Université du Québec
Institut National de la Recherche Scientifique
Centre Énergie, Matériaux et Télécommunications

Synthesis and Characterization of Semiconductor Nanocrystals for Solar Technologies

Par

Yufeng Zhou

Thèse présentée pour l'obtention du grade de
Philosophiae doctor (Ph.D.)
en sciences de l'énergie et des matériaux

Jury d'évaluation

Président du jury et examinateur interne	Emanuele Orgiu INRS-EMT, Université du Québec
Examinateur externe	Tomislav Friščić McGill University
Examinateur externe	Rafik Naccache Concordia University
Directeur de recherche	Federico Rosei INRS-EMT, Université du Québec
Codirecteur de recherche	Dongling Ma INRS-EMT, Université du Québec

Abstract

Semiconductor nanocrystals (NCs) have been widely investigated in recent decades due to their unique optical, electrical properties and various applications in solar technologies, such as solar cells, luminescent solar concentrators (LSCs) and solar-driven water splitting. Among these semiconductor NCs, colloidal semiconducting quantum dots (QDs), are regarded as promising candidates for LSCs applications, with size/composition- tunable optical properties (including high photoluminescence quantum yield (PLQY), broad absorption, high photo/chemical stability, *etc*. However, it is still challenging to synthesize colloidal QDs with large Stokes shift, high PLQY and broad absorption spectrum, which are the criteria for large-area high efficient LSCs fabrications. In addition, ultra-thin semiconducting nanoplatelets (NPLs) with high carrier mobility, narrow emission spectrum and high PLQY, have been investigated and used for light emitting diodes, solar-driven hydrogen generation applications. To broaden the absorption range of ultra-thin NPLs for solar technologies, it is demanding to synthesize near infrared (NIR) NPLs with high QY and colloidal photo/chemical stability.

I firstly synthesized mixed-halide perovskite $CsPb(Br_xI_{1-x})_3$ QDs with different ratios of Br/I precursors via *hot-injection* method, which show tunable absorption and emission spectra. The mixed-halide perovskite $CsPb(Br_{0.2}I_{0.8})_3$ QDs exhibit high PLQY of ~60%, small overlap of absorption and emission, broad absorption ranging from 300-650 nm, which is a promising material as PL emitters in LSCs applications. The optical performance of LSCs based on perovskite $CsPb(Br_{0.2}I_{0.8})_3$ QDs was investigated and an external optical efficiency of 2% with a geometrical (G) gain factor of 45 has been achieved. In addition, the LSCs exhibit long-term stability without any noticeable variations in PL emissions and lifetimes under ultraviolet (UV, 4W) illumination for over four hours.

To extend the light absorption spectrum of QDs, near infrared (NIR) PbS/CdS core/shell QDs have been synthesized with various core sizes and shell thicknesses. Specifically, the bare PbS QDs was prepared via *hot-injection* method with different capping ligands. An engineered Stokes shift in NIR core/shell PbS/CdS QDs was achieved via a cation exchange approach by varying the core size and shell thickness through the refined reaction parameters, such as reaction time, temperature, precursor molar ratio, *etc*. The as-synthesized core/shell QDs with high PLQY and excellent chemical/photo- stability exhibit a large Stokes shift with respect to the bare PbS QDs due to the strong core-to-shell electrons leakage. The large-area planar LSC based on core/shell QDs exhibits the higher value (6.1% with a G factor of 10) for optical efficiency than that of the bare NIR QD-based LSCs and other reported NIR QD-based LSCs. The suppression of reabsorption loss and the broad absorption of PbS/CdS QDs offer a promising pathway to integrate LSCs and photovoltaic devices with well spectral matching.

Compared to conventional inorganic QDs which act as PL emitters in LSCs, carbon dots (C-dots) have superior advantages of non-toxicity, environmental friendliness, low-cost and simple preparation using abundant carbon based feedstock. We synthesized colloidal C-dots via solvothermal method using different solvents, surfactants and carbon sources. We further demonstrated large-area LSCs (up to 100 cm^2) using colloidal C-dots. Two types of LSCs were fabricated by either incorporating oil-soluble oleylamine-treated C-dots into photo-polymerized poly(laurylmethacrylate) (PLMA) or spin-coating the water-soluble C-dots/polyvinylpyrrolidone (PVP) mixture on the glass substrate. The LSCs based on C-dots/PLMA exhibit an internal quantum efficiency of 4% (G factor of 38), and an optical efficiency of 1.1% (100 cm^2, G factor of 12.5) of tandem thin-film LSCs based on C-dots/PVP was achieved under one sun illumination. The optical performance is comparable to those of LSCs based on inorganic QDs with similar G

factor. The LSCs based on C-dots are highly air-stable without any noticeable variations in PL emissions under UV illumination (1.3 W/cm^2) for over 12 h. These large-area LSCs based on C-dots exhibit a highly transparency (over 90% for wavelengths longer than 500 nm) with low reabsorption losses, excellent optical performance including high optical efficiency and very good photostability.

Aside from the fabrication of QDs based LSCs, we developed a cation exchange route to synthesize ultrasmall lead chalcogenides NIR $PbSe_{1-x}S_x$ NPLs. Basically, the as-prepared $PbSe_{1-x}S_x$ NPLs with small lateral dimensions, controlled thickness of ~2 nm, and different compositions were obtained via a cation exchange process on template CdSe or alloyed $CdSe_{1-x}S_x$ NPLs using various Pb precursors. The NIR NPLs exhibit continuously tunable PL emission ranging from 1180 to 1380 nm thanks to the variation of the S/Se ratio, which cannot be achieved in binary NPLs, and a high PLQY up to ~60%. Theoretical simulations of the bandgap as a function of thickness, geometry, and lateral size show that ultrasmall NPLs exhibit strong 3D quantum confinement, compared to 1D confinement in larger sized NPLs with similar thickness. As a proof-of-concept, we used the NPLs as photosensitizers for solar-driven hydrogen generation. After surface treatment with Cd, a saturated photocurrent density of ~5 mA/cm^2 at 1.0 V vs RHE was obtained using NIR NPLs based photoanode under one sun illumination.

Acknowledgements

I would first like to thank my supervisor Prof. Federico Rosei for the insightful suggestions and supports throughout my PhD study. I want to thank my co-supervisor Prof. Dongling Ma for her useful advice and encouragement. And I acknowledge the UNESCO Chair in Materials and Technologies for Energy Conversion, Saving and Storage (MATECSS) for a PhD Excellence Scholarship.

I would particularly like to single out my group leader Prof. Haiguang Zhao for the continuous support of my research, for his patience, motivation and immense knowledge. In addition, I would like to thank our collaborator Prof. Alberto Vomiero for the meaningful comments and guidance, Prof. Alexander O. Govorov, Prof. François Vidal, Prof. Margherita Zavelani-Rossi and Dr. Mert Celikin for their helps and supports.

I would like to thank my colleagues, Daniele Benetti and Xin Tong for excellent and inspiring discussions, and constant supports. Thanks to my colleagues Dr. Gurpreet Singh Selopal, Dr. Fabiola Navarro-Pardo, Dr. Adhikari Rajesh, Lei Jin, Kaustubh Basu, Rusoma Akilimali, Wei Huang, Jiabin Liu, Daling Cui, Joyprokash Chakrabartty, Kanghong Wang and other colleagues for their helps and suggestions.

I would like to share my appreciates to my friends at INRS-EMT center, Yanqing Fu, Qiliang Wei, Fan Yan, Yanlong Liu, Miao Wang and Nathanael Komba for all the fun we had in the past four years. I also thank to our nice technicians and staffs at INRS-EMT, particularly Louise Hudon, Christophe Chabanier, Georges Lamoureux and Helene Sabourin. Besides, I am grateful to Jean-Philippe Masse for TEM measurement.

Last but not the least, I would like to thank my parents and Bingyu Sun for supporting me spiritually throughout my life.

Contents

List of Figures

List of Tables

Chapter 1 Introduction

1.1 Clean and renewable energy

Generating power directly or indirectly from sustainable resources, such as solar radiation, provides an attractive approach towards addressing the increasing demands for clean and renewable energy, with minimal environmental impacts caused by the excessive carbon emissions.[1,2] In order to address these issues, many possible solutions have been explored and put in place today. For instance, efficient energy products, such as light emitting diodes (LED), are applied to replace traditional bulbs, which will use less watts of electricity and last longer.[3] If most of people across the globe adopt these products, the demand for electricity would be lowered, alleviating the energy crisis. However, for the moment, they have not been widely adopted and practical. In Figure 1.1, during the last several decades, the global energy consumption from non-renewable resource rises very fast and in 2017 accounts for over 80% of whole energy consumption.[4]

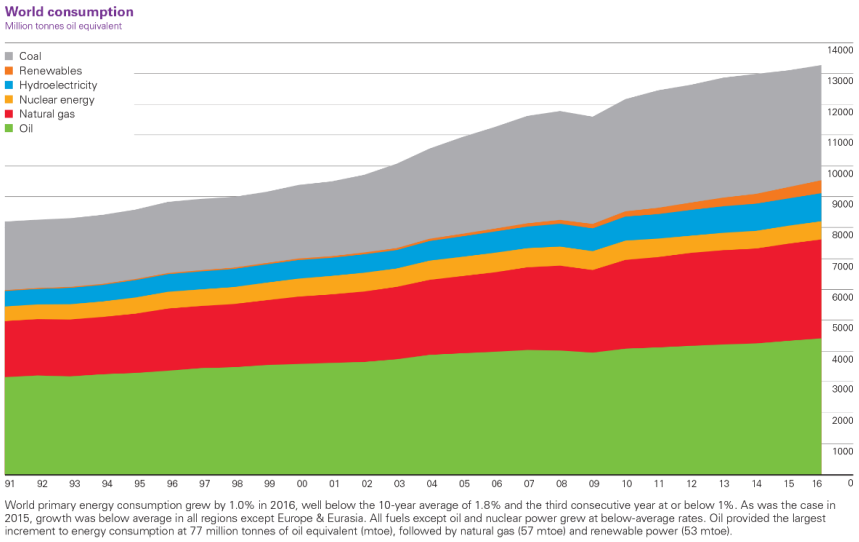

Figure 1.1 The world's energy consumption from different resources.[4]

An alternative approach is to utilize clean and renewable energies for global energy consumption. To date, renewable energy includes solar, wind, biomass, heat and hydropower etc.[5-8] Hydropower is clean power collected from the energy of falling water or fast running water, which can be used for electricity generation or irrigation. In some regions, such as Quebec Province in Canada, more than 95% of electricity used (which is equal to 40% of total energy consumption) since 2011 is generated from hydropower.[9] Additionally, the electricity derived from traditional biomass holds half of energy generated from renewable sources.[10] Among these clean and renewable energy resources, solar energy provides enormous potentials to fulfill the global energy consumptions.[11] Every hour, radiation impinging from the sun would be sufficient to power the whole planet for one year. However, the electricity generated from solar energy is only ~ 1.3% of total energy consumption so far.[4] Efficient conversion of solar radiation into electrical/chemical energy and their storage are quite demanding and challenging in recent years.

1.2 Utilization and storage of solar energy

Solar energy is regarded as an important clean and renewable resource, which can be directly or indirectly converted into electricity or chemical energy based on solar technologies without significantly environmental pollution. Solar cells (SCs) are photovoltaic (PV) devices that harvest the solar radiation and convert it into electricity.[12] In the past decades, silicon (Si) solar cells have been widely explored and commercialized due to their relatively high power conversion efficiency (PCE) and long-term stability (after 30-year use, only 20% drops in PCE was observed). The PCE of crystalline Si solar cells can be improved to ~20-40% with varied architectures. Additionally, the PCE of thin-film (CdTe, CuInGaSe, a-Si) solar cells has been enhanced to > 20%.[13] However, the fabrication of Si and thin-film solar cell is complicated and requires skilled people and high-cost equipments.[14] Current research directives in solar energy conversion are investigating new

methods, and, in particular, new materials and processes that will render integrated and more efficient power harvesters.[15,16]

Third-generation solar cells (also called excitonic solar cell) are a class of emerging PV devices. They include dye-sensitized solar cells (DSSCs), organic solar cells, perovskite solar cells, polymer solar cell and quantum dots (QDs) sensitized solar cells (QDSCs).[17-20] A typical structure of DSSC is illustrated in Figure 1.2.[21] Basically, incident photons are absorbed by organic dyes upon solar illumination, and exciton pairs (electron-hole pairs) are generated and separated. The electrons are injected into TiO_2 nanocrystals further flows out through an external circuit, while the holes are transferred to the counter electrode via a redox reaction.

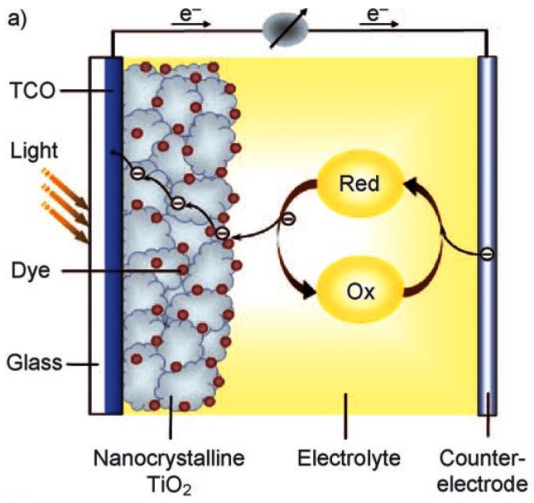

Figure 1.2 Scheme of a DSSC with a marked electron flow.[21]

In general, the fabrication of third-generation solar cells is much simpler and more cost-effective compare to Si solar cells.[17-20] However, commercial DSSCs products can work only for a few years and the PCE is still lower than 10%, which gives the ample room for the development and the use of luminescent solar concentrators (LSCs).[20]

LSC is another technology which can generate electricity with low cost and high efficiency. Typically, an LSC consists of a planar plastic waveguide embedded with fluorophores, such as quantum dots and organic dyes (Figure 1.3).[22,23] Upon the illumination on the top surface of LSCs, the photon is absorbed by fluorophores and reemitted at a longer wavelength, then guided through the edges of LSCs where a PV device is coupled with it. This approach will largely reduce the active area and the cost of PV devices and boost the PCE of solar cells. Besides, LSCs can be also applied for building-integrated PVs and lighting objects.[24,25]

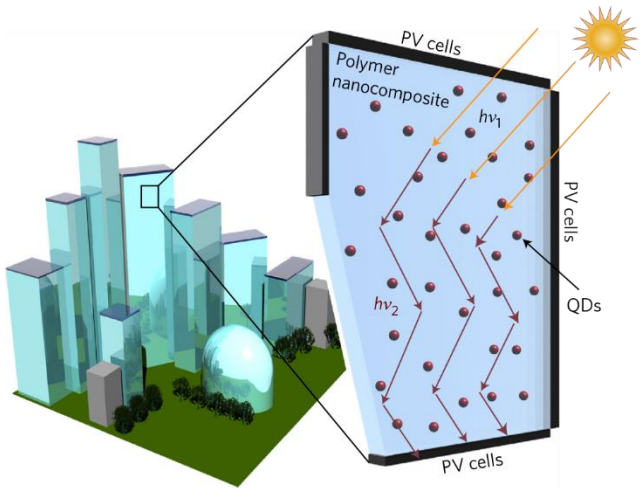

Figure 1.3 Schematic representation of an LSC window composed of a polymer matrix incorporating reabsorption-free QDs.[22]

In recent years, organic dyes with high PL quantum yield (PLQY) have been investigated as PL emitters for LSCs fabrications.[26-28] However, the spectral overlap between absorption and emission of organic dyes such as Rhodamine with QY less than 100% is intrinsically large, which causes reabsorption issues and hampers the fabrication of large-area high optical efficiency (η_{opt}, defined as the ratio of output power (P_{out}) coming from the edges of LSC and the input power (P_{in}) through the top surface of LSC) LSCs.[29] Moreover, organic dyes suffer from the photodegradation due to the direct interaction of dyes and sunlight, or the attack on the dyes by an active species formed

by residue molecule in polymer matrix, resulting in poor photo/chemical stability.[30,31] Semiconducting nanocrystals, for instance, QDs are promising PL emitters for LSCs due to their excellent photo/chemical stability and engineered large Stokes shift (defined as the difference in wavelength between positions of the band maxima of absorption and emission spectra). Compared to organic dyes, QDs have huge potentials for large-area highly efficient and stable LSCs fabrications.[32,33]

Solar energy is not a constant stream of energy, which makes the storage of solar energy significant. For example, the electricity can be generated from sun radiation and stored in battery.[34] Thermal energy storage allows excess thermal energy to be collected from sunlight for later use.[35] Similarly, the incident photon absorbed by semiconductors can be applied for solar-driven water splitting via photoelectrochemical (PEC) system.[36] The clean chemical energy sources hydrogen can be stored and transported for appropriate usages. Typically, in a PEC system, upon sun illumination, semiconductor nanocrystals act as light absorbers and sensitizers. The photogenerated carriers are separated and transferred into photoanode and photocathode for oxygen and hydrogen generation reactions, respectively.[36] The metal oxides such as ZnO and TiO_2 are widely investigated for solar-driven hydrogen generation. However, the optimal materials with appropriate bandgap (usually forbidden d-d transitions) for solar-driven hydrogen generation have very small optical absorption coefficient. On the other hand, the mobilities of carriers in metal oxides are quite low, resulting in short carrier diffusion lengths. Until now, the solar-to-hydrogen (STH) conversion efficiency in PEC cell is still low, which needs to be further boosted. To enhance the long-term photostability (PEC performance vs time) of photoelectrodes and lower their cost are also very challenging for practical realizations.

1.3 Semiconductor nanocrystals for solar technologies

Semiconductor nanocrystals are small fluorescent particles with typical dimensions in the range of 1-100 nanometer (nm) with respect to bulk semiconductor, exhibiting size-dependent optical and electronic properties. In Figure 1.4, the electronic density of states in bulk semiconductor is continuous, and the corresponding bandgap energy of semiconductor is composition-dependent.[37] The exciton is formed in semiconductor nanocrystals when the photon with energy larger than bandgap energy is absorbed. Basically, the excited electron will be recombined with the hole in the valence band, emitting a photon via radiative recombination.[38] When one or more dimensional sizes of semiconductor nanocrystals are decreased to the same magnitude of exciton Bohr radius, which is defined as the distance in an electron-hole pair, the charge carriers will be spatially confined.[39] The unique properties of semiconductor nanocrystals provide enormous potential for the application in solar technologies.

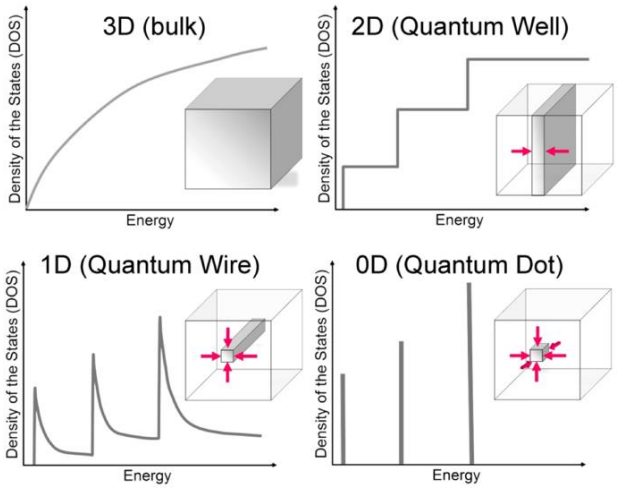

Figure 1.4 Schematic diagram illustrating the representation of the electronic density of states depending on dimensions.[37]

Semiconductor QDs are 3-dimensionally (3D) quantum confined (Figure 1.5a).[40] Generally, when the size of QDs increases, the corresponding bandgap decreases accompanied with a red-shift PL emission. Figure 1.5b dispalys tunable PL spectra of core/shell CdSe/ZnS QDs with various core

sizes.[41] Due to quantum confinement effect of QDs, their electronic band structures can be designed and engineered by controlling the core size, shell thickness, and the choose of materials and chemical composition. Based on the bandgap and the relative position of electronic energy levels of core or shell materials, the band alignment of core/shell QDs can be generally classified into Type I, Type II and reverse Type I, shown in Figure 1.5c.[42]

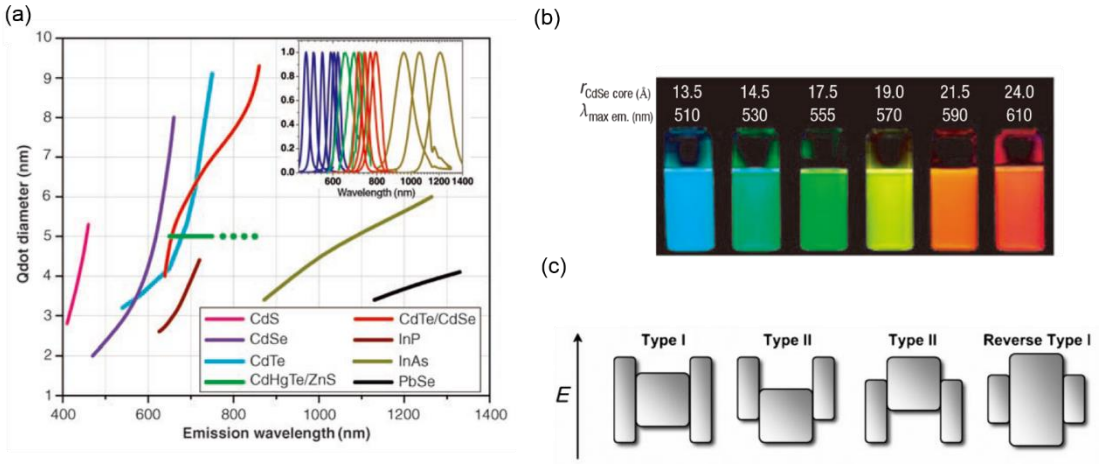

Figure 1.5 (a) Emission maxima and sizes of QDs of different composition. Inset: representative emission spectra for some materials.[40] (b) Size tunable PL spectra of CdSe/ZnS QDs.[41] (c) Schematic representation of the energy-level alignment in different core/shell systems realized with semiconductor NCs to date. The upper and lower edges of the rectangles correspond to the positions of the conduction- and valence-band edge of the core (center) and shell materials, respectively.[42]

Compared to traditional organic dyes, QDs shows superior optical properties, such as broad absorption spectrum covering ultraviolet (UV), Visible (Vis) and near infrared (NIR) range, tunable absorption/emission spectra, large absorption coefficient and high long-term photostability.[43] With high PLQY of QDs in polymer based device, it can be used to fabricate high efficiency LED. The QDs with high PLQY and large Stokes shift is favorable in the fabrication of QDs based LSCs. Additionally, QDs with high carrier mobility and appropriate band structures can be applied to the related solar technologies, including QDSCs, and QDs based solar-driven water splitting.[44-47]

1.4 Quantum dots based luminescent solar concentrators

As introduced in section 1.2, QDs can be used as highly efficient PL emitters in LSCs. Recently, highly efficient LSCs based on various types of colloidal QDs, e.g. CdSe/CdS QDs, CuInSeS/ZnS QDs and Si QDs have been widely investigated.[22,46,48-50] A typical structure of QDs based LSC is showed in Figure 1.6.[51] Light can be lost in different ways (processes (1) to (5) in the scheme). (1) Only a fraction of incident light can be absorbed due to the limited overlap between the QD's absorption spectrum and solar spectrum; (2) part of the light is reflected at the top surface of the LSC; (3) light is lost during nonradiative recombination, because the typical PLQY is below 100%; (4) if the emission angle of a re-emitted photon is smaller than that of the critical angle, this photon will be escaped from the so-called escape cone and cannot undergo total internal reflection inside the waveguide; (5) part of the light is lost due to re-absorption. Other minor light losses could be due to the absorption of emitted light by the polymer matrix.

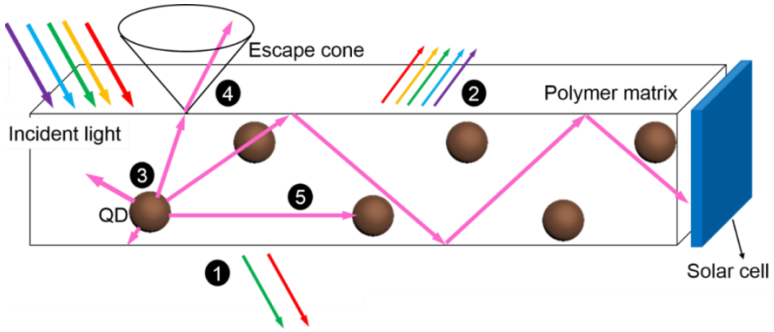

Figure 1.6 Schematic representation of a QD-based LSC. (a) LSC is obtained by embedding the QDs in a transparent polymer matrix. The numbers indicate the typical processes of energy loss in an LSC. (1) Unabsorbed light; (2) Light reflects from the top surface; (3) The light was absorbed by the QDs, but there is partial loss due to the non-unity of fluorescence QY; (4) Re-emitted incident light escapes from the surface due to the escape cone (the angle smaller than the critical angle). (5) Light is reabsorbed by another QD.[51]

The theoretically optical efficiency of an LSC can be specifically calculated from Equation 1.1:[23]

$$\eta_{\mathrm{opt}} = (1 - \mathrm{R}) \cdot P_{\mathrm{TIR}} \cdot \eta_{\mathrm{abs}} \cdot \eta_{\mathrm{PLQY}} \cdot \eta_{\mathrm{Stokes}} \cdot \eta_{\mathrm{host}} \cdot \eta_{\mathrm{self}} \quad (1.1)$$

where R is the reflection of solar light from the waveguide surface, P_{TIR} is the total internal reflection efficiency, η_{abs} is the fraction of solar light that is absorbed by the emitter, η_{PLQY} is the PLQY of QDs, η_{Stokes} is the energy loss due to heat generation during the absorption and emission event, η_{host} is the transport efficiency of the wave-guided photons through the waveguide, η_{TIR} is the reflection efficiency of the waveguide, and η_{self} is related to re-absorption of the emitted photons by another fluorophore in the waveguide.[33]

How to avoid the energy loss because of the reabsorption (5) is the key to realizing high efficiency LSCs. Ideally, if a QY of QDs is 100%, the energy loss mainly depends on the critical angle θ_C ,as the re-emitted photons still can escape from the LSC (process 4). While there would be no energy loss through process 3. In the real case, the QY of colloidal QDs is typically lower than 100% and there is a spectral overlap between the absorption and emission spectra of QDs. Energy losses from re-absorption of the QDs occur repetitively, because photons traveling within the waveguide may be absorbed and re-emitted by other QDs with similar energy band edges multiple times before reaching an edge. In practical LSC implementations, optical path lengths may reach a meter or more, and even very small overlap between absorption and emission spectra would result in strong energy losses. Thus, the synthesis of QDs with high QY, large Stokes shift, broad absorption spectrum matching with solar radiation, and high stability becomes one of the most critical issues in fabricating large-area high efficiency LSCs. And these issues can be further addressed by design and synthesis of QDs with controllable size and chemical composition to precisely tune optical transitions for application of LSCs.[22,46,48,49]

1.5 Nanoplatelets based photoanode for solar-driven hydrogen generation

Besides using semiconducting nanocrystals for LSCs, they can also be employed as light absorbers and sensitizers in PEC devices for solar-driven H_2 production or water splitting application. In a PEC system, oxygen and hydrogen from water can be generated in a light-induced water splitting reaction, illustrated in Figure 1.7a.[52] In this set-up, light impinges on an electrode (for example the photoanode, made from a photocatalytic material such as titanium oxide, TiO_2), generating negatively charged electrons (e^-) and positively charged 'holes' (h^+). Electrons excited in the conduction band from photoanode are drained away through external circuit and flow to counter electrode for hydrogen generation. The holes remaining at the photoanode react with water to form oxygen. If the hole scavenger is used in this system, the generated holes are consumed without oxygen generation. In Figure 1.7b, the band alignments of conventional semiconductor materials (such as TiO_2, WO_2 *etc*) used for photoanodes in PEC system are reported.[53] To date, the STH conversion efficiency is still low due to the limit harvest of solar radiation, and lower carrier separation and transport efficiencies in PEC system. In this case, two-dimensional semiconductor NPLs shows encouraging features for hydrogen generation, with the advantages of tunable absorption spectrum matching with solar spectrum, large surface area that can offer more active catalytic sites, which can also mimic the photosynthetic process within a leaf by splitting water to produce hydrogen or oxygen fuels.[54-58] For example, Bi_2S_3 sensitized WO_3 NPLs arrays shows enhanced PEC performance with photocurrent density of ~8.0 mA/cm^{-2} at −0.1 V vs Ag/AgCl reference electrode,[59] which is active under visible light.[59]

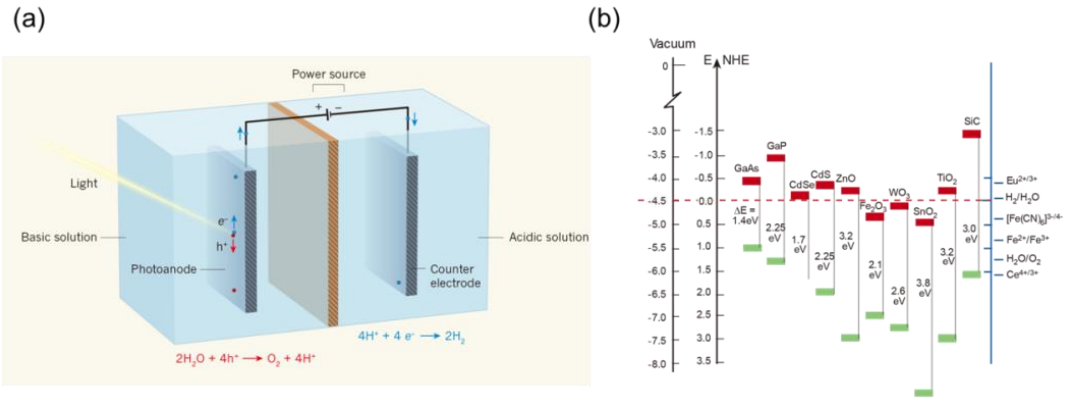

Figure 1.7 (a) Schemetic demonstration of a water-splitting cell.[52] (b) Band positions of several semiconductors in contact with aqueous electrolyte at pH 1. On the right side the standard potentials of several redox couples are presented against the standard hydrogen electrode potential. The energy scale is indicated in electron volts using either the normal hydrogen electrode (NHE) or the vacuum level as a reference.[53]

Moreover, ultrathin NPLs (for example In_2S_3 porous sheets[58] and CdS nanosheets[60]) have been widely studied and applied for hydrogen generation (or water splitting) in PEC system, exhibiting excellent photocatalytic performance, such as high carrier mobility and transfer rate, relatively high photocurrent density at certain applied potential for hydrogen generation reaction. Therefore, the synthesis of ultrathin NPLs with broad absorption spectrum could be an efficient approach to enhance solar-to-hydrogen efficiency and stability. In this thesis, I will focus on the preparation of photoanodes based on nanoplatelets (NPLs) for hydrogen generation.

1.6 Thesis objectives and contributions of this work

As described in the introduction of LSCs (Chapter 1.4), it is quite challenging to fabricate highly efficient, stable and environment friendly large-area QDs based LSCs. Specifically, the design and synthesis of efficient emitter is of significant importance for LSCs application. Efficient emitter requires the following features, (1) relatively high QY; (2) broad absorption spectrum matching with solar radiation; (3) small or zero overlap between absorption and emission spectra; (4) heavy

metal-free materials; (5) high and long-term stability in polymer matrix under illumination and ambient condition; (6) simple and green synthesis method.

To address the above issues, I plan to synthesize efficient PL emitters (semiconductor QDs) for LSCs, and fabricate large-area LSCs based on as-prepared QDs.

1. Synthesize high-QY emitter (perovskite QDs) with tailored Stokes shift, and characterize perovskite QDs based LSCs.
2. Synthesize NIR PbS/CdS QDs with large Stokes shift for LSCs fabrication, and characterize PbS/CdS QDs based LSCs.
3. Use of "green" carbon quantum dots (C-dots) for LSCs fabrication via simple method, and characterize C-dots QDs based LSCs.

The synthesis of ultrathin NPLs with wide absorption spectrum is also demanding for the hydrogen generation application, enhancing the solar-to-hydrogen conversion efficiency and long-term stability.

I plan to synthesis ultrathin NPLs with broad absorption spectrum for solar-driven hydrogen generation. The objectives of my projects are in the following:

1. Synthesis of ultrathin NIR NPLs with broad absorption and high photostability.

2. Apply the as-obtained NIR NPLs as light absorbers and sensitizers for photoanode fabrication in solar-driven hydrogen generation application.

1.7 Thesis organization

This thesis is divided into six parts and organized as follows:

Chapter 1 introduces the topic of this thesis and outline the motivation for this work.

Chapter 2 presents the synthesis and characterization of high-QY mixed-halide perovskite $CsPb(Br_xI_{1-x})_3$ QDs with tunable Stokes shift via varying concentration ratio of Br/I precursors, and investigate the optical performance (optical efficiency, quantum efficiency and stability) of LSCs based on mixed-halide perovskite $CsPb(Br_xI_{1-x})_3$ QDs.[61] The publication related to this chapter is:

61. H. Zhao#, Y. Zhou#, Benetti, D.; Ma, D.; Rosei, F. *Nano Energy* **2017**, *37*, 214. (#: equal contribution)

Chapter 3 presents the synthesis and characterization of core/shell PbS/CdS QDs with engineered Stokes shift by tailoring core size and shell thickness, and discuss the optical performance (optical efficiency, quantum efficiency and stability) of LSCs based on core/shell PbS/CdS QDs.[62] The publication related to this chapter is:

62. Zhou, Y.; Benetti, D.; Fan, Z.; Zhao, H.; Ma, D.; Govorov, A. O.; Vomiero, A.; Rosei, F. *Adv. Energy Mater.* **2016**, *6*, 1501913.

Chapter 4 presents the synthesis of non-toxicity, low-cost C-dots fabrication via simple method using relatively earth-abundant carbon based feedstock. In addition, I investigate optical properties of surface modified C-dots and the optical performance of large-area C-dots based LSCs.[63] The publication related to this chapter is:

63. Zhou, Y.; Benetti, D.; Tong, X.; Jin, L.; Wang, Z. M.; Ma, D.; Zhao, H.; Rosei, F. *Nano Energy* **2018**, *44*, 378.

Chapter 5 presents the synthesis of NIR ultrathin $PbSe_{1-x}S_x$ NPLs via cation exchange using $CdSe_{1-x}S_x$ NPLs as templates. And I investigate the formation mechanism and optical properties

of $PbSe_{1-x}S_x$ NPLs. Finally, we study the performance of $PbSe_{1-x}S_x$ NPLs based photoanode in application solar-driven hydrogen generation.[64] The publication related to this chapter is:

64. Zhou, Y.; Celikin, M.; Camellini, A.; Sirigu, G.; Tong, X.; Jin, L.; Basu, K.; Tong, X.; Barba, D.; Ma, D.; Sun, S.; Vidal, F.; Zavelani-Rossi, M.; Wang, Z. M.; Zhao, H.; Vomiero, A.; Rosei, F. *Adv. Energy Mater.* **2017**, *7*, 1602728.

Chapter 6 briefly summarizes important contributions of this work and states future challenges in this field.

Following the main body of thesis is an appendix providing a summary of this thesis in French as per INRS requirements.

Chapter 2 Synthesis and characterization of perovskite quantum dots based luminescent solar concentrator

In this chapter, I discuss the synthesis and optical properties of inorganic mixed-halide perovskite $CsPb(Br_xI_{1-x})_3$ QDs with different feeding ratios of Br/I. The resulting perovskite QDs with high PLQY of over 60% and small overlap of absorption and emission spectra has been applied as emitter for LSC application (Figure 2.1). Additionally, the optical performance and photostability of LSCs under long-term UV illumination have been investigated.

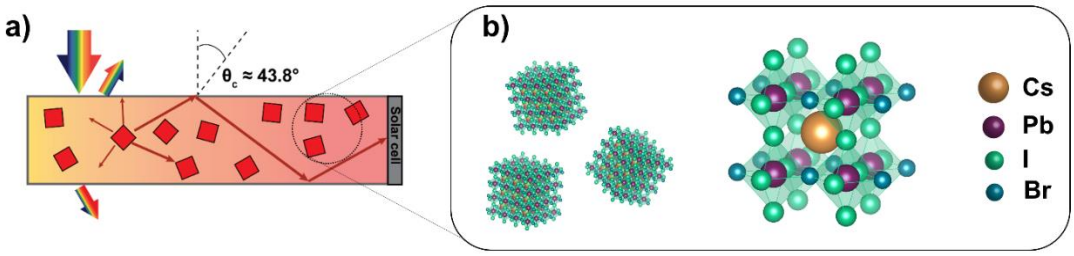

Figure 2.1 (a) Scheme of a typical LSC configuration. (b) Cubic structure of mixed-halide perovskite QDs of $CsPb(Br_xI_{1-x})_3$.

2.1 Synthesis and characterization of perovskite quantum dots

Colloidal hybrid organic-inorganic and inorganic perovskite QDs have been synthesized and used as building blocks in a variety of devices.[65-72] Among various kinds of perovskite QDs, inorganic $CsPbX_3$ (X = Cl, Br, I) QDs have been widely studied for optoelectronic applications in view of their size/compositional dependent absorption and emission spectra, wide absorption spectrum, high brightness with a PLQY up to 90% or unity, narrow emission linewidth, easy solution phase synthesis and good photostability.[65,66,68,69] Inorganic perovskite QDs may represent a new promising candidate for efficient LSCs.

2.1.1 Synthesis of perovskite quantum dots

A hot injection synthetic method was used to synthesize colloidal perovskite QDs according to procedures found in the literature.[70,71] Firstly, the precursor Cs-oleate was synthesized. Specifically, a solution of oleic acid (OA, 0.6 mL) and Cs_2CO_3 (0.2 g) in 7.5 mL of 1-octadecene (ODE) was stirred and heated to 200 °C until the Cs_2CO_3 was completely dissolved. Then the mixture was kept at 130 °C for one hour under vacuum. The temperature of the Cs-oleate mixture was kept at least at 80 °C to avoid precipitation.

Mixed-halide perovskites of $CsPb(Br_xI_{1-x})_3$ were synthesized by using a hot injection approach. Typically, in a 100 mL round-bottom flask, OA (2 mL), oleylamine (OLA, 2 mL), ODE (20 mL) and 290 mg of $PbBr_2$ (or 368 mg PbI_2) were degassed at 100 °C for 30 min. The reaction flask was re-stored with N_2 and heated to 130 °C for 30 min under vacuum. The temperature was further increased to 160 °C, followed by the rapid injection of 1.8 mL of Cs-oleate solution. The reaction was kept at 160 °C for 5 seconds and then the solution was rapidly cooled by the water bath. For the synthesis of the mixed-halide perovskite QDs, a mixture of $PbBr_2$/ PbI_2 with different molar ratios (1:9, 2:8, 3:7, 4:6 and 5:5) was used as halide precursors. All other reaction conditions, such as injection temperature and reaction time are the same with the synthesis of $CsPbBr_3$ or $CsPbI_3$ QDs. Butanol was added, then the suspension was centrifuged and the supernatant was removed. The QDs were then re-dispersed in toluene for further characterization. The as-prepared QDs are very sensitive to moisture and need to be kept in a desiccator or a refrigerator at -10 °C.

2.1.2 Structure and optical properties

Transmission electron microscopy (TEM) was used to characterize sizes and morphologies of as-synthesized QDs (Figure 2.2). As shown in Figures 2.2a,b,c, mixed-halide $CsPb(Br_xI_{1-x})_3$ QDs show a typical cubic/cuboidal shape with size between 11-15 nm. For example, $CsPb(Br_{0.4}I_{0.6})_3$ QDs exhibit a size of 12.9± 1.7 nm (standard deviation, σ <15%) (Figure 2.3). In a big contrast,

$CsPbI_3$ and $CsPbBr_3$ QDs show a cubic shape with more uniform size of 7.9 ± 0.3 nm and 8.5 ± 0.3 nm (σ < 7%) respectively (Figures 2.2d,e and 2.3a,b). The crystal lattice is clearly visible by high resolution TEM (HRTEM) imaging (Figures 2.2b-e). The inset in Figure 2.1b displays a micrograph of an individual $CsPb(Br_{0.4}I_{0.6})_3$ QD with a lattice spacing of ~0.597 nm which is well indexed to the (200) plane of the cubic phase, consistently with previous reports.[70,71]

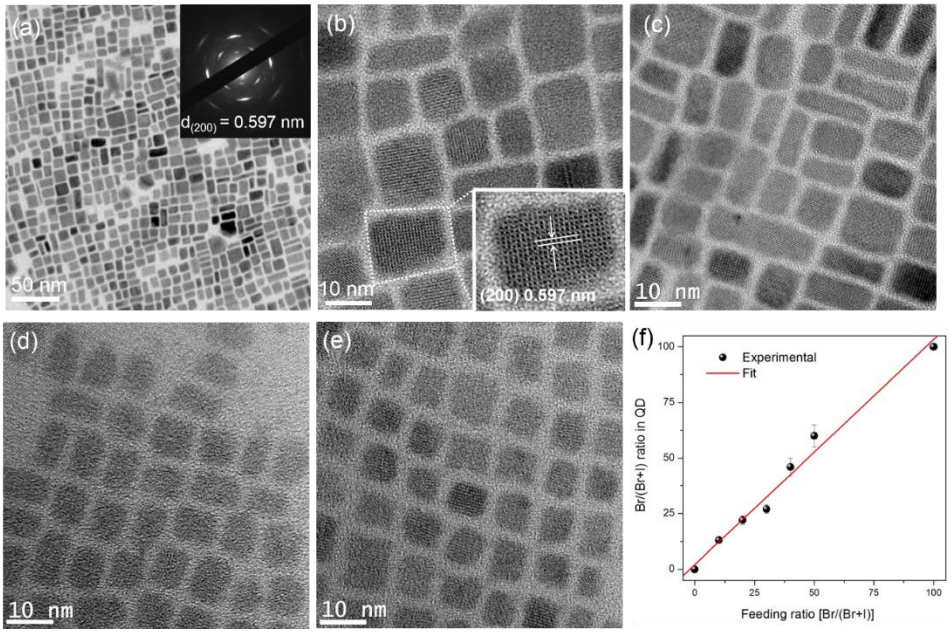

Figure 2.2 Representative TEM images of $CsPb(Br_xI_{1-x})_3$ QDs (a-e). (a) A large-area TEM image and corresponding SAED pattern (inset) of $CsPb(Br_{0.4}I_{0.6})_3$ QDs. HRTEM images of $CsPb(Br_{0.4}I_{0.6})_3$ QDs (b), $CsPb(Br_{0.5}I_{0.5})_3$ QDs (c), $CsPbI_3$ QDs (d), and $CsPbBr_3$ QDs (e). Inset of (b): a HRTEM image of an individual perovskite QD. (f) Concentration of Br as a function of feeding ratio of Br/(Br+I) precursors.

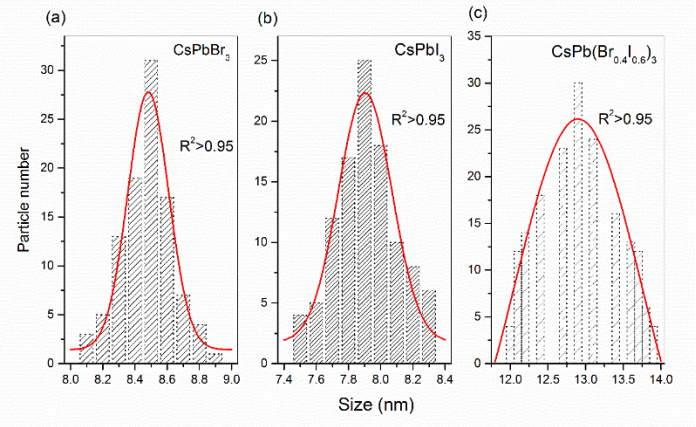

Figure 2.3 Size distribution of perovskite QDs of (a) $CsPbBr_3$ QDs (8.5 ± 0.3 nm), (b) $CsPbI_3$ QDs (7.9 ± 0.3 nm) and (c) $CsPb(Br_{0.4}I_{0.6})_3$ QDs (12.9± 1.7 nm).

The typical cubic structure of mixed-halide perovskite is shown in Figure 2.2b. The lattice distances further measured by selected area electron diffraction (SAED) patterns of $CsPb(Br_{0.4}I_{0.6})_3$ (inset image of Figure 2.2a) and other perovskite QDs are well indexed to the (200) planes of cubic phase. The measured lattice spacing of (200) decreases with the increase of Br concentration, due to the larger lattice spacing in $CsPbI_3$ compared to $CsPbBr_3$ (Table 2.1). The corresponding energy-dispersive X-ray spectroscopy (EDX) spectrum of an individual $CsPb(Br_xI_{1-x})_3$ QD with feeding ratio of 40% (Br/[Br+I]) confirms the presence of elemental Cs, Pb, Br/I and 1:1:3 atomic ratio for $CsPbX_3$ (Figure 2.4). Based on the EDX analysis, with increase of feeding ratio of Br/(Br+I), the real concentration of Br in Br_xI_{1-x} increases linearly, indicating the successful control of the chemical composition of mixed-halide perovskite QDs (Figure 2.2f).[65-67]

Table 2.1 D-spacings of perovskite QDs with variations of Br concentration.

Br concentration (%)	(200)
0	0.619
10	0.617
20	0.615
30	0.614
40	0.597
50	0.594
100	0.584

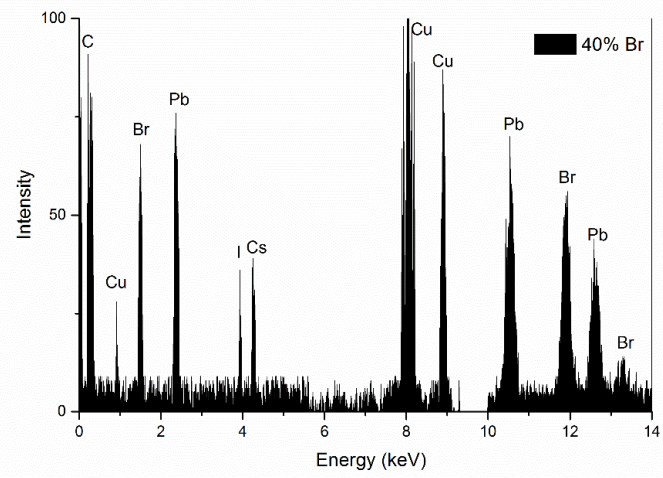

Figure 2.4 EDX of an individual $CsPb(Br_{0.4}I_{0.6})_3$ QD.

The absorption and PL spectra of colloidal $CsPb(Br_xI_{1-x})_3$ QDs with various chemical compositions are reported in Figure 2.5a. The absorption spectrum acquired from perovskite QDs can be tuned over the entire window of visible wavelength (300-700 nm) by adjusting their chemical composition (ratio of halide precursors), which allows an efficient capture of solar radiation in this

spectral range. The first-excitonic absorption peak shifts to red gradually with the decrease of Br concentration, consistently with the red-shift of the PL peak. Compared to $CsPbX_3$ (X= Br, I) QDs with PL full width at half maximum (FWHM) of ~17-20 nm, the broadening in the FWHM in mixed-halide perovskite QDs (~35 nm) is due to their lower size uniformity (Figure 2.3). The as-synthesized $CsPbI_3$ QDs show a typical QY of ~20 ± 2% after purification. This is much lower compared to values of 40-70% reported in the literature,[65,66,68,69] which is possibly due to their sensitivity to moisture, since the purification procedure was carried out under normal ambient conditions with average humidity of ~40%.[69] In contrast, mixed-halide QDs exhibit higher QYs compared to $CsPbI_3$ QDs. When x is over 10%, the QYs of QDs exceed 60%. The $CsPbBr_3$ QDs show a highest QY of 90%. In addition, mixed-halide QDs or $CsPbBr_3$ QDs exhibit a very good stability compared to $CsPbI_3$ QDs. There is no significant QY variation after keeping the $CsPb(Br_xI_{1-x})_3$ samples in -10 °C or in a desiccator (20 °C) for 3 months. Compared to $CsPbBr_3$ QDs or $CsPbI_3$ QDs, the mixed-halide perovskite $CsPb(Br_xI_{1-x})_3$ QDs (x=0.1, 0.2, 0.3, 0.4) represent a better separation between the absorption and emission spectra (Figure 2.5a). This feature has been associated with a Stokes shift as mentioned above. As shown in Figure 2.5b, mixed-halide perovskite QDs exhibit a two-fold larger Stokes shift compared to $CsPbX_3$ (X=Br, I) QDs, which could reduce the energy loss in large-area LSCs. The large Stokes shift has also been found in small-sized $CsPbI_3$ QDs (< 5 nm) synthesized via a non-injection approach.[69] In colloidal QDs, typically a Stokes shift arises from a combination of the effects of band-edge fine-structure splitting, phonon-assisted emission and size polydispersity.[73,74] Herein, the larger Stokes shift in mixed-halide QDs may originate from their larger size distribution compared to single perovskite QDs. As shown in Figure 2.3, the standard deviation (σ ~15%) of mixed-halide QDs is two-fold of that of pure perovskite QDs (σ ~7%). The larger size distribution leads to the self-

quenching of the PL as high energy photons emitted by smaller QDs may be absorbed by larger QDs with a narrower bandgap.[73] This effect leads to the red-shift of PL peaks and the decrease in PLQY. Because the absorption peak does not change, the red-shifted PL peak leads to a larger Stokes-shift in mixed halide QDs.[73] This self PL quenching also leads to a decrease of QY due to the reabsorption energy loss (Figure 2.5b) in mixed-halide QDs compared to $CsPbBr_3$ QDs. PL decay curves of perovskite QDs with different Br concentrations are shown in Figure 2.5c,d. The PL lifetime of $CsPbBr_3$ QDs is around 9 ns and that of mixed-halide QDs is in the range of 18-21 ns, which are consistent with the reported values for high-QY perovskite QDs.[68] Typically, the PL lifetime of $CsPbI_3$ QDs is longer than those of both $CsPbBr_3$ QDs and mixed-halide QDs. In our case, although the QY of $CsPbI_3$ QDs is lower (~ 20%) which is mainly due to the increase of non-radiative decay rate induced by traps/defects,[48,68,69,71] resulting in shorter PL lifetime, the observed PL lifetime of $CsPbI_3$ QDs (26 ns) is still longer than those of both $CsPbBr_3$ QDs and mixed-halide QDs, consistent with reported values in the literature.

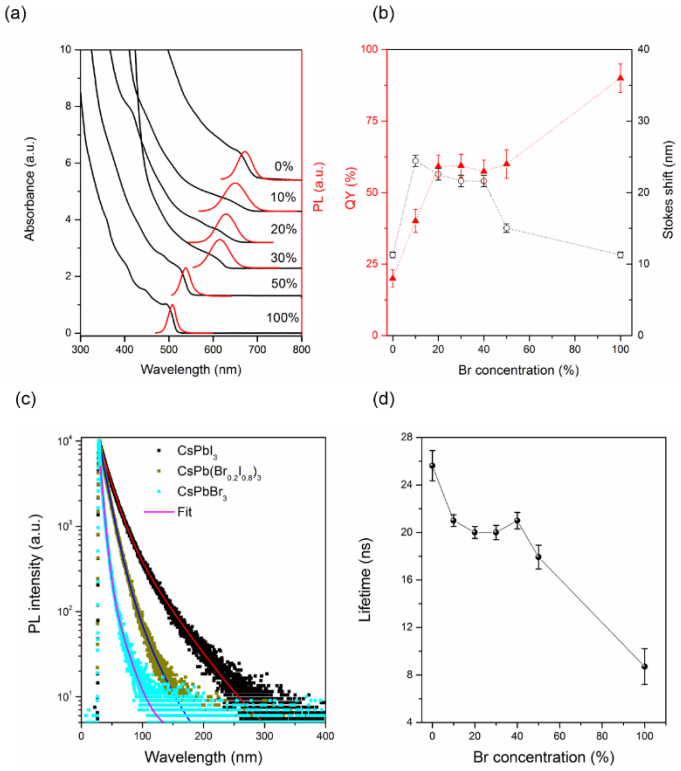

Figure 2.5 (a) Absorption and PL spectra of $CsPb(Br_xI_{1-x})_3$ QDs with various chemical compositions (x = 0-1). (b) QY and Stokes shift variations with various Br concentration. Fluorescence decays (c) and lifetimes (d) of $CsPb(Br_xI_{1-x})_3$ QDs of various chemical compositions in toluene. The excitation wavelength is λex=444 nm. The values of the apparent Stokes shift are obtained from the difference in the positions of the lowest-energy minimum in the second derivative of the absorption spectrum and the PL peak position.

2.2 Fabrication and measurement of perovskite quantum dots based luminescent solar concentrators

By tuning the ratio of Br/I, the Stokes shift engineered perovskite QDs have been synthesized, exhibiting high PLQY (60-90%). In next step, I focus on the fabrication of large-area LSCs using $CsPbBr_3$ and mixed-halide perovskite QDs with different Stokes shifts and PLQYs, and investigate their optical performance and long-term photostability.

2.2.1 Fabrication of perovskite quantum dots based luminescent solar concentrators

We quantify the reabsorption by introduction of a parameter of quality factor (Q_F, defined as the ratio between the absorption coefficient (α_1) at the wavelength λ_1 of collected light and the

absorption coefficient (α_2) at the emission peak) as shown in Figure 2.6.[75] This parameter (Q_F) is four in $CsPb(Br_{0.8}I_{0.2})_3$ QDs, which is four times higher than that of $CsPbBr_3$ QDs (Q_F = 0.97). This is consistent with the larger Stokes shift in mixed-halide QDs, indicating a small overlap of absorption and emission spectra in mixed halide QDs.[75] The as-synthesized perovskite QDs were dispersed into monomers of lauryl methacrylate and crosslinking agent of ethylene glycol dimethacrylate (wt% of 5:1) and a UV initiator (diphenyl(2,4,6-trimethylbenzoyl)phosphine oxide.[22,51,62] Crosslinked poly(lauryl methacrylate) (PLMA) has long side chains that can interact with surface long-chain ligands to prevent agglomeration of the QDs during polymerization.[22,48,51,62] In addition, by carefully controlling the polymerization conditions, such as molar ratio between the monomer and cross-linker, crosslinked PLMA exhibits high-optical-quality, such as high-transparency in the visible and NIR range (> 95%, better than PMMA).[22,46,62] The high quality of PLMA with less unconverted monomers has been widely used as polymer matrix in high efficiency LSCs based on colloidal QDs.[22,46,51,62] As perovskite QDs are very sensitive to moisture, the monomers lauryl methacrylate and ethylene glycol dimethacrylate have to be pumped to remove moisture before mixing with perovskite QDs. After polymerization, perovskite QDs are embedded into crosslinked PLMA-EGDA polymer matrix. As shown in Figure 2.7a, the square large-area LSC (0.2 × 6 × 6 cm^3) appears semi-transparent in ambient environment, and a clear concentrated red light can be seen from the edges (Figure 2.7b), when the top surface of the LSC is partially placed under one sun illumination (100 mW/cm^2). Figure 2.7c presents a photograph of two overlapping LSCs using $CsPbBr_3$ QDs (green) and $CsPb(Br_{0.2}I_{0.8})_3$ (red) QDs under UV illumination, in which both bright green and red emission are clearly visible, indicating the possible fabrication of tandem semi-transparent LSCs using perovskite QDs.[76]

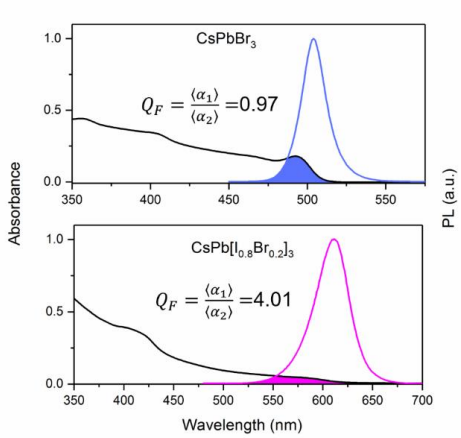

Figure 2.6 Overlap between absorption and emission spectra of the $CsPbBr_3$ and $CsPb(I_{0.8}Br_{0.2})_3$ QDs with similar concentration.

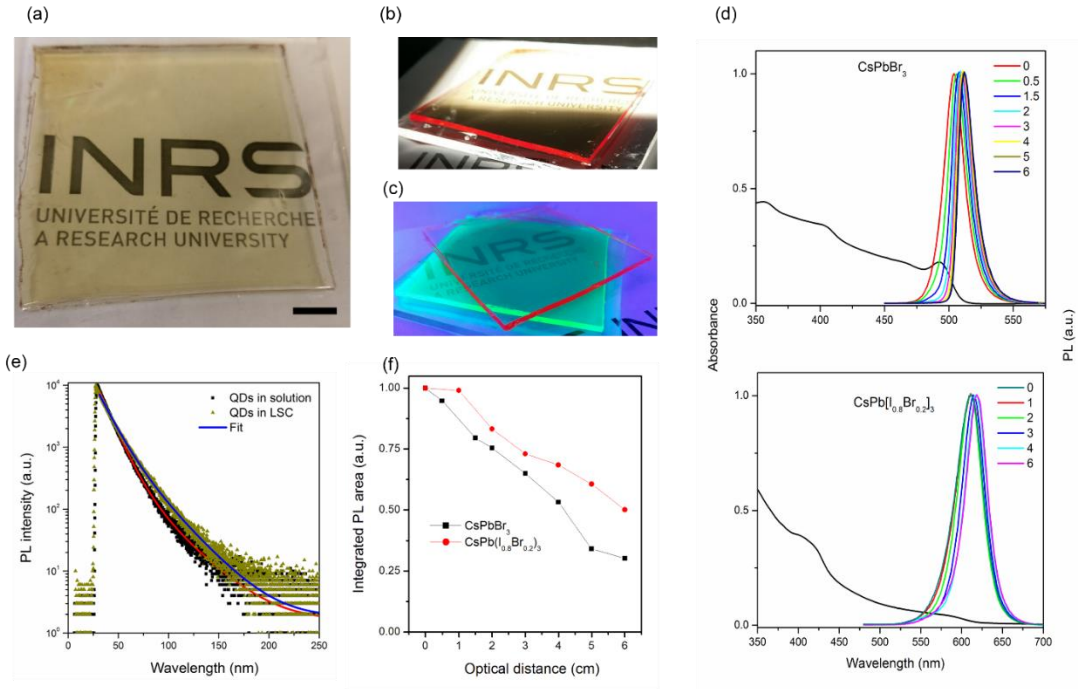

Figure 2.7 Photographs of the LSC comprising $CsPb(Br_{0.2}I_{0.8})_3$ QDs (red light) and $CsPbBr_3$ QDs (green light) under ambient (a), one sun (100 mW/cm^2) (b), and UV illumination (c). LSC dimensions, 6 × 6 × 0.2 cm^3. (d) Absorption and PL spectra measured at different optical paths for the $CsPb(Br_{0.2}I_{0.8})_3$ QD and $CsPbBr_3$ QDs based LSCs. (e) PL decay curves for $CsPb(Br_{0.2}I_{0.8})_3$ QDs in toluene and polymer matrix (excitation at 440 nm). (f) Integrated PL area of $CsPb(Br_{0.2}I_{0.8})_3$ QDs and $CsPbBr_3$ QDs based LSCs at different optical paths.

2.2.2 Optical performance measurement and simulation of perovskite quantum dots based luminescent solar concentrators

LSCs based on mixed-halide perovskite QDs exhibit an absorption spectrum in the wavelength range 300~650 nm (Figure 2.7d). No significant changes in the PL peak positions or FWHM have been found for the investigated samples before (in solution) and after embedding the QDs into the polymer matrix (Figure 2.7c,d). We estimated the relative QYs of QDs in polymer matrix by considering the variations in lifetime.[46,62]

The QY can be expressed as:

$$QY = \frac{k_{\mathrm{rad}}}{k_{\mathrm{nr}}+k_{\mathrm{rad}}} \tag{2.1}$$

Where k_{rad} and k_{nr} are the radiative and the non-radiative decay rate, respectively.

The measured lifetime is equal to:

$$\tau = \frac{1}{k_{\mathrm{rad}}+k_{\mathrm{nr}}} \tag{2.2}$$

The absence of additional non-radiative decay channels (k_{nr}) in the $CsPb(Br_xI_{1-x})_3$ QDs/polymer are confirmed by PL decay measurements, which show identical dynamics for the $CsPb(Br_xI_{1-x})_3$ in toluene and after encapsulation in the polymer (Figure 2.7e), indicating that the preparation process does not lead to the formation of a significant density of surface-defects/traps.[46,77] The polymerization process only affects k_{nr} of QDs.[46] Since the measured lifetime of investigated $CsPb(Br_xI_{1-x})_3$ QDs does not change after embedding them in the polymer, we can deduce that the factor (k_{rad} + k_{nr}) does not change either.[46] This is a clear indication that the mixed-halide QDs embedded in the polymer keep almost the same QY as in solution.[78,79] These results clearly confirm that the mixed-halide $CsPb(Br_xI_{1-x})_3$ QDs present a better photostability under high dose UV

illumination (~40 W/cm^2). The PL does not vary significantly during the further storage of LSCs under ambient condition for 5 months due to the protection of polymer which can protect the QDs from exposure to moisture or oxygen.[48,67,78-80]

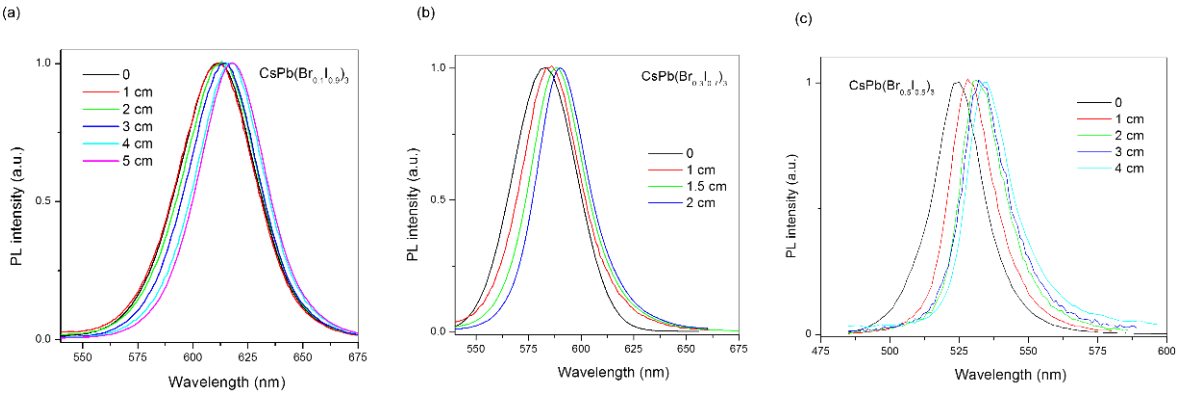

Figure 2.8 PL spectra measured at different optical paths for the LSCs based on $CsPb(Br_{0.1}I_{0.9})_3$ (a), $CsPb(Br_{0.3}I_{0.7})_3$ (b) and $CsPb(Br_{0.5}I_{0.5})_3$ (c).

We further measured the absorption and PL spectra of perovskite QD based LSCs at different optical paths for the mixed-halide $CsPb(Br_xI_{1-x})_3$ and $CsPbBr_3$ QD based LSCs (Figures 2.7d, 2.8). The overlap between absorption and emission spectra is significantly larger in $CsPbBr_3$ compared to $CsPb(Br_{0.2}I_{1-0.8})_3$. Specifically, the PL signals from the LSC are recorded at a certain distance between the edge and vertically illuminated spot at excitation wavelength of 440 nm (Figure 2.8). We plotted the integrated PL area as a function of the optical paths. As shown in Figure 2.7f, the integrated PL area ratio of $CsPb(Br_{0.2}I_{1-0.8})_3$ QDs remains 0.5 in 6-cm LSC, which is higher than 0.3 in 6-cm LSC based on $CsPbBr_3$ QDs due to the escaped and reabsorbed energy loss. The normalized PL spectra are shown in Figure 2.7d. Without reabsorption in QDs based LSC, the PL spectra will not change by increasing the optical path.[22] The change in the PL signal with respect to PL FWHM and PL peak position can only occur due to spectral distortion because of light reabsorption by the perovskite QDs.[48] In our case, by increasing the optical path, the PL spectra of

both types of QDs exhibit a red-shift up to 8 nm with a narrowing of the PL FWHM which confirms the energy loss due to light reabsorption (Figures 2.7d, 2.8). In future work, we plan to investigate the mechanisms of energy loss in LSCs.[81] The reduced reabsorption loss and high external optical efficiency make mixed-halide perovskite QDs potentially excellent candidates for fabricating large-area high-efficiency LSCs.

Standardization of efficiency measurements in LSCs are still an open issue. For this reason, to allow a fair comparison of our results with previous achievements in the literature, in this study we used the set-up described in literature (Figure 2.9).[46,51,62] The LSC (dimension: 0.2 × 1.5 × 11 cm^3) was illuminated perpendicular to its surface by a 1.5 AM global solar simulator (100 mW/cm^2). In the photograph (Figure 2.9a), a standard silicon solar cell with known external quantum efficiency (Figure 2.9b), also called incident photon-to-electron conversion efficiency (IPCE) was coupled with one of the edges of the LSC. Other three edges were coupled by optical mirrors.

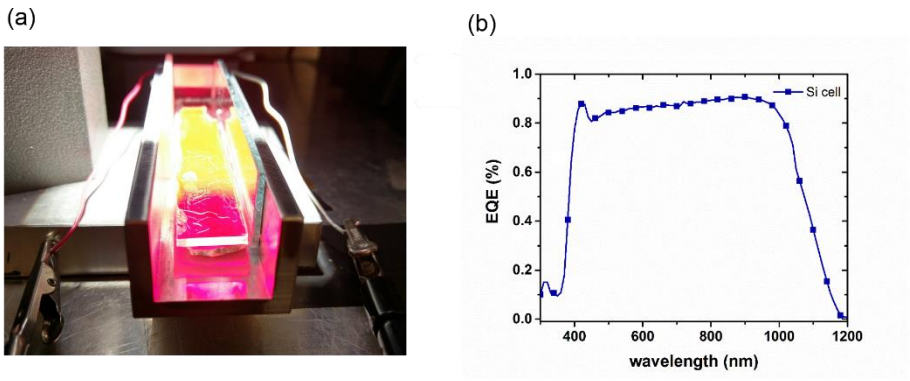

Figure 2.9 (a) Photograph of a perovskite QD based LSC during optical power conversion efficiency measurements with illumination from a solar simulator (1.5 AM global, 100 mW/cm^2). A silicon solar cell (1.5×0.3 cm^2) is coupled with one edge of the LSC. (b) External Quantum Efficiency (EQE) of the Silicon cell used for testing the LSC efficiency.

We also measured the emitted light intensity by coupling a standard power-meter on one of the edges of the LSC. By applying the aforementioned scheme, we estimated the optical efficiency of LSCs as follows. A common method to estimate η_{opt} is to couple a PV cell at the edge of the LSC. In this case, η_{opt} can be calculated as:[23,51,62]

$$\eta_{opt} = \frac{I_{LSC} \cdot A_{PV}}{I_{SC} \cdot A_{LSC}} = \frac{I_{LSC}}{I_{SC} \cdot G} \quad (2.3)$$

Where I_{LSC} is the short circuit current generated by the cell coupled to the LSC, I_{SC} is the short circuit current of the same PV cell under direct illumination, A_{PV} is the area of the edge of the LSC (or the active area on the PV cell, if the area is smaller) and A_{LSC} is the area of the top of the LSC.

As expected, η_{opt} of LSCs using $CsPb(Br_{0.2}I_{0.8})_3$ QDs drops exponentially with the increase of the G factor of the LSCs, which is consistent with our simulation (Figure 2.10).

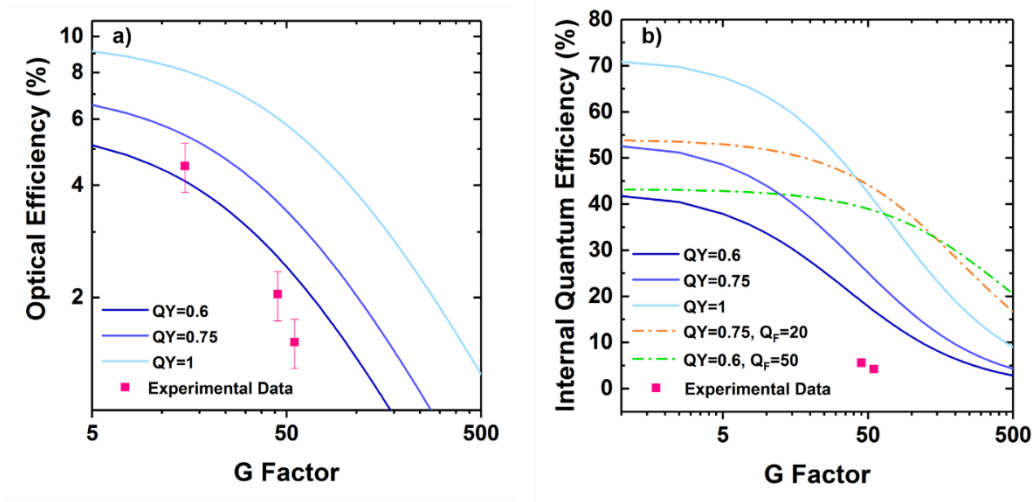

Figure 2.10 External optical efficiency (a) and Internal Quantum Efficiency (b) of $CsPb(Br_{0.2}I_{0.8})_3$ based LSC with the QY varied from 0.6 to 1. The square points are the experimental data obtained with the electro-optical method of comparing the I_{sc}. The dotted lines are calculated for QDs with QY=0.75 and Q_F =20 (red dashed line), QY=0.6 and Q_F =50 (green dashed line).

A maximum external optical efficiency of $\eta_{opt} = 2\%$ is achieved with G of 45 (Figure 2.10a). Increasing the G factor up to 55 (corresponding to a LSC length of 11 cm) η_{opt} decreased to ~1.45% due to reabsorption and scattering loss. The 2% of η_{opt} of LSCs using $CsPb(Br_{0.2}I_{0.8})_3$

QDs is four times higher that of LSC using $CsPbBr_3$ QDs (0.5%) or $CsPbI_3$ (0.4%) with same G factor of 45 and optimal concentration. There is no significant difference in η_{opt} measured by silicon solar cell or power meter. The low external optical efficiency in single perovskite QDs is due to their large overlap between the absorption and emission spectra. Moreover, the η_{opt} of 2% obtained with the mixed-halide perovskite QDs based LSCs is higher than other recent QDs-based LSCs (see Table 2.2). The organic–inorganic hybrid perovskite thin film, e.g. $CH_3NH_3PbI_3$[82] and $CH_3NH_3PbBr_3$[83] have been used as PL emitters for small-sized LSCs with an external optical efficiency of ~13% (1.5×1.5×0.01 mm^3).[82] However due to the strong overlap between the absorption and PL spectra, it is still very challenging to fabricate highly efficient large-area LSCs.

Table 2.2 External optical efficiencies for different LSCs based on QDs and perovskite thin films at different G factors under one sun illumination (100 mW/cm^2).

LSCs	η_{opt} (%)	G factor	LSC dimensions (cm^3)	Ref.
CdSe/CdS QDs	1	43	21.5×1.3×0.5∗	46
CdSe/CdPbS QDs	1.15	45	9×1.3×0.2∗	51
CuInSSe/ZnS QDs	3.2	10	12×12×0.3#	48
$CH_3NH_3PbI_3$ thin film	13	15	1.5×1.5×0.01#	82
Mixed-halide perovskite QDs	2	45	9×1.3×0.2∗	This Work

∗The measurement set up is similar as shown in Figure 2.9, one edge was coupled with PV device. Other three edges of the LSC were coupled by optical mirrors.

#One edge of the LSC was coupled with PV device. Other three edges of the LSC were not coupled by optical mirrors.

In view of the high external optical efficiency obtained at G=45, we further explored the possibility to realize large-area high-efficiency LSCs with perovskite QDs exhibiting higher PLQY or a higher Q_F. We implemented the analytical model of planar LSCs reported in the literature.[75]

Following the formalism developed elsewher,[75] the η_{opt} of the LSC can be expressed as:

$$\eta_{\text{opt}} = \frac{1.05\cdot(1-R)(1-e^{-<\alpha_1>d})\eta_{PL}\eta_{TIR}}{1+\beta\alpha_2 L(1-\eta_{PL}\eta_{TIR})} \quad (2.4)$$

in which $< \alpha_1 >$ is the spectrally averaged absorption coefficient, d is the thickness of the LSC, η_{PL} is the estimated QY of the perovskite QDs, fixed to 0.6; η_{TIR} is the total internal reflection efficiency of the polymer waveguide that can be estimated to be around 73%; β is a numerical value fixed to 1.4 as in ref. 75, α_2 is the absorption coefficient at the wavelength λ_2, peak of the emitted light; R is the fraction of the incident light reflected by the collecting surface , that can be calculated, considering the normal incidence of the simulated sunlight as:

$$R = \frac{(n_{\text{polymer}}-n_{\text{air}})^2}{(n_{\text{polymer}}+n_{\text{air}})^2} \quad (2.5)$$

With the polymer utilized, R can be estimated to be 3%.[51]

To correct the underestimation of the overall efficiency resulting from neglecting effects of reabsorption/reemission within the escape cone, a correction factor of 5% has been introduced.

Because our experimental data on external optical efficiency have been obtained a simulated solar light with non-monochromatic spectrum we used a spectrally averaged absorption coefficient $< \alpha_1 >$ defined as:

$$< \alpha_1 > = -\frac{1}{d} ln\left(\frac{\int_{\lambda 1}^{\infty} S_{in}(\lambda)e^{-\alpha(\lambda)d}d\lambda}{\int_{\lambda 1}^{\infty} S_{in}(\lambda)d\lambda}\right) \quad (2.6)$$

in which λ_1 is the wavelength from which the perovskite QDs start to absorb light, α is the absorption coefficient and S_{in} is the solar irradiance at 1.5G.

To obtain a better fit of the experimental data, α_2 can be replaced by its averaged value $<\alpha_2>$. This allows us to take in account the variation of the absorption coefficient along the emission band. $<\alpha_2>$ can be determined as follows:

$$<\alpha_2> = \frac{\int S_{\mathrm{PL}}(\lambda)\alpha(\lambda)d\lambda}{\int S_{\mathrm{PL}}(\lambda)d\lambda} \quad (2.7)$$

in which $S_{PL}(\lambda)$ is the PL emission spectrum.

From (1) it is also able to obtain the internal quantum efficiency (IQE) as:

$$IQE = \frac{\eta_{\mathrm{PL}}\eta_{TIR}}{1+\beta<\alpha_2>L(1-\eta_{\mathrm{PL}}\eta_{\mathrm{TIR}})} \quad (2.8)$$

The concentration factor (C) is defined as $C = G\times\eta_{opt}$.[84,85]

In addition to the experimental points for the C we also added a simulation for larger LSCs and with perovskite QDs up to 100% of QY. In this case C was calculated as follows:

$$C = \frac{(1-R)(1-e^{-<\alpha_1>d})\eta_{PL}\eta_{TIR}}{1+\beta\alpha_2 L(1-\eta_{PL}\eta_{TIR})}\left(\frac{L}{d}\right) \quad (2.9)$$

Where L is the LSC length and d is the thickness.

With the above mentioned formalisms, we can accurately fit the results of the η_{opt}, C and IQE as reported in Figure 2.10. The IQE represents the number of photons emitted by the edge of the LSC over the number of photons absorbed by the LSC. We observe the consequence of an increase in the QY of the $CsPb(Br_{0.2}I_{0.8})_3$ QDs: increasing the QY up to 75% (from 60% of synthesized QDs) the efficiency would increase to 3.6% at G=45 and 5.9% at G=10 respectively. An ideal $CsPb(Br_{0.2}I_{0.8})_3$ QDs, with QY of 1, would have a maximum η_{opt} of more than 6 % at G=45.

Improving the PL QY from 0.6 to values close to 1 can be very challenging because the as-prepared perovskite QDs should have almost perfect crystal structure without any defects/traps and very narrow size distribution (σ ~15%) to avoid any of the self-PL quenching due to the spectral overlap between the luminescence and absorption. Such improvements can potentially be achieved by surface treatment of perovskite QDs or selection of appropriate precursors in reaction system, and refining reaction conditions to synthesize QDs with high PL QY and very narrow size distribution. Another possible way to increase the external optical efficiency is to increase the Q_F.[75] Figure 2.10b reports simulation results of the effect of increasing Q_F (and so the Stokes-shift) of the $CsPb(Br_{0.2}I_{0.8})_3$ QDs on the internal quantum efficiency of the LSC. For example, with a QY=75% and Q_F=20 it is possible to achieve the same efficiency at G=45 as in the case of QDs with QY of 100%. Preserving the same QY of synthesized QDs, but with a Q_F improved to 50, we could achieve similar performance of the LSC with QDs with either QY of 1 (at G=70) or with QY of 0.75 (at G=12.5).[75] The concentration factor C was also calculated and the detail is included in Figure 2.11.

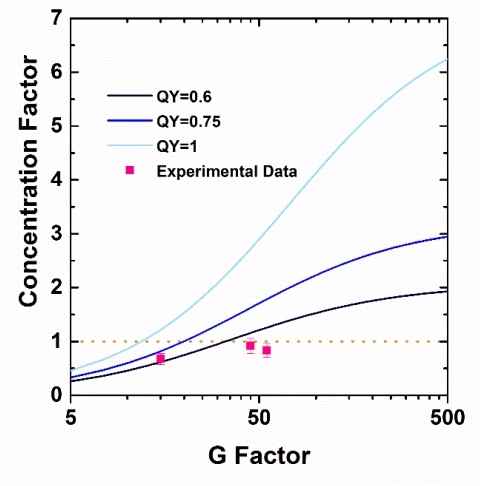

Figure 2. 11 Calculated and experimental concentration factor as a function of G factor for QDs with QY=0.6, 0.75 and 1.

Compared to colloidal perovskite QDs which lack long-term stability due to the sensitivity of the moisture, after encapsulation of perovskite QDs into the polymer matrix, the LSCs exhibit very good stability with respect to photocorrosion. After UV illumination (20 mW/cm^2) for 14 hours, the optical properties of perovskite QDs or mixed halide perovskite QDs based LSCs (PL intensity, PL peak position and PL FWHM) do not show a significant change compared to their values UV illumination (Figure 2.12). Upon exposure to a high dose of UV illumination (100 mW/cm^2, equal to 20 sun illumination),[48] within the first four hours, the PL peak position and PL FWHM of the perovskite QDs do not change significantly compared to their values before and after UV illumination (Figure 2.12). Similarly, the PL lifetime of perovskite QDs of both $CsPbBr_3$ and $CsPb(Br_{0.2}I_{0.8})_3$ in polymer matrix exhibit similar values and before and after UV exposure (Figure 2.13). When increasing the illumination time (10 hours), the PL intensity still maintains over 90% of its intensity for both bare and mixed-halide perovskite QDs based LSCs (Figure 2.13). Extended UV illumination leads to a decrease in PL intensity, but the PL peak position and PL FWHM do not change significantly. Significant variations in PL FWHM and PL peak positions are generally attributed to a phase segregation which creates iodide-rich and bromide-rich domains in mixed-halide perovskite QDs. Therefore we believe that in our case this phase segregation did not occur.[79] A similar remarkable photostability has been reported for perovskite QDs films under continuous pulsed laser excitation in ambient conditions for at least 34 h (corresponding to 1.2×10^8 laser shots, 12 mJ/cm^2).[78] In addition, there is no significant change regarding the color and external optical efficiency of the LSCs after storing at ambient conditions for more than three months. This indicates better photostability compared to LSCs based on perovskite thin films, in which the external optical efficiency drops by 15% after four-week storage.[82] These results indicate that inorganic perovskite QDs based LSCs are very promising for solar energy applications.

As lead is toxic,[86] future work should focus on the synthesis of lead-free perovskite QDs, such as bismuth halide perovskite QDs ($MA_3Bi_2Br_9$)[87] and tin halide perovskite QDs ($CsSnI_3$).[88] Mixed-halide perovskite QDs based on Bi and Sn may present a promising emitter for large-scale LSCs.

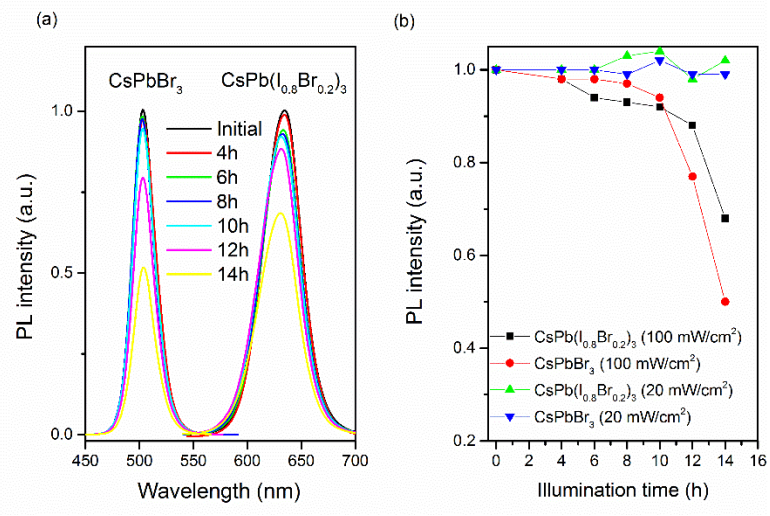

Figure 2.12 PL spectra (a) and PL intensity (b) of $CsPbBr_3$ (b) and $CsPb(Br_{0.2}I_{0.8})_3$ (c) QDs based LSCs upon UV exposure for different hours.

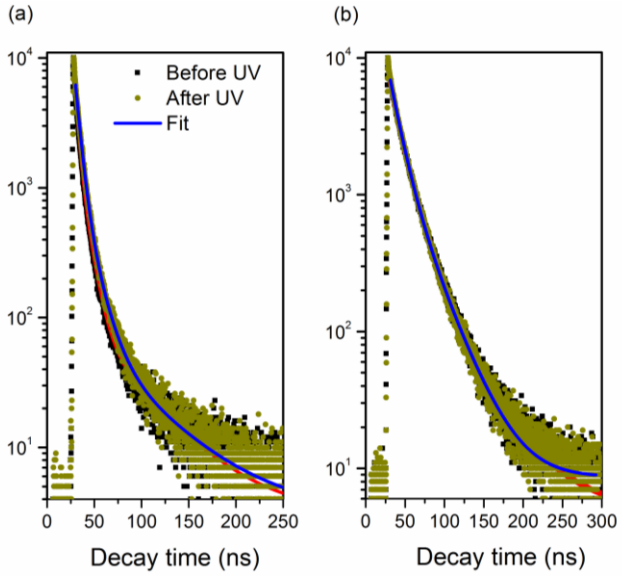

Figure 2.13 PL decay curves of $CsPbBr_3$ (a) and $CsPb(Br_{0.2}I_{0.8})_3$ (b) QDs based LSCs without or with UV exposure (100 mW/cm^2) for four hours.

2.3 Summary

We demonstrated large-area and high-efficiency LSCs based on colloidal $CsPb(Br_xI_{1-x})_3$ QDs dispersed in a polymer matrix. By tuning the chemical composition of Br/I, the Stokes shift of QDs can be efficiently enlarged, leading to a better separation between the absorption and emission spectra. The as-prepared mixed-halide perovskite QDs exhibit a high PLQY over 60% with good photostability. Due to the broad absorption and relatively low reabsorption loss, large-area LSCs based on $CsPb(Br_{0.2}I_{0.8})_3$ QDs exhibit an external optical efficiency of 2% (G = 45). The LSCs exhibit long-term air stability without any noticeable variations in PL intensity and lifetime under 4 W UV light illumination for over four hours. The concept can be applied in NIR LSCs by tailoring the chemical composition of the perovskites, such as $Cs(Pb_ySn_{1-y})(Br_xI_{1-x})_3$ QDs or lead-free $CsSn(Br_xI_{1-x})_3$. In view of the simple synthesis procedure and excellent optical properties of $CsPb(Br_xI_{1-x})_3$ QDs, they represent practical emitter for large-area, high efficiency LSCs and are also promising candidates for other optoelectronic applications, such as light emitting devices, field effect transistors (FETs) and solar cells.

Chapter 3 Synthesis and characterization of PbS/CdS core/shell quantum dots based luminescent solar concentrator

In Chapter 2, we introduced high PLQY mixed-halide perovskite QDs for LSCs application. However, the Stokes shift of mixed-halide perovskite QDs is still relatively small, resulting in strong reabsorption issue when the dimension of LSC is getting larger. In addition, the absorption of mentioned mixed-halide perovskite QDs is in the UV-vis range, which is not sufficient for the utilization of solar irradiation. To extend the absorption range and enhance the Stokes shift of PL emitter for LSCs application, in this chapter, we synthesized NIR PbS/CdS core/shell QDs with engineered Stokes shift by varying the core size and shell thickness. The optical properties of large-area PbS/CdS core/shell QDs based LSCs (scheme in Figure 3.1a) is also investigated.

3.1 Synthesis and characterization of PbS/CdS core/shell quantum dots

To alleviate the reabsorption loss in QDs based LSCs, transition-metal ions (such as Cu or Mn) doped QDs or hetero-structured QDs with small overlap of absorption and emission spectra have been used for LSCs application.[33,89-93] For example, Meinardi *et al*. developed a large-area LSC based on giant CdSe/CdS core/shell QDs embedded in a mass-polymerized poly(methyl methacrylate) (PMMA) matrix with conversion efficiency per incident photon over 1%.[46] However, currently, both LSCs based on doped QDs or giant core/shell QDs mainly absorb in the ultraviolet/visible (UV/Vis) spectral range (usually < 500 nm), leaving more than 60% of solar radiation unabsorbed, which strongly limits their application in PV.

Spectrally-tunable near infrared (NIR) QDs (such as lead chalcogenides) have large absorption cross-sections and the NIR absorption onset is well-suited for harvesting solar radiation. In particular, commercial Si solar cells are photoactive in the 400-1000 nm range, perfectly matching optical emission from NIR QD-based LSCs. In addition, NIR QDs enable the realization of high transparency colourless QD-doped slabs by tuning their sizes and/or compositions that can act as neutral-density filters, and therefore well-suited for applications as semitransparent windows.[48] Recently, NIR fluorophores have been employed in LSCs.[94-96] However, it is difficult to synthesize large-area high efficiency NIR QD-based LSCs due to three main factors: (1) the QY drops during LSC fabrication due to the chemical and thermal sensitivity of QDs to the surrounding environment;[97] (2) the strong re-absorption due to the limited Stokes shift and the large overlap of absorption and emission spectra; (3) the limited long-term photo-stability. All these challenges can be addressed by using core/shell NIR QDs, such as PbSe/CdSe or PbS/CdS QDs due to their high QY, and chemical- and photo-stability with respect to bare QDs.[98]

In this chapter, we synthesized the core/shell PbS/CdS QDs with tunable core size and shell thickness. The Stokes shift of the core/shell QDs with high PLQY (40~50%)[99] can be largely increased by engineering the band structure compared to bare QDs, due to the strong core-to-shell leakage of electrons, when the core size is less than 3 nm in diameter and the shell is thicker than 0.5 nm.

3.1.1 Synthesis of PbS/CdS core/shell quantum dots

Colloidal size-tunable PbS QDs with narrow size distribution (σ < 10%) were synthesized according to procedures described elsewhere,[99] and were subsequently used to synthesize PbS/CdS core/shell QDs via a cation exchange approach.[100] This approach leads to a core/shell structure to either PbS/CdS or PbSe/CdSe QDs.[98]

Typically, $PbCl_2$ (3.6 mmol) in OLA (2.4 mL) and sulfur (0.36 mmol) in OLA (0.24 mL) were purged, respectively, by N_2 at room temperature for 30 min. The $PbCl_2$-OLA suspension was heated to 160 °C for 1 hour. The $PbCl_2$-OLA suspension was cooled to 80 °C under vacuum for 30 min. The flask was then reopened and the N_2 flux was restored. Sulfur in OLA at room temperature was quickly injected into the $PbCl_2$-OLA suspension under vigorous stirring. The reaction cell was quenched with cold water after the growth reaction was conducted at 100 °C for 1- 360 min. The size of PbS QDs can be tuned from 3.4 to 6 nm by adjusting the molar ratio of Pb/S, injection temperature and growth time.

PbS QDs with diameter of less than 3.0 nm were synthesized by using OA as ligand. In a typical synthesis experiment, a mixture of lead acetate trihydrate (1 mmol), OA (1.2 mL), trioctylphosphine (TOP) (1 mL), and ODE (15 mL) were heated to 150 °C for 1 h. Then, the system was cooled to ~100 °C in N_2 atmosphere for 15 min. Subsequently, the solution containing 0.5 mmol bis(trimethylsilyl) sulfide ($(TMS)_2S$), 0.2 mL of TOP and 4.8 mL of ODE was quickly (less than 1 second) injected into the reaction flask at 130 °C; then, the reaction was cooled down to room temperature by immersing the reaction flask into cold water. PbS QDs were precipitated with ethanol, centrifuged to remove unreacted lead oleate and free OA molecules and then re-dispersed in toluene.

PbS/CdS core/shell QDs were synthesized via a cation exchange method.[99] Typically, CdO (2.3 mmol), OA (2 mL) and ODE (10 mL) were heated to 255 °C under N_2 for 20 min. The clear solution was cooled to 155 °C under vacuum for 15 min. The flask was then reopened and the N_2 flux was restored. PbS QDs suspension in toluene (1 mL, Absorbance = 3 at the first excitonic peak) was diluted in 10 mL toluene, bubbled for 30 min and then heated to 100 °C in less than 5

minutes. The Cd/OA mixture was injected. The reaction cell was quenched with cold water after the growth reaction was conducted at 100 °C for different times. PbS/CdS QDs with tunable core size and shell thickness of 0.1~0.7 nm were synthesized by choosing different starting PbS sizes together with different reaction parameters (Pb-to-Cd ratio and reaction time).

3.1.2 Structure and engineered Stokes shift in PbS/CdS core/shell quantum dots

A representative TEM image (Figure 3.1d) confirms that the PbS/CdS QDs synthesized via this approach have a uniform size distribution. In addition, as we previously reported, the shell is mainly composed of CdS, rather than alloyed $Pb_xCd_{1-x}S$,[99] which guarantees an excellent chemical stability due to the protection of pure chemically stable CdS. The average diameter of the bare PbS QDs was estimated from TEM images. For the core/shell QDs, the Pb-to-Cd atomic ratio was first determined by an inductively-coupled plasma-optical emission spectrometer. Using this ratio and the overall diameter from TEM images, the diameter of the remaining PbS core and the thickness of the shell were estimated by using the approach presented in reference.[101] By carefully controlling the reaction parameters such as time, temperature and starting size of bare PbS QDs, we successfully synthesized PbS/CdS core/shell QDs with tunable size and shell thickness. The PbS core radius (R) ranges from 1.3 to 3.3 nm (emission peak: 0.8 ~1.4 eV; Figure 3.1e), with shell thickness of 0.1~0.7 nm. The representative absorption and PL spectra of samples in solution containing various sizes of PbS and PbS/CdS QDs are shown in Figures 3.1b and 3.1c. Both the first excitonic absorption and emission peaks are clearly observed for these samples. For QDs with R of 2.3 nm, with increasing shell thickness (H) from 0 to 0.7 nm, the Stokes shifts exhibit limited variation, compared to bare PbS QDs (Figure 3.1c). On the contrary, in the QDs with R of 1.5 nm, the Stokes shift increases significantly with increasing shell thickness (Figure 3.1b).

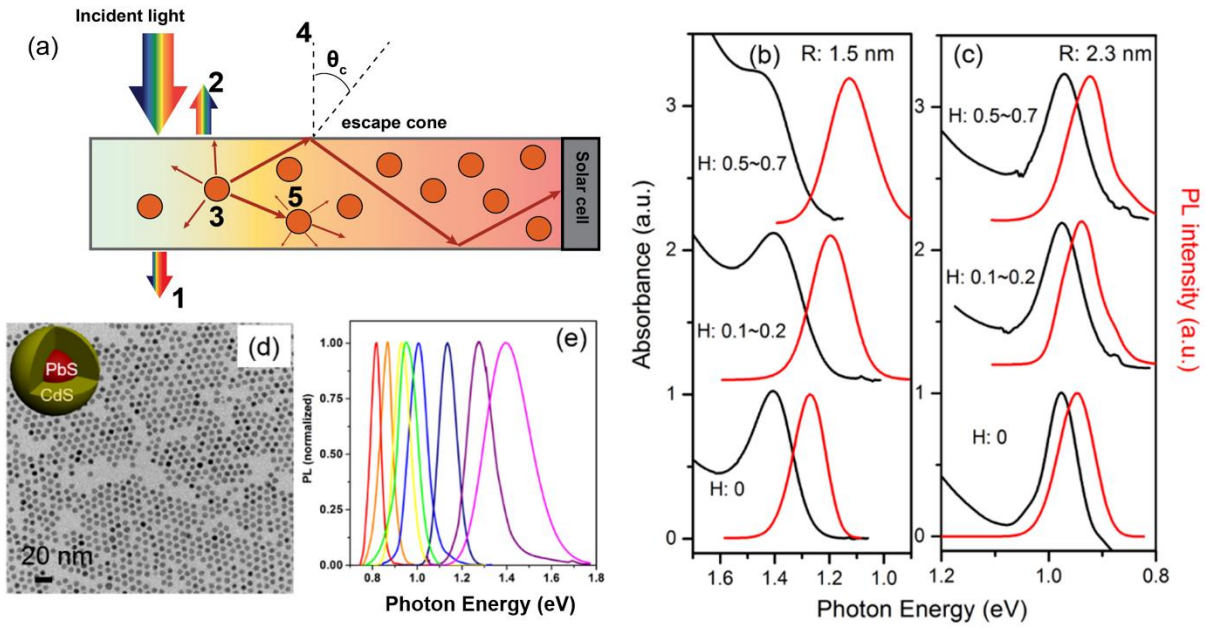

Figure 3.1 (a) Illustration of QD-based LSC incorporated with a PV device, including the typical processes of energy loss in an LSC. (1) Unabsorbed (transmitted) light; (2) Light reflected from the top surface; (3) Light absorbed by the QDs, but partial energy loss due to fluorescence QY below 100%; (4) Re-emitted incident light escaping from the surface, due to the escape cone. (5) Light re-absorbed by another QD. (b-c) Normalized absorption and PL spectra of QDs with core radius of 1.5 nm (b) and 2.3 nm (c) with tunable CdS shell thickness (H, 0~0.7 nm). (d) Representative TEM image of the core/shell PbS/CdS QDs. The inset shows the structure diagram of a core/shell PbS/CdS QD. (e) PL spectra of the core/shell QDs with various core sizes and shell thicknesses.

3.1.3 Optical properties and theoretical calculation

To understand the observed differences in Stokes shifts, we calculated the electron wave functions of a QD (R: 3 nm; H: 0~0.6 nm) based on its bulk band alignment (Figures 3.2b,d). In these calculations, we solved the stationary Schrödinger equation in spherical geometry, in which we used the bulk values for the effective masses of electrons (m_e*) and holes (m_h*), namely m_e* = 0.085 m_e and m_h* = 0.085 m_e for PbS, and m_e* = 0.2 m_e and m_h* = 0.7 m_e for CdS, where m_e is the electron mass at rest in vacuum.[102] The potentials for electrons and holes as a function of position were approximated as the lowest unoccupied molecular orbital and highest occupied molecular orbital levels, respectively, for the bulk materials.[103] The interaction between electrons and holes was neglected in the calculations.

Figure 3.2d shows the radial distribution functions of 1S electrons in the QD as a function of the radial distance from the QD's center. Electrons have a high probability of penetrating deeply into the CdS layer and even further, entering the out-layer of the QD surface,[103,104] although the amplitude of their wave function decays throughout the shell thickness, especially for thicker shells. These findings describe the size- and shell thickness-dependent Stokes shifts in core/shell QDs, which is due to the efficient electron leakage, similar to what was reported in PbSe/CdSe QDs.[105] In general, this leakage effect can lead to a red-shift of the PL peak position and longer lifetime with respect to bare QDs (Figure 3.2c). PL lifetimes of QDs are calculated using triple-exponential decay function.[106] The detailed fitting procedure, parameters and calculated lifetimes are shown in Table 3.1.

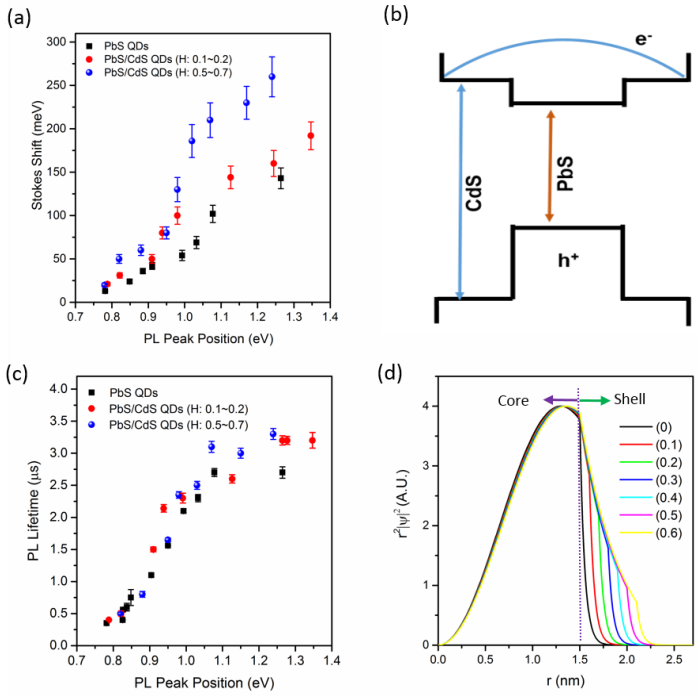

Figure 3.2 (a) Stokes shift of QDs with various shell thicknesses as a function of the PL peak position (related to core size of diameter from 3 to 6 nm). (b) Approximate electronic band structure of a core/shell PbS/CdS QD. (c) PL lifetime of QDs with various shell thicknesses as a function of the PL peak position (related to core size of diameter from 3to 6 nm). (d) Radial distribution functions for 1S electron of a PbS QD with the core size of 3.0 nm in diameter and tunable shell thickness of 0~0.6 nm.

Table 3.1 Relevant parameters of the investigated PbS and PbS/CdS QDs with thin shell (shell thickness of 0.1~0.2 nm) or thick shell (shell thickness of 0.5~0.7 nm). Energies corresponding to PL maximum for QDs in toluene and average lifetime and QY of QDs in toluene are reported.

Samples	PL peak position (eV)	Average lifetime (μs)*	PLQY (%)
PbS#1	1.26	2.7	80
PbS#2	1.07	2.7	70
PbS#3	1.03	2.3	60
PbS#4	0.99	2.1	40
PbS#5	0.95	1.56	28
PbS#6	0.90	1.1	26
PbS#7	0.84	0.75	20
PbS#8	0.84	0.6	20
PbS#9	0.83	0.56	15
PbS#10	0.82	0.4	12
PbS#11	0.78	0.35	10
PbS/CdS#1_thin	1.35	3.2	60
PbS/CdS #2_thin	1.28	3.2	71
PbS/CdS #3_thin	1.26	3.2	63
PbS/CdS #4_thin	1.13	2.6	38
PbS/CdS #5_thin	0.99	2.3	40
PbS/CdS #6_thin	0.94	2.14	35
PbS/CdS #7_thin	0.91	1.5	30
PbS/CdS #8_thin	0.82	0.5	25
PbS/CdS #9_thin	0.79	0.4	20
PbS/CdS#1_thick	1.239	3.3	40
PbS/CdS #2_thick	1.15	3	40
PbS/CdS #3_thick	1.07	3.1	40
PbS/CdS #4_thick	1.03	2.5	35
PbS/CdS #5_thick	0.98	2.35	30
PbS/CdS #6_thick	0.82	0.5	15

For all the samples, the decay curves of the PL peak centered at different wavelengths of PbS/CdS QDs are well fitted by a three-component decay. The intensity-weighted average lifetime $<\tau>$ is estimated as follows, and the quantitative results are reported in Table 3.1.

$$<\tau>=\frac{a_1\tau_1^2+a_2\tau_2^2+a_3\tau_3^2}{a_1\tau_1+a_2\tau_2+a_3\tau_3} \quad (3.1)$$

Where a_i (i=1,2,3) are the coefficients of the fitting of PL decay and τ_i (i=1,2,3) are the lifetimes. The PL lifetimes of bare PbS QDs increase with increasing PL peak position, which is correlated with R of QDs from ~0.4 μs (~0.8 eV) to ~2.7 μs (~1.05 eV) and remain almost constant after ~1.05 eV. These lifetime values of bare PbS QDs are consistent with the reported values for PbS QDs dispersed in organic solvents,[107,108] while the lifetimes of the core/shell QDs with PL peak position (eV) higher than ~0.95 eV are longer than those of the pure PbS QDs (Figure 3.3). The long lifetime value is usually attributed to the decrease of quantum confinement due to the leakage of electrons.[105] The aforementioned results confirm that we can achieve QDs with larger Stokes shifts with respect to bare QDs by tuning the core size and shell thickness. In addition, the as-synthesized core/shell QDs with shell thickness of 0.5~0.7 nm still show a high QY of ~40~50 %, making them good candidates for high efficiency LSCs.

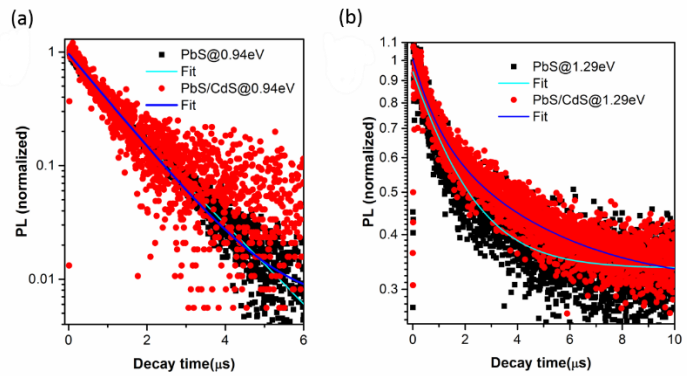

Figure 3.3 (a-b) Fluorescence decays of PbS QDs and corresponding core/shell PbS/CdS QDs in solution with absorption energy of 0.94 eV (a) and 1.29 eV (b). The excitation is at 2.79 eV.

3.2 Fabrication and measurement of PbS/CdS core/shell quantum dots based luminescent solar concentrators

In this section, engineered Stokes shift PbS/CdS core/shell QDs with high QY and broad absorption in NIR region, has been used as PL emitter for large-area LSCs application. The optical performance and photostability of LSCs are also discussed. The results suggested that this type of QDs is a promising candidate for high efficient large-area LSCs.

3.2.1 Fabrication of PbS/CdS core/shell quantum dots based luminescent solar concentrators

To experimentally compare the efficiency of the LSCs, we fabricated the QD-based LSCs (5 cm × 1.5 cm × 0.3 cm) by embedding the bare and core/shell QDs with tunable size and shell thickness in a polymer matrix, the fabrication procedure of which is the same as the preparation in chapter 2.[51] The geometric factor G defined by the ratio of the area of the top surface and the surface area of the edge facing the solar cell (the other three edges being covered by the mirrors) is ~16. In the following, the small and large sized PbS QDs are labeled as PbS_S and PbS_L; the small and large sized core/shell QDs are labeled as C@S_S and the C@S_L, respectively. Moreover, I synthesized

and investigated the optical performance of large-area LSC based on C@S_S QDs (G=50) with large Stokes shift.

3.2.2 Optical performance measurements of PbS/CdS core/shell quantum dots based luminescent solar concentrators

A red-shift in PL peak and the decrease in PL lifetime were found in the bare QDs after being transferred from solution into the polymer matrix (Figure 3.4a, c-d), while no significant changes were observed in the PL peak position, the full width at half maximum (FWHM) of the PL spectra or lifetime for the investigated core/shell samples (Figure 3.4b, e-f). Typically, the variation of PL peak, FWHM and lifetime could be affected by surface traps/defects,[109] which form during the LSC synthesis process that involves the phase transfer process and high dose UV irradiation for polymerization. The optical properties (PL peak, FWHM and lifetime) in core/shell QDs after fabrication suggest the higher chemical and photo-stability of the core/shell QDs benefiting from their CdS shell protection compared to bare QDs. As the presence of surface traps/defects can also affect the QY of QDs inside the polymer matrix, we estimated the QY variation according to the following equation:[110]

$$\mathrm{QY} = \frac{\tau_{meas}}{\tau_{rad}} = \frac{\tau_{nr}}{\tau_{nr}+\tau_{rad}} \tag{3.2}$$

Where τ_{meas}, τ_{rad} and τ_{nr} are the measured PL lifetime, and the radiative and non-radiative lifetime, respectively. As the non-radiative lifetime is more sensitive to the surface chemical state,[111] the decrease of lifetime between bare QDs in solution (2.74 μs) and in the polymer matrix (2.46 μs) is mainly due to the decrease of non-radiative lifetime, indicating a drop of QY for bare PbS QDs. The smaller change of lifetime in the core/shell QDs indicates that the QY does not change significantly.

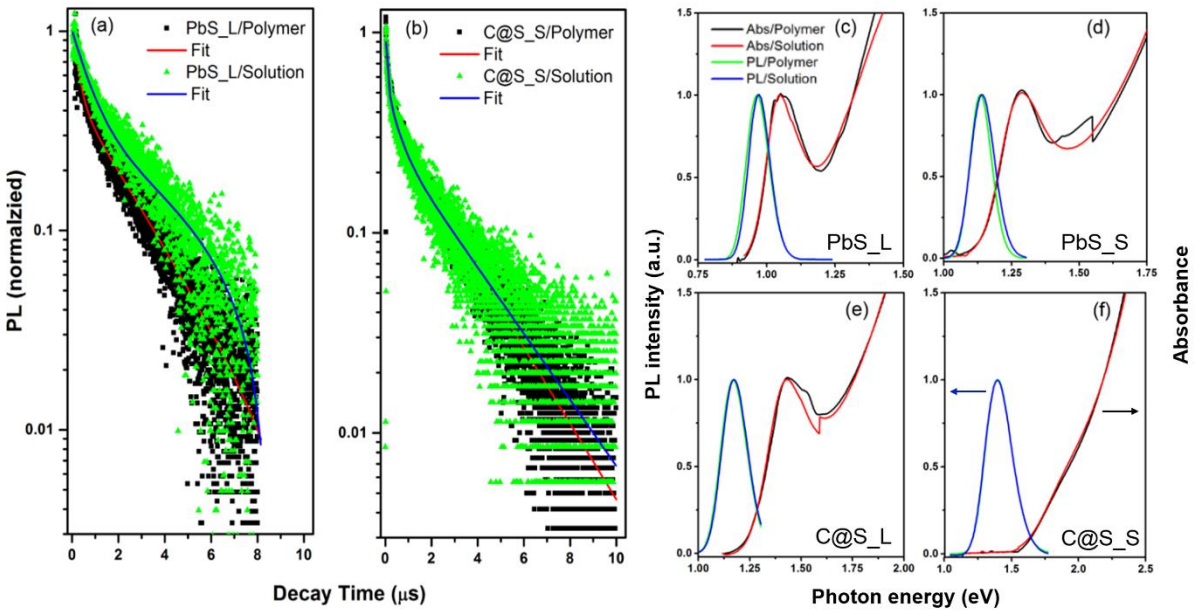

Figure 3.4 (a-b) PL decays of the large sized PbS QDs (PbS_L) (a) and the small sized core/shell QDs (C@S_S) (b) in solution or in polymer. (c-f) Absorption (red/black) and PL (green/blue) spectra of QDs in solution and in polymer for the PbS_L (c), the small sized PbS QDs (PbS_S) (d), the C@S_L (e) and the C@S_S (f).

Furthermore, we characterized the optical properties of LSCs fabricated using the aforementioned QDs. We measured the PL intensity as a function of the optical path (Figure 3.5). The PL intensity of the LSC is collected at a certain distance from the edge while perpendicularly illuminated at wavelength 670 nm, which characterizes the optical performance of QD-based LSCs. As shown in Figure 3.5a, the PL peak position for PbS_L sample is red-shifted with the increase of the optical path due to the strong overlap between the absorption and emission spectra, which causes strong re-absorption. At 4-cm optical path, the PL intensity is reduced to 40% of its initial value (Figure 3.6a). Also, the PL FWHM becomes narrower due to the multiple re-absorption/re-emission process, as seen from the FWHM ratio, which expresses the ratio of the FWHM at a certain optical path and at the starting point of the LSC (optical path ~0 cm). Similar results of red-shifted PL peak, decreasing PL intensity and FWHM ratio with the extended optical path were observed for PbS_S and C@S_L samples (Figures 3.6, 3.7). However, a dramatic difference is found in C@S_S

sample (Figure 3.5b). The shapes of the PL spectra for C@S_S sample remain unchanged along the optical path as long as 5 cm, as well as the PL peak position (Figure 3.6b) and PL FWHM ratio (Figure 3.6c). Additionally, the integrated PL signal exhibits a weak attenuation (10%) at an optical path of 4.5 cm due to scattering, indicating the high optical performance of the C@S_S QD-based LSC.

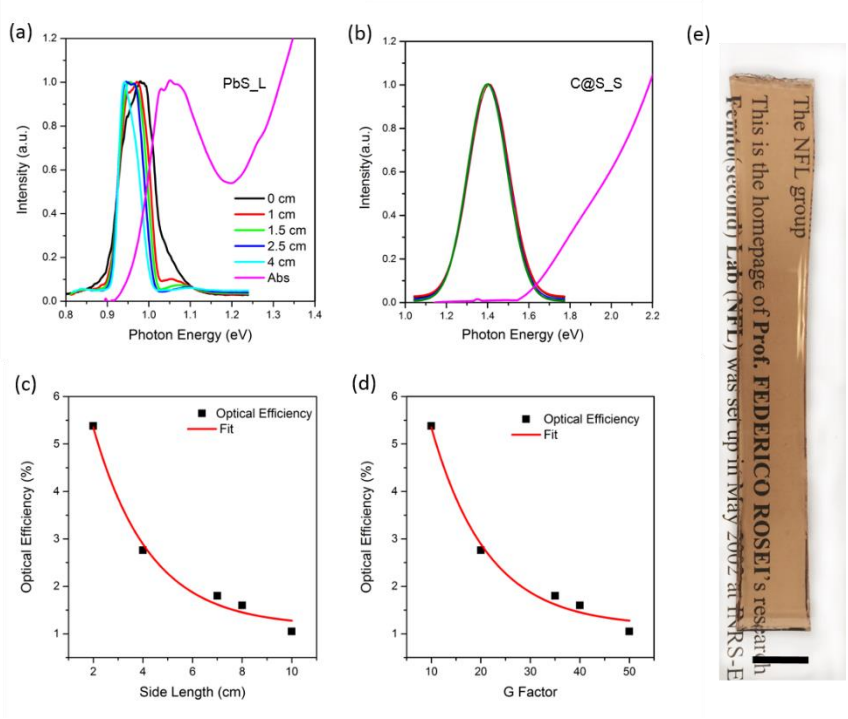

Figure 3.5 (a-b) Normalized absorption and PL spectra measured at different optical paths for the samples of the PbS_L QDs (a) and the C@S_S QDs (b). (c-d) Optical efficiency of C@S_S QD-based LSC (#1) coupled with Si diode as a function of side length (c) or geometric factor (G factor) (d). (e) Photograph of a QD-polymer-based LSC (#1, dimension: 10 cm × 1.5 cm × 0.2 cm) comprising C@S_S QDs in ambient light. Scale bar is 1 cm.

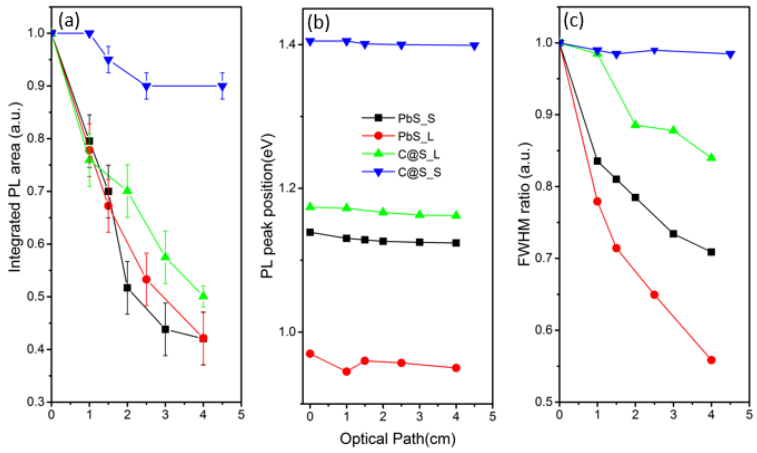

Figure 3.6 (a-c) Spectral integrated PL area (a), PL peak position in eV (b) and FWHM ratios (c) plotted as a function of an optical path for the investigated samples.

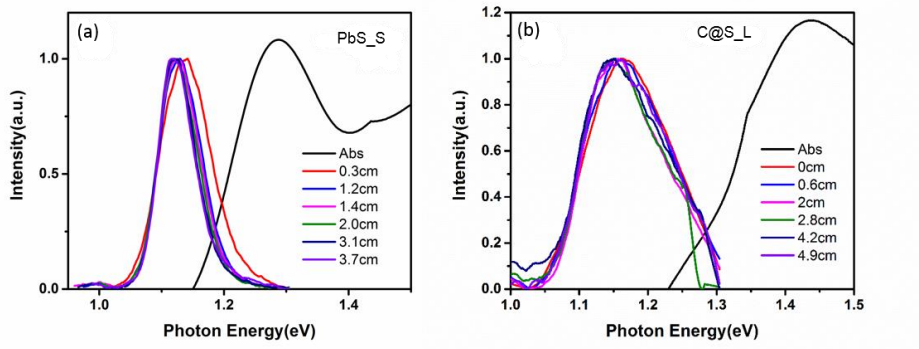

Figure 3.7 (a-b) Normalized absorption and PL spectra measured at different optical paths for the PbS_S QD-based LSCs (a) and the C@S_L QD-based LSCs (b).

Eventually, I fabricated a large-area semi-transparent C@S_S QD-based LSC as large as 10 cm × 1.5 cm ×0.2 cm (Figure 3.5e). Strong absorption of the LSC with different concentrations of C@S_S QDs in the UV range and continuously extending to the NIR region can be found in Figure 3.8a, which is consistent with the absorption nature of C@S_S QDs. Also, semi-transparency of LSCs in Vis-NIR range is confirmed by optical transmittance (Figure 3.8b), which can be varied by different concentrations of QDs in LSCs.

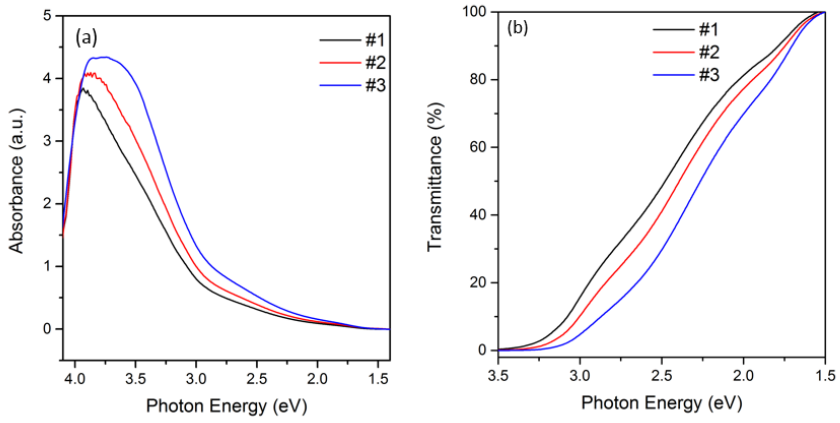

Figure 3.8 (a-b) Absorption spectra (a) and transmission spectra (b) of C@S_S QD-based LSC samples with concentration of QDs increasing from sample #1 to #3.

The concentration of QDs is calculated using the Beer-Lambert's law.[100] To measure the efficiency of LSCs, we integrated a Si diode into semi-transparent C@S_S QD-based LSC, and estimated the optical efficiency (η_{opt}) of LSC. The measurement and calculation of optical efficiency (equation 2.3) follow the procedure and method based on our previously work illustrated in chapter 2.

LSCs with different size (in the range 2-10 cm in length) for testing their optical efficiency were fabricated. Each LSC was fully illuminated perpendicularly to its surface by a 1.5 AM global solar simulator (100 mW/cm^2). A commercial Si diode (IXYS KXOB22) was positioned at the end of the LSC. To keep the system as simple as possible, the coupling between the cell and the LSC was purely mechanical, through commercial tape. The other edges were fully covered by commercial mirrors to limit photon losses (scheme in Figure 2.9a). The external quantum efficiency (EQE) spectrum of reference Si diode are shown in Figure 2.9b. Similar set-ups, which include full illumination of the active area of the LSC can be found in literature for calculation of LSC efficiency.[23,26,46] The η_{opt} exhibits an exponential decrease with increasing side length or geometric factor G of LSC (Figure 3.5c-d), which is also observed in the literature.[112] With the

side length of LSC extended to 4 cm (G = 22.5), η_{opt} (3.4%) is 2.4-times higher than that of bare PbS QD-based planar LSC (G = 11, η_{opt} = 1.4%), even if the concentration of C@S_S QDs is almost 10 times lower (Table 3.2).[95] The η_{opt} of semi-transparent C@S_S QD-based LSC reaches up to 6.1% with G of 10, which is over 15 times higher than that of PbS QD-based planar LSC (G = 4.2) with similar concentration of QDs (~ 20 μM) and represents the highest value ever reported for a planar structure.[89] It has been also demonstrated that η_{opt} can be easily boosted in moderately efficient planar LSC (G = 14, η_{opt} = 3%)[89] simply by shaping the LSC as a hollow cylindrical structure (G = 4.2, η_{opt} = 6.5%),[89] which is, however, impractical for PV applications due to its geometry. A further benefit of C@S_S QD-based LSC compared to bare PbS is that the last ones are dark and nontransparent in the visible range because of their high QD concentrations.[89,95] Also, they are quite short (usually less than 2 cm) due to the strong overlap of absorption and emission spectra in bare QDs. In our case, benefiting from the large Stokes shift in semi-transparent C@S_S QD-based LSC, we are able to fabricate high efficiency large-area LSCs even with low QD concentration. The semi-transparency of LSCs is also an essential requirement for possible application as PV windows in BIPV.

Table 3.2 Optical characterizations of C@S_S QD-based LSCs with different concentrations of QDs and PbS QD-based LSCs.

Samples	Concentration of QDs in LSCs [μM]	LSC side length [cm]	G factor	Quantum efficiency [%]	Optical efficiency [%]
#1_1	14	10	50	4.5	1.1
#1_2	14	8	40	6.6	1.6
#1_3	14	7	35	7.4	1.8
#1_4	14	4	20	11.6	2.8
#1_5	14	2	10	22.3	5.4
#2_1	18	5.5	27.5	7.2	2.2
#2_2	18	4.5	22.5	11.2	3.4
#3_1	24	4.5	22.5	4.1	1.6
#3_2	24	3	15	8.7	3.4
#3_3	24	2	10	15.5	6.1
Planar PbS QD-based LSC[a)]	193	4.5	11	-	1.4
Planar PbS QD-based LSC[b)]	20	-	4.2	-	0.4
Hollow cylindrical PbS QD-based LSC[b)]	100	-	4.2	-	6.5

Error of quantum/optical efficiency: ±10%; [a)] (Reference [95][95]); [b)] (Reference [89][89]).

To further evaluate the optical performance of C@S_S QD-based LSCs, we estimated the LSC quantum efficiency by means of the absorbed optical power, defined as:

$$\eta_{quantum} = \frac{I_{LSC}}{I_{SC}^{Abs} \times G} \quad (3.3)$$

Where I_{SC}^{Abs} is the short circuit photocurrent produced by the Si diode, illuminated by the light absorbed by QDs. The quantum efficiency $\eta_{quantum}$ of C@S_S QD-based LSC (G = 10) is ~22.3%. When the length of LSC is up to 10 cm (G = 50), the $\eta_{quantum}$ keeps around 4.5%. Although this value is lower than that of the reported UV-Vis QD-based LSC, (CdSe/CdS QD-based LSCs achieved $\eta_{quantum}$ ~ 10% with similar G factor[46]) it is quite high for NIR QD-based large-area LSCs. We tested the photostability of our LSCs to prove the resistance of the final device under highly intense UV irradiation. We recorded no significant change in PL peak intensity, position and width after 4-h UV illumination with highly intense UV light {λ=365 nm, 1300 mW/cm^2 (Figure 3.9)}, demonstrating the high chemical-/photo-stability of the QDs integrated in the LSC. This result is highly promising for the practical exploitation of QD-based LSCs. In addition, the quantum/optical efficiency of C@S_S QD-based LSC can be further improved by optimizing the concentration of QDs, increasing the QY, or employing plasmonic nanostructures to enhance PL emission.[113]

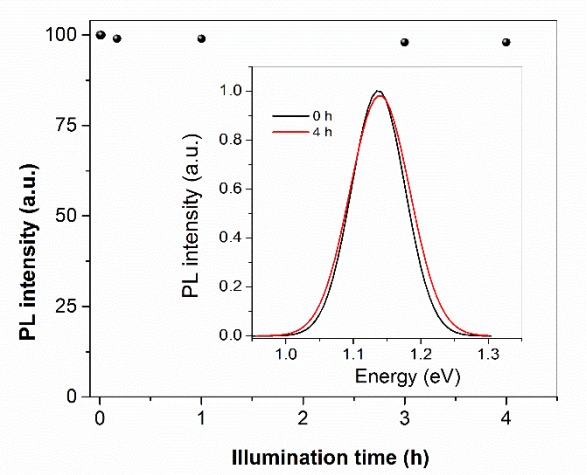

Figure 3.9 Photostability of LSC under UV light illumination (λ=365 nm) at 1300 mW/cm^2. The time was recorded after the QDs were buried into the polymer.

3.3 Summary

In conclusion, I demonstrated engineered Stokes shifts in NIR core/shell PbS/CdS QDs via a cation exchange method, by varying the core size and shell thickness. The as-prepared core/shell QDs show a large Stokes shift with respect to bare QDs, due to the electron leakage from the core to the shell. The resulting LSC based on core/shell QDs embedded in a polymer matrix exhibits excellent optical performance including: (i) broad absorption covering the UV-Vis-NIR range (1.1 ~ 4 eV); (ii) un-changed PL peak position (1.38 eV) and lifetime after incorporation into the polymer matrix; (iii) small PL loss over large areas and (iv) high optical efficiency with respect to bare PbS QDs. Even if the proposed QDs contain Pb and Cd, which are toxic, they are embedded in the polymer matrix, when integrated in LSCs. The semi-transparent C@S_S QD-based LSC shows an external optical efficiency of 6.1% (G = 10). Suppression of emission loss and broad absorption of PbS/CdS QDs offer a favorable approach to be integrated with a PV device in an appropriate spectral region, indicating that it is a promising candidate toward high efficiency semi-transparent large-area LSCs.

Chapter 4 Synthesis and characterization of carbon dots based luminescent solar concentrator

In chapters 2 and 3, we have introduced halide-mixed perovskite $CsPb(Br_xI_{1-x})_3$ QDs and PbS/CdS core/shell QDs for application of large-area LSCs. However, these types of QDs contain heavy metal Pb or Cd which is detrimental to environment. Using heavy metal free or metal-free emitters such as alloyed CuInSeS QDs or carbon dots (C-dots) for LSCs, is an alternative approach to reduce the toxicity and makes LSCs ecofriendly and cost-effective. In this chapter, I investigate the synthesis of "green" metal-free C-dots in different absorption ranges and fabrication of two types of large-area C-dots based LSCs. The optical performance and simulation of optical efficiency are both estimated.

4.1 Synthesis and characterization of carbon dots

As discussed in the aforementioned chapters, besides reabsorption issue, the main challenges that have hampered so far the technological development of LSCs are the following: 1) commonly used inorganic QDs contain toxic elements, e.g. Cd, Pb. Even if CuInSe(S) and silicon QDs are less toxic, the synthesis procedure involves the use of toxic organic solvents;[22,48,114] 2) doped QDs or type-II QDs exhibit reduced reabsorption energy loss which is favorable for large-area LSCs. However, the PL QY of these QDs is typically not very high (<20%) and suffering the low photostability;[112] 3) colloidal inorganic QDs are sensitive to oxygen/moisture/light exposure during synthesis, purification, and post-disposal.

Recent work demonstrated that silicon QDs are very promising emitters for high optical efficiency LSC, as they have almost no energy loss thanks to zero reabsorption, due to the indirect band-gap

of silicon QDs.[22] This type of LSCs exhibit an external optical efficiency of 2.85%. However, the synthesis procedure for silicon QDs is still very complicated, as it requires the use of argon, helium and hydrogen under high pressure (1.4 torr), expensive facilities and extended (12 hour) post-treatment under UV light to improve stability.[22] This challenge may be addressed by using C-dots which represent an emerging class of non-toxic semiconducting nanomaterials.[115-120] C-dots are exclusively composed of heavy metal-free elements (C, N and O) and can be synthesized in large quantities via a simple solvothermal approach using abundant, low-cost precursors.[115,121-125] They also exhibit a relatively high PLQY with tunable absorption up to the near infrared range.[126] For example, Kwon *et al.* synthesized colloidal C-dots with QY as high as 60% using a soft-template approach.[127] Compared to organic dyes/polymers and inorganic QDs, e.g. Si, PbS/CdS and CdSe/CdS, C-dots exhibit excellent air stability, which allows to store them in ambient conditions. In addition, non-radiative emission can be inhibited by surface passivation and functionalization of C-dots, resulting in a large separation between the emission and absorption spectra. This, in turn could reduce the energy loss caused by reabsorption in large-area LSCs.[128,129] Very recently the fabrication of LSCs based on C-dots with small lateral area (4 cm^2) was reported, which shows the potential utilization of C-dots in LSCs fabrication.[130]

4.1.1 Synthesis of carbon quantum dots

In this section, We synthesized OLA modified C-dots and UV C-dots for LSCs applications. For OLA modified C-dots, firstly, hydrophilic C-dots with absorption spectra from UV to longer wavelength up to 700 nm were synthesized via a solvothermal method using citrate and urea as precursor sources. The procedures were described in the following.[126] Typically, 1 g citric acid and 2 g urea were dissolved in 10 mL dimethylformamide under stirring. Subsequently the precursors were transferred into an autoclave and reacted for 6 h at 160 °C. After cooling to room

temperature, the mixture was then added dropwise to 50 mL hexane to precipitate the C-dots. The precipitates were collected and dispersed in 60 mL methanol (original C-dots in methanol). The original C-dots can be surface-modified with Na^+ and OLA for further applications.

For the Na^+ treatment, the original product was mixed with 20 mL NaOH aqueous solution (50 mg/mL), stirred for 1 min. The mixture was then added dropwise to 50 mL hexane to precipitate the C-dots. The precipitates were dispersed in 60 mL methanol. The purified solution was transferred into dialysis bags with a molecular weight of 3000 Da for 2 hours. The C-dots/methanol solution inside the dialysis bag was collected by opening the dialysis bag and pouring the solution into a plastic tube.

In the case of the OLA-modified C-dots, 5 mL as-prepared C-dots in methanol was added to 250 mg EDC and 1 mL OLA. The mixture solution was then stirred for 15 h at room temperature. After the reaction, 20 mL of additional hexane were then fully mixed with the aforementioned solution. The OLA-modified C-dots were transferred into hexane after 5 min standing. For purification of OLA-modified C-dots, the product was kept at -10 °C for 1 h. With low temperature, the residue OLA was precipitated and removed.

For UV C-dots, 1.051 g citric acid and 335 μL ethylenediamine were dissolved in 10 mL water under stirring. Subsequently the precursors were transferred into an autoclave and reacted for 6 h at 200 °C. The as-synthesized reaction solution was transferred into dialysis bags with molecular weight (Mw) of 3000 Da for 2 hours. The C-dots methanol solution outside the dialysis bag was collected and concentrated to 15 mg/L.[131]

4.1.2 Surface modification of carbon dots

For C-dots with absorption spectrum extending in the visible range (denoted as visible C-dots),[126] in the presence of 1-Ethyl-3-(3-dimethylaminopropyl)carbodiimide (EDC) which acts as catalyst and crosslinker, the primary amine from long carbon-chain molecule OLA reacts with the carboxyl group on the surface of C-dots (Figure 4.1a). The OLA modified C-dots exhibit hydrophobic features due to the long carbon-chain. As visible in the pictures displayed in Figures 4.1b,c, the solution of C-dots appears very clear both in methanol and hexane, indicating excellent dispersity before and after phase transfer.

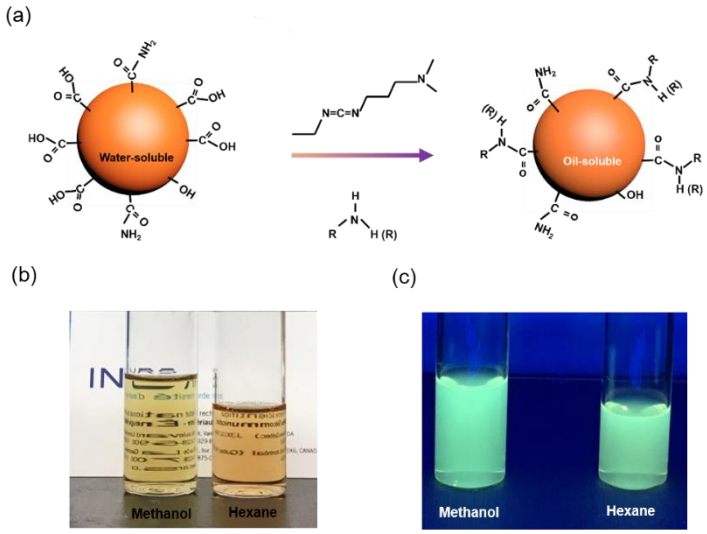

Figure 4.1 (a) Schematic illustration of surface modification of C-dots before and after phase transfer. (b, c) Photographs of visible C-dots in methanol and in hexane under room light (b) and UV light (c).

4.1.3 Structure and optical properties

As shown in Figure 1a, the as-prepared C-dots have diameter sizes in the range ~5-10 nm, consistent with values reported previously.[126] The HRTEM image displayed in the inset of Figure 4.2a identifies a lattice spacing of ~0.333 nm that is well indexed to the (002) plane of graphite,

demonstrating the graphitic sp^2 character of the C-dots, which contribute to strong band edge emission other than lower energy emission from surface traps.[121,126] After surface modification using OLA and further dispersion in hexane, the size and morphologies of C-dots remain unchanged (Figure 4.2b), suggesting a successful phase transfer of C-dots from polar to nonpolar solvent.

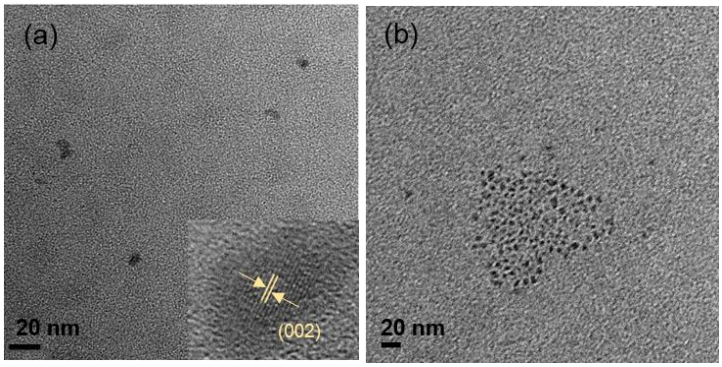

Figure 4.2 TEM and HRTEM images of the freshly synthesized C-dots (a) and the OLA-modified C-dots (b). The inset of (a) is a HRTEM image of C-dots.

The absorption and PL spectra of C-dots before and after different surface treatments are reported in Figure 4.3a. For a fair comparison, all the C-dots were measured under identical conditions e.g. same concentration, optical path and excitation wavelength. The spectrum acquired from freshly synthesized C-dots shows a strong absorption extended over the entire window of visible wavelengths. However, the absorption spectrum strongly overlaps with its broad PL spectrum (500-600 nm) which indicates a large overlap between absorption and emission spectra (Figure 4.3a). Metal-cation-functionalized C-dots (surface treatment with NaOH) can decrease this overlap, resulting in a lower reabsorption (Figure 4.3a). We compared the optical performance under different treatments with NaOH or OLA. After treatment with NaOH, the surface of C-dots can be effectively passivated by Na^+, thereby reducing electron transitions from surface states minimizing the absorption of C-dots in the range of 550-700 nm range (Figure 4.3a).[126] As reported

by Qu et al., the efficiency in Na^+ capped C-dots based light emitting device (LED) exhibits a significant improvement compared to the LED based on the original C-dots due to the efficient metal ion surface passivation and large Stokes shift.[126] The OLA modified C-dots maintain a strong absorption in this range (300-500 nm) and simultaneously exhibit a reduced absorption in the 550-700 nm range (Figure 4.3a).

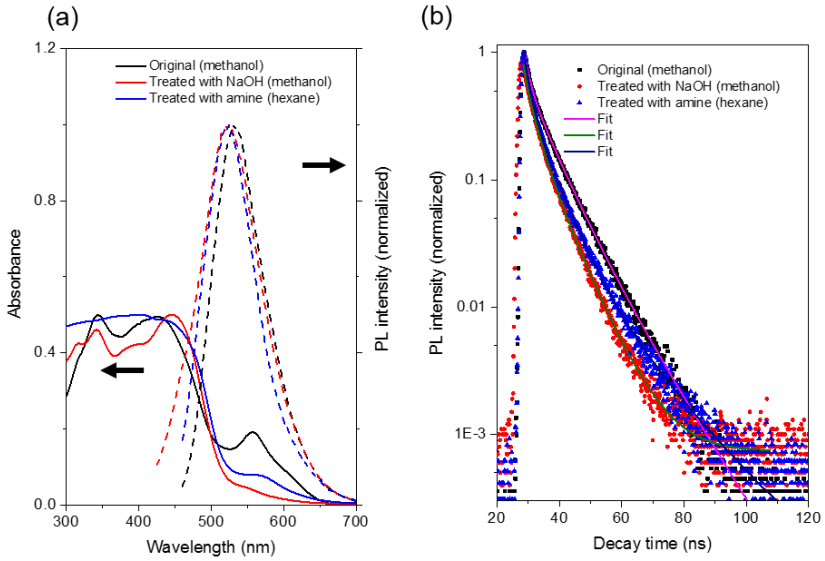

Figure 4.3 (a) Absorption and PL spectra of C-dots under different surface treatments (excitation wavelength at 400 nm) with same concentration in different solvent. (b) PL decay curves collected at emission peak of 540 nm for C-dots under different surface treatments (excitation wavelength at 440 nm).

The C-dots before and after OLA-treatment exhibit an excitation-wavelength dependent PL spectrum (Figure 4.4). With the increase of the excitation wavelength, the PL peak of C-dots exhibits a red-shift. As the absorption spectrum does not change, the red-shift of PL peak leads to a smaller overlap of the absorption and emission spectra, which is promising for their applications in LEDs[126] and LSCs. After phase transfer, the C-dots still exhibit bright emission under UV illumination (Figure 4.1c). The reduced re-absorption and oil-soluble property of the OLA modified C-dots are promising for LSC fabrication. The QY of the Na^+ modified C-dots is around 40%, higher than that of freshly prepared C-dots (~30%) and of OLA-modified C-dots (~20-

30%).[126] The OLA-modified C-dots exhibit a similar PL emission peak as that of a freshly prepared sample (Figure 4.5). Considering that the modification process is carried out under ambient conditions without any protection, C-dots present a better chemical/structural stability compared to other types of inorganic QDs.[46,48,51,62,77]

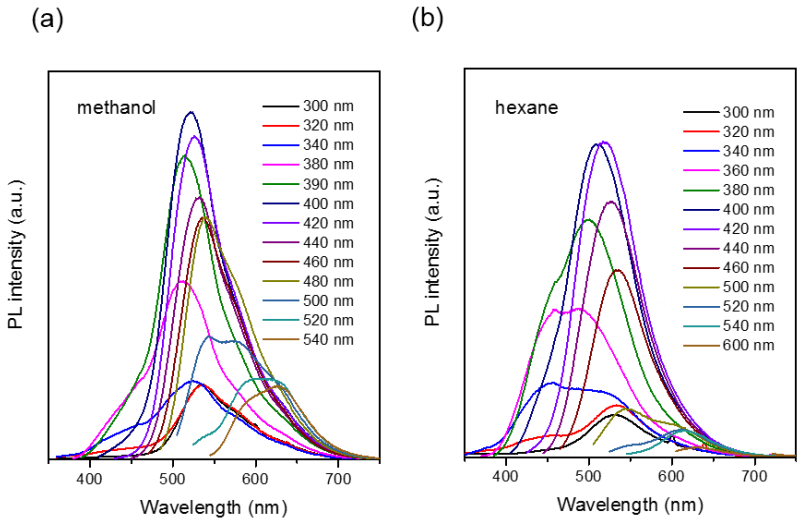

Figure 4.4 PL spectra of (a) the freshly prepared C-dots in methanol and (b) the OLA-modified C-dots in hexane at different excitation wavelengths.

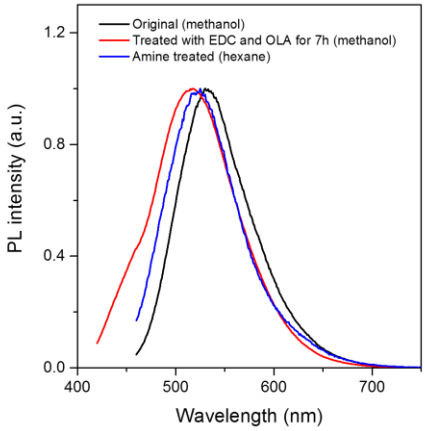

Figure 4.5 PL spectra of the C-dots under different conditions. Excitation wavelength is 440 nm.

PL decay curves of C-dots with different treatments were also studied, as shown in Figure 4.3b. Due to the well passivated surface treatment, the PL lifetime of Na^+ modified C-dots is ~7.1±1 ns, in the same range with the reported value for high-efficiency Na^+ C-dots (~4 ns).[126] The PL lifetime of the original and OLA-modified C-dots is around 8.6±1 ns, which is longer than that of NaOH treated C-dots, consistent with the literature and their QYs.[126]

4.2 Fabrication and optical measurement of carbon dots based luminescent solar concentrators

In this section, I used OLA-modified C-dots for planar LSCs application. Additionally, UV active C-dots and OLA-modified C-dots were used for thin-film LSCs fabrication. Their optical performance is estimated by using calibrated Si solar cell as reference and power meter, respectively. To validate our measurements and explore the possibility to realize large-area LSCs with C-dots exhibiting higher QY, the analytical model of planar LSCs reported previously is implemented.[46]

4.2.1 Fabrication and characterizations of carbon dots based luminescent solar concentrators

First, we focus on fabricating large-area LSCs by incorporating hydrophobic OLA-modified C-dots in the crosslinked PLMA polymer matrix. Details on LSC fabrication are the same as the fabrication presented in chapter 2. After polymerization with a UV initiator, C-dots were embedded into a crosslinked PLMA polymer matrix with typical dimension of 0.2 × 1.5 × 10 cm^3.[62] The absorption and PL spectra of the C-dots in the PLMA polymer matrix are almost identical to those of the C-dots in hexane solution (Figures 4.3a, 4.6c). The working principle for C-dot based LSCs in polymer matrix is illustrated in Figure 4.6a.

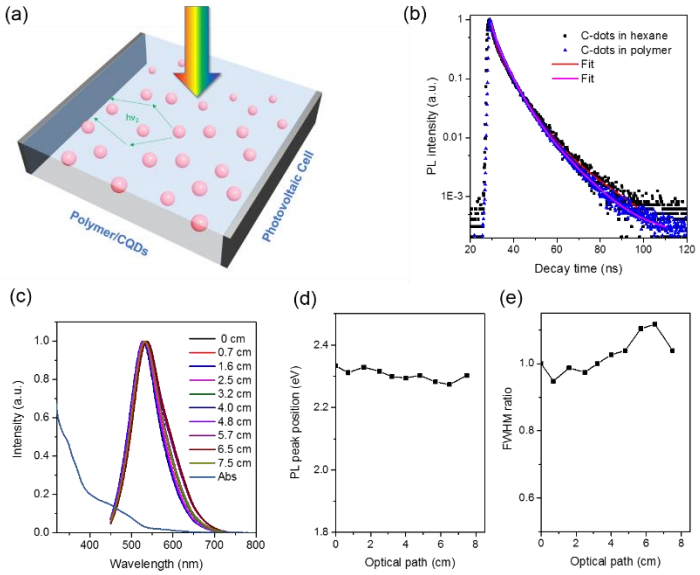

Figure 4.6 (a) Schematic demonstration of C-dot based LSCs integrated with PV device. (b) PL decay curves collected at emission peak of 540 nm for the OLA-modified C-dots in hexane and polymer matrix (excitation at 440 nm). (c) Absorption and PL spectra measured at different optical paths for the OLA-modified C-dot based LSCs. (d, e) PL peak position (d) and PL FWHM ratio (e) of the OLA-modified C-dot based LSCs as a function of optical path.

The absence of additional non-radiative decay channels in the C-dots/polymer was confirmed by PL decay measurements, which showed identical dynamics for the C-dots in hexane and after encapsulation in the polymer (Figure 4.6b). We further measured the PL spectra of C-dot based LSCs as a function of the optical path (Figure 4.6c). Specifically, the PL signals from the LSC are recorded at a certain distance between the edge and vertically illuminated spot at an excitation wavelength of 440 nm, which characterizes the reabsorption effect on LSCs. As shown in Figure 4.6c, the overlap between absorption and emission spectra is very small. By increasing the optical path, the PL spectra exhibit a limited red-shift. Following the approach introduced by Meinardi et al[48], we normalized the PL spectra of LSCs as a function of optical paths. The PL peak position and shape can only affected by the light reabsorption due to either polymer matrix or C-dots. The PL peak position is almost unchanged, remaining close to 2.3 eV (~540 nm) due to the efficient separation between the absorption and emission spectra,[46,48] indicating that the OLA modified C-

dots based LSC exhibits excellent optical properties (Figure 4.6d). Only a slight PL peak tail was observed for long optical paths (> 5 cm), leading to a broadening of the FWHM which is due to reabsorption (Figure 4.6e).

To demonstrate the suitability of C-dots as emitters in LSCs, I further fabricated LSCs based on a thin-film tandem system by incorporating hydrophilic C-dots (15 mg/mL) in the PVP (200 mg/mL) and spin-coating them on the glass substrate (scheme in Figure 4.7a). Compared to the above mentioned QDs/PLMA polymer based LSCs which has thickness of 2 mm, the thickness of C-dots/PVP layer on a glass substrate is only 50-100 μm. The emitted photons travel within the glass, decreasing the probability of meeting C-dots, leading to reduced energy loss due to the reabsorption. In addition, only NaOH post-surface treatment is needed as visible C-dots can be effectively dispersed in PVP/methanol or PVP/water. Last but not least, the fabrication technique used for realizing large-area LSCs is very simple, as it does not use any organic solvent and UV illumination. Two types of C-dots were used to fabricate the LSCs. The first layer of LSCs was fabricated using UV C-dots (denoted as #1)[131] (QY of 60%) without any of post-surface-treatment. The visible NaOH modified C-dots (denoted as #2) with a QY of 40% and the original C-dots without any surface treatment (QY of ~30%) were used to fabricate the second layer of thin-film LSCs (Figure 4.7).

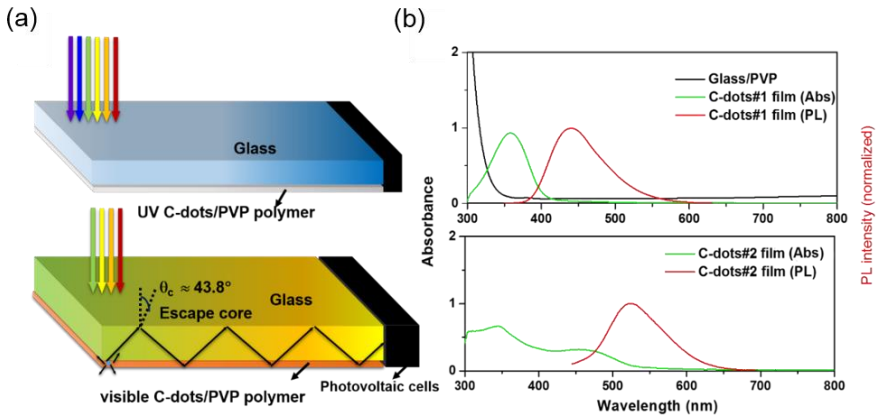

Figure 4.7 (a) Schemes of tandem thin-film LSCs based on UV C-dots (top) and visible C-dots (bottom). (b) The absorption and emission spectra of UV C-dots (#1, top) and visible NaOH treated C-dots (#2, bottom) based thin-film LSCs and absorption spectrum of PVP on a glass substrate.

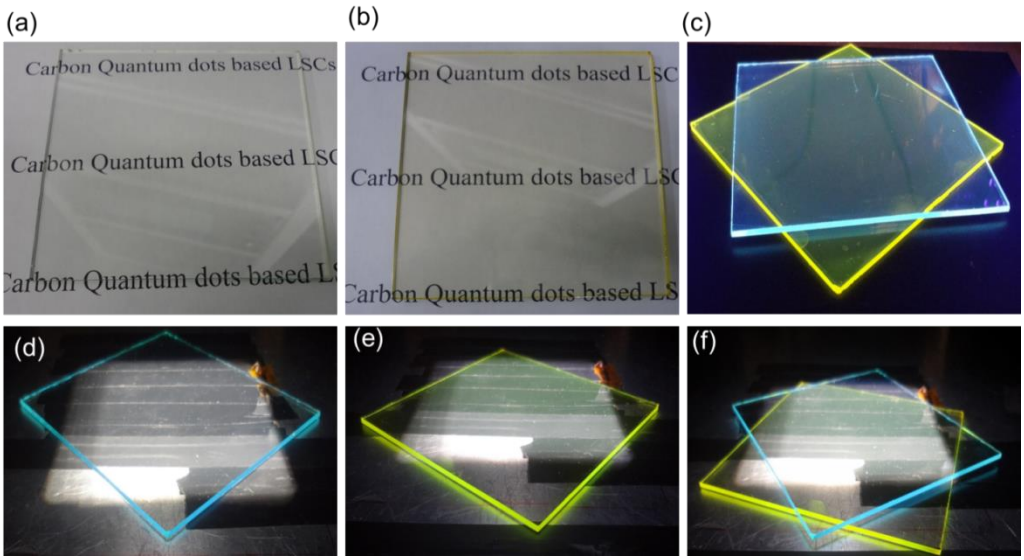

Figure 4.8 (a, b) Photographs of thin-film LSCs based on C-dots#1 (a) and C-dots#2 (b) under ambient light. (c-f) Photographs of tandem thin-film LSCs based C-dots LSCs under UV illumination (c) and one sun AM 1.5G illumination (f), and thin-film LSCs based on C-dots#1 (d) and C-dots#2 (e) under one sun AM 1.5G illumination. The dimensional size of LSCs is 10×10 cm^2.

As shown in Figure 4.7b, UV C-dots exhibit very large separation of absorption and emission spectra and a high QY of 60%, which reduces the reabsorption loss. In addition, the emitted visible light in the first layer escaped by the waveguide, could be further absorbed by the second layer of NaOH treated C-dots, concentrating from the edges of the glass substrate. By using UV active and

visible NaOH modified C-dots, I fabricated semitransparent tandem thin-film LSCs, shown under different illuminations (Figure 4.8). Thin-film C-dots based LSCs exhibit very good transparency in visible range, which is favorable for the use of solar smart windows (Figures 4.8a, b). The PL peak position for both types of C-dots exhibits a slight red-shift due to the reabsorption energy loss (Figure 4.9).

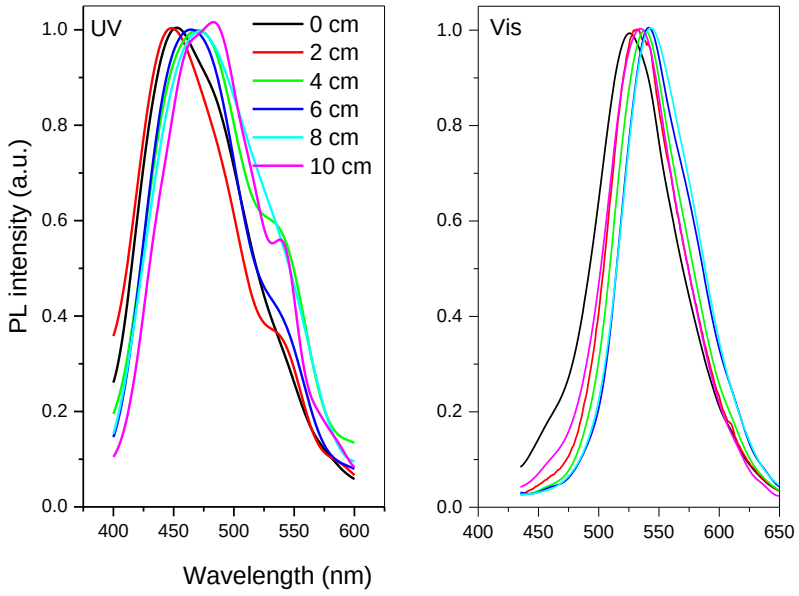

Figure 4.9 Normalized PL spectra measured at different optical paths for the thin-film LSCs based on UV and visible C-dots.

4.2.2 Optical performance measurement and simulation of carbon dots based luminescent solar concentrators

As shown in Figure 4.10a, the square large-area LSC (10 × 10 cm^2) appears highly transparent in ambient environment, and a concentrated yellow light is clearly visible under low-intensity illumination (0.3 Sun, 30 mW/cm^2), indicating the promising potential to be used to power buildings even when the light intensity is reduced, *e.g.* like when the sky is overcast. When the top surface of the LSC is partially placed under one sun illumination, the concentrated yellow light

emitting from the edges is clearly visible in Figure 4.10b. The optical performance of the polymer based LSCs with different concentrations (absorption spectra of C-dots are shown in 4.11, which were used to define the concentration of C-dots in PLMA) of C-dots (dimension: 0.2 × 1.5 × 10 cm^3), are shown in Figures 4.10c-f.

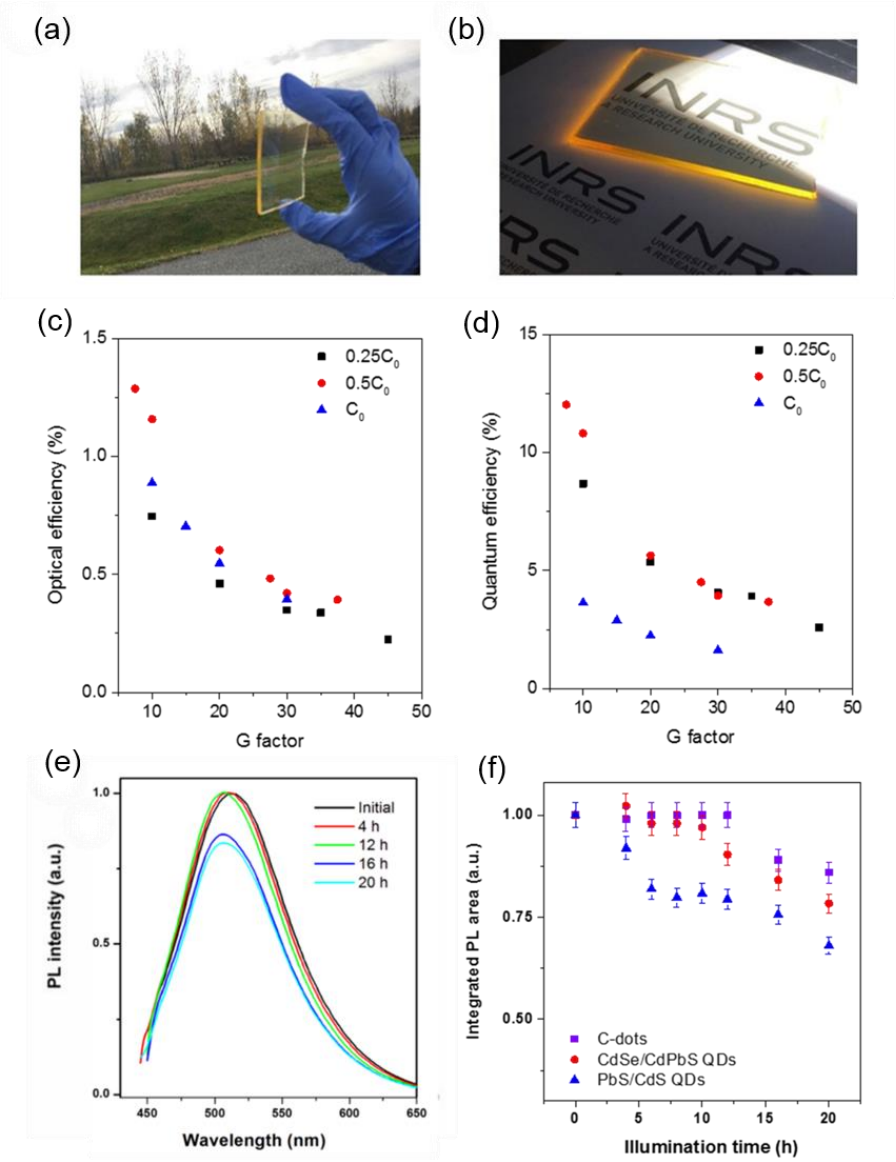

Figure 4.10 (a, b) Photographs of colorless large-area OLA-modified C-dot based LSCs with dimension of 0.2 × 10 × 10 cm^3 under ambient (a) and UV illumination (b). (c, d) External optical efficiency (c) and internal quantum efficiency (d) of LSCs with different concentration of the OLA-modified C-dots. (e, f) PL spectra of C-dots based LSC (e) and PL intensity of different types of QDs based LSCs (f) upon UV exposure (1.3 W/cm^2) for several hours.

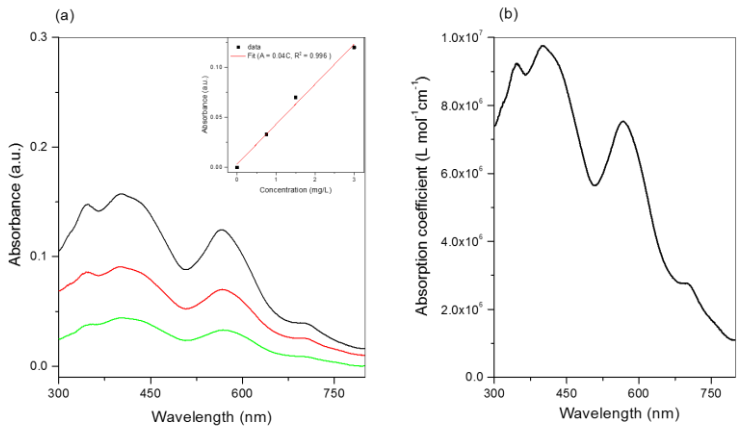

Figure 4.11 (a) Absorption spectra of OLA-modified C-dots in methanol solution with different concentrations (C_0, 0.5 C_0 and 0.25 C_0). Inset is the Beer's law relationship between absorbance at 564 nm and concentration of C-dots. The concentration is defined as C_0 = 2.8 mg/L when A = 0.12 @ 564 nm. (b) Absorption coefficient spectrum of OLA-modified C-dots in methanol solution. The C-dots show a similar absorption coefficient to that of inorganic QD.[132]

To calculate the external optical efficiency of the LSCs, we coupled a commercial Si solar cell on one edge of the OLA-modified C-dot based LSCs (details described in the chapter 2).

As expected, η_{opt} drops exponentially with the increase of the G factor of the LSCs (Figures 4.10c, d) consistent with the decrease of integrated PL area with the increase of optical paths (Figure 4.12) which could be due to the combined effect of light escaping from the waveguide and reabsorption by the C-dots and the polymer matrix. A maximum external optical efficiency of $\eta_{opt} = 1.2\%$ is achieved with G factor of 10 (1.5×2 cm^2, three edges coupled with optical mirrors) at a concentration of 0.5 C_0 (C_0 equals to 2.8 mg L^{-1}) (Figure 4.10c). Increasing the G factor up to 38 (corresponding to a LSC length of 7.6 cm), η_{opt} decreased to ~0.4% due to reabsorption and scattering loss.

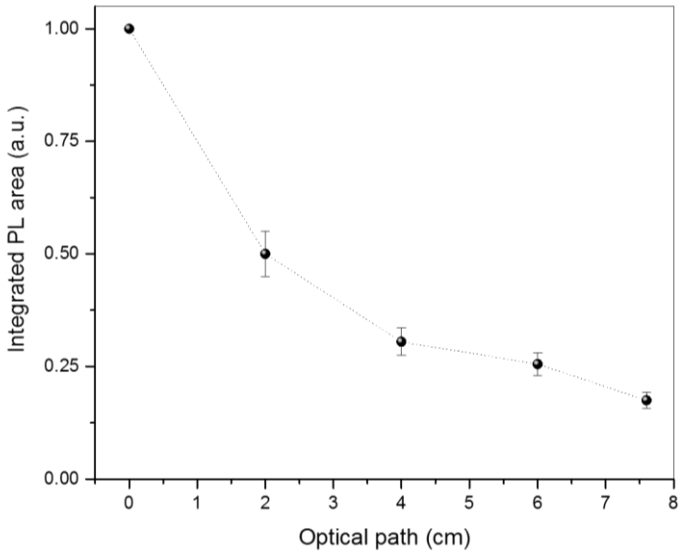

Figure 4.12 Integrated PL area of the OLA-modified C-dot based LSCs as a function of optical path. The PL spectra are taken from Figure 4.6c.

We further estimate the quantum efficiency η_{quantum} of LSCs. In this case, the highest η_{quantum} is achieved by the LSC with the lowest concentration (0.25 C_0) of C-dots, with a value of ~13%, slightly lower than the QY of the C-dots in hexane. This indirectly confirms that the PL emission of embedded C-dots in the polymer matrix does not change The highest value obtained for 0.25 C_0 can be due to the smallest absorption at this concentration in the emission range of the C-dots which limits the energy loss due to re-absorption.[129] Even at a large G factor (G=38), η_{quantum} is still around 4%. This value is similar to that of LSCs made of PbS/CdS core/shell QDs (4.5%, G = 50).[62] Comparing η_{quantum} of the C-dot based LSCs with the best inorganic QDs based LSC, we observe that the internal quantum efficiency obtained using CdSe/CdS core/shell QDs with a QY of 45% (measured under the same conditions, under one sun and the same distance from the sun simulator to the LSCs) is around 10% at G = 40.[46] With a higher QY of ~70% for the same type of CdSe/CdZnS core/shell QDs, the maximum internal quantum efficiency increases to 15% at G=32.[50] Using $CuInSe_xS_{2-x}$/ZnS core/shell QDs, η_{quantum} is ~16.7%.[48] Considering the much

lower QY (~ 20-30%) in C-dots compared to the reported value for inorganic QDs, the reported quantum efficiency is comparable to those of semi-transparent highly efficient inorganic QD based LSCs (Table 4.1).

Table 4.1 Optical performance of QDs based LSCs.

Sample (QDs)	QY (%)	Lateral area (cm^2)	G factor	Optical efficiency (%)
C-dots (polymer based)	30	1.5×8	38	0.4
PbS/CdS	40	1.5×10	50	1.1
CdSe/CdS	45	1.3×21.5	40	1
CdSe/CdZnS	70	20×20	32	0.9
$CuInSe_xS_{2-x}$/ZnS	40	12×12	40	2.85

We further examined the stability of LSCs based on various types of QDs including PbS/CdS core/shell QDs,[62] CdSe/CdPbS core/thick-shell QDs[51] and C-dots under indentical measurement conditions (a high dose of UV illumination, 1.3 W/cm^2, equal to 260 sun illumination;[50] humidity of ~ 40% at room temperature). After four hours, the PL peak position and PL intensity of the as-fabricated LSCs based on C-dots and CdSe/CdPbS core/thick-shell QDs do not show a significant change compared to the LSC before illumination (Figures 4.10e,f). Similarly, the PL lifetime of C-dots in polymer matrix exhibit equivalent values of 7.2±1 ns and 8.6±1 ns after and before 4h UV exposure, respectively (Figure 4.13). When increasing the illumination time (12 hours), the PL intensity of LSCs based on C-dots still does not change, indicating the LSCs based on C-dots

are very photo-stable.[50] While further UV illumination (12 hours) leads to a decrease in PL intensity of the LSCs based inorganic QDs (such as 20% drop in PbS/CdS QDs and 10% drop CdSe/CdPbS QDs) (Figure 4.10f and Figure 4.14). In addition, there is no significant change regarding the color and external optical efficiency of the LSCs based on C-dots after storing at ambient conditions for more than four months. These results indicate that C-dots QDs based LSCs are very promising for long-term stable LSCs application compared to inorganic QDs based LSCs.

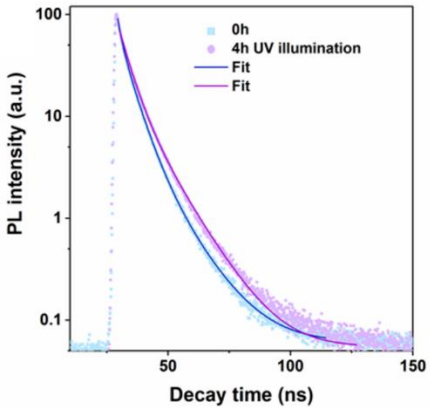

Figure 4.13 PL decay curves collected at 540 nm wavelength of the OLA-modified C-dot based LSCs (G = 10) without or with UV exposure (1.3 W/cm^2) for four hours.

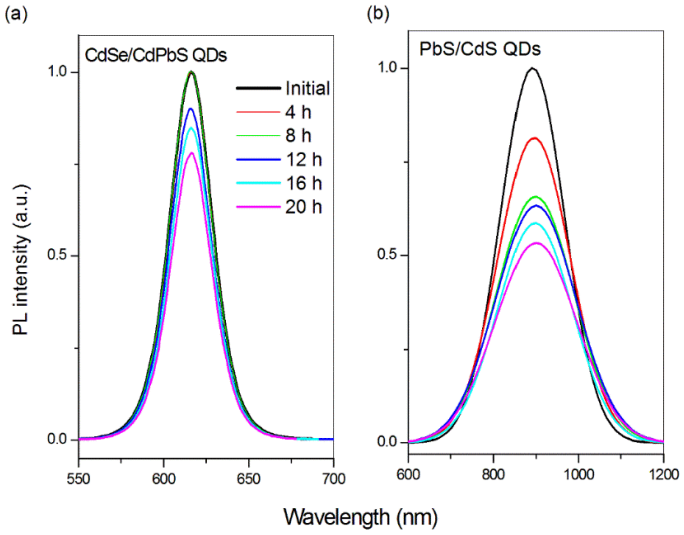

Figure 4.14 Stability of the QD-polymer composites. PL spectra of CdSe/CdPbS core/thick-shell QDs (a) and PbS/CdS core/shell QDs (b) based LSCs upon UV exposure (1.3 W/cm^2) for several hours.

To validate our measurements and explore the possibility to realize large-area LSCs with C-dots exhibiting higher QY, we implemented the analytical model of planar LSCs reported previously[46] (details for simulation are included in chapter 2). We can accurately fit the results of the η_{opt} and internal quantum efficiency as reported in Figure 4.15b, d. In addition, we can simulate the effect of increasing the QY of the C-dots (Table 4.2): with a PLQY value of 75% the maximum optical efficiency, at G=10, would be around 2% and for G=40 it would be 1%. An ideal C-dot, with PLQY of 1, would have a maximum efficiency of ~3.5% at G=10.

Table 4.2 External optical efficiency of 0.5 C_0 C-dot based LSC for different values of the QY.

QY (%)	G	External optical efficiency (%)
75	10	2.5
75	40	1.5
100	10	3.5

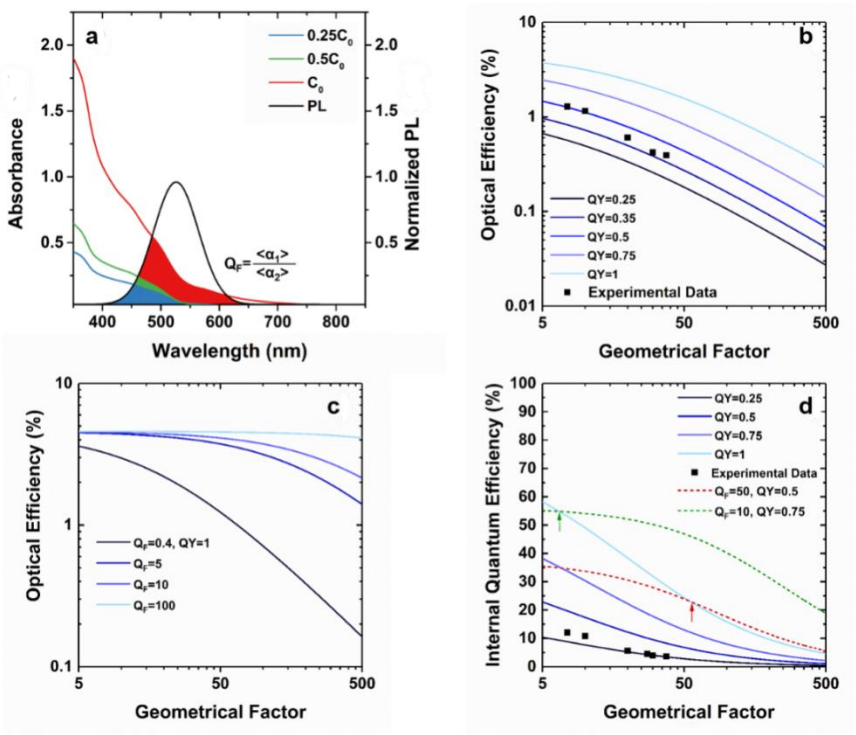

Figure 4.15 Analytical model of the performance of OLA-modified C-dot based LSC with 0.5 C_0. (a) Overlap between absorption and emission of the C-dots at different concentrations. (b) External optical efficiency of 0.5 C_0 C-dot based LSC with the PLQY varied from 0.25 to 1. The square points are the experimental data obtained with the electro-optical method of comparing the J_{sc}. (c) External optical efficiency of 0.5 C_0 C-dot based LSC with PLQY=1 when varied the quality factor from 0.4 (the value measured) up to 100 (d) Internal quantum efficiency of 0.5 C_0 LSCs with different PLQY. The dotted lines are calculated for C-dots with PLQY=0.5 and Q_F =50 (red dotted line), PLQY=0.75 and Q_F =10 (green dashed line). The square points are the experimental data obtained with the method of comparing the different I_{sc}.

Another way to increase the performance of the LSC is to increase the quality factor (Q_F) defined as the ratio between the absorption coefficient (α_1) at the wavelength λ_1 of collected light and the absorption coefficient (α_2) at the emission peak (Figure 4.15a), as demonstrated in Chapter 2.

Figure 4.15c reports simulation results of the effect of increasing Q_F (and therefore the Stokes-shift) of the C-dots with QY=1 on the optical efficiency. The main consequence is an increase of the efficiency for large-area LSCs: with a Q_F of 10, the maximum efficiency at G=500 would be more than 2%. Considering the large G of 500, an efficiency of 2% in LSC leads to at least 10-fold decrease of solar cell area with similar power generation. Observing the internal quantum

efficiency. Observing the internal quantum efficiency (Figure 4.15d), the C-dots based LSC would have the same performance of the inorganic QD based LSCs, with η_{quantum} of ~15% at G=50 when the QY of the C-dots is 75%.

It is also possible to reduce the effect of a low QY by an increase in the Q_F. For example, with a PLQY=75% and Q_F=10 we can achieve higher efficiency than the case of C-dots with an ideal PLQY=100% but lower Q_F. A similar performance of LSCs could be achieved by using C-dots (G=50) with either a PLQY of 50% (Q_F=50) or a PLQY of 100% (Q_F=0.4). This simulation indicates that we can tune both the PLQY and the Q_F by tuning the concentration of C-dots and the overlap of absorption and emission spectra to obtain high-efficiency C-dot based LSCs.

The optical performance of thin-film LSCs under solar radiation (100 mW/cm^2) was directly measured by an optical power meter. Single layer LSCs have an efficiency of 0.4% and 0.9% respectively for UV C-dots based LSC and visible NaOH-treated C-dots based LSC, while the tandem thin-film LSC exhibits a high optical efficiency of 1.1% with dimension of 10×10×0.2 cm^3 due to the reduced scattering and reabsorption (values reported in Table 4.3). The external optical efficiency is comparable with LSCs based on PLMA polymer (1.3%, G of 10), but with a larger surface area (100 cm^2 vs 3 cm^2). To the best of our knowledge, only one group used silica coated inorganic QDs making the thin-film LSCs.[50] However, in their case, the hydrophobic Cd-based QDs need to be coated with a silica layer and then dispersed in PVP matrix which is time-consuming and very expensive. In view of the simple preparation procedure and good optical performance, C-dots pave the way towards LSCs with high efficiency and excellent stability.

Table 4.3 External optical efficiency of thin film C-dots based LSCs with lateral area (10×10 cm^2). #1: UV C-dots; #2: visible NaOH treated C-dots.

LSCs		External Optical Efficiency (%)	
C-dots#1		0.4	
C-dots#2_Original		0.7	
C-dots#2		0.9	
Tandem LSCs	C-dots#1	0.4	1.1
	C-dots#2	0.7	

4.3 Summary

I demonstrated low-cost, large-area and high-efficiency LSCs based on metal-free, colloidal C-dots dispersed in a PLMA polymer matrix or PVP on glass substrate. With proper surface modification, the as-synthesized C-dots show a reduced absorption/PL spectral overlap. The OLA-modified C-dots exhibit a PLQY of ~30% and an excellent photo-/chemical stability without any emission loss during the entire process of their encapsulation into a polymer matrix. Due to their broad absorption and relatively low reabsorption loss, large-area C-dot based LSCs exhibit an η_{opt} of 1.2% (G = 10) and η_{quantum} of 4% (G = 38), comparable to those of semi-transparent highly efficient inorganic QD based LSCs. The tandem semi-transparent thin film LSCs (100 cm^2) exhibit an external optical efficiency of 1.1%. The LSCs are highly stable in air and do not exhibit any noticeable variation in PL under UV light illumination (1.3W/cm^2) for over twelve hours. The external optical efficiency of LSCs can be further enhanced by improving the absorption range,

enhancing the PLQY and increasing the quality factor by modifying the surface of C-dots. The cost of C-dot based LSCs would be cheaper compared to LSCs made of inorganic QDs, considering the easier synthesis using abundant and low-cost carbon elements and their simple disposal after use. In view of the simple synthesis procedure, easy surface modification, environmental friendliness, non-toxicity, low-cost and excellent optical properties of C-dots compared to conventional inorganic QDs and dyes/polymers, they may represent a practical emitter for large-area, high efficiency LSCs, which are promising for renewable and clean solar energy applications such as transparent solar windows.

Chapter 5 Synthesis and characterization of $PbSe_{1-x}S_x$ nanoplatelets based photoanode for solar-driven hydrogen generation

In this chapter, I focus on the synthesis of 2D alloyed NIR $PbSe_{1-x}S_x$ NPLs via cation exchange process of ultrathin $CdSe_{1-x}S_x$ NPLs. The prepared ultra-small alloyed NIR $PbSe_{1-x}S_x$ NPLs exhibit broad absorption, large absorption coefficient and high QY, compared to metal oxides. The NIR NPLs with high carrier mobilities and perfect spectral match to solar irradiation region is favorable to be applied in solar technologies. As a proof of concept, we further discussed the photoelectrochemical performance of NIR NPLs based photoanodes in solar-driven hydrogen generation.

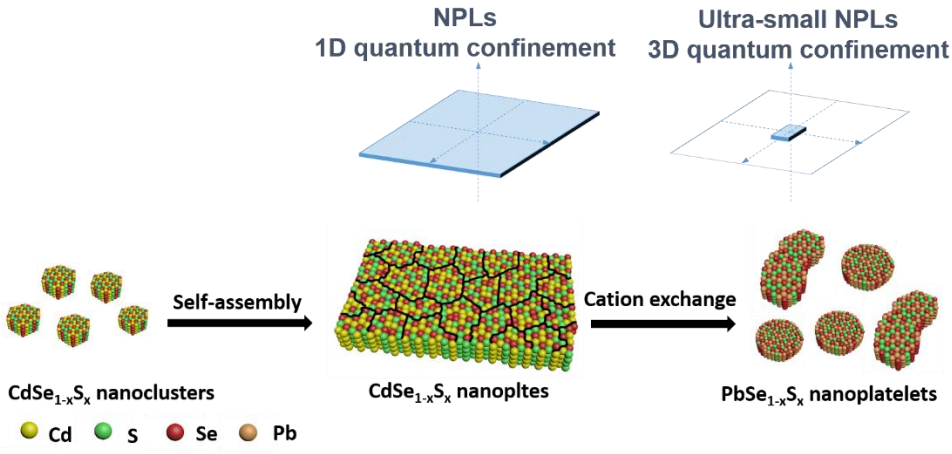

Figure 5.1 Scheme of the formation of NIR NPLs through cation exchange using visible NPLs as template and 1D to 3D transition of quantum confinement from NPLs to ultra-small NPLs.

5.1 Synthesis and characterization of $PbSe_{1-x}S_x$ nanoplatelets

Ultrathin 2D nanomaterials are sheet-like structures with single- or few-layer thickness (typically less than 5 nm), with lateral size ranging from 100 nm to tens of micrometers. They exhibit

ultrahigh specific surface area and strong quantum confinement in one dimension, leading to unusual and promising physical, optical, chemical and electronic properties,[133-135] such as relatively large absorption coefficient, high carrier mobility and unique thickness-dependent optical transitions.[136-139] Charge carriers in 2D structures e.g. nanosheets, are confined by finite thickness but can move freely in a plane, which may lead to superior charge transport compared to assemblies of quantum dots (QDs, zero-dimensional).[134] In addition, the carrier multiplication efficiency in 2D PbS nanosheets is higher than that in PbS QDs.[140,141] These 2D systems represent one of the latest frontiers in nanomaterials, and may be used as building blocks in several high-performance optoelectronic devices such as LED, FETs, photovoltaics, photocatalysis and energy storage.[142-145] Because of the strong quantum confinement in 2D NPLs, the narrow PL emission can be tuned by precisely controlling their thickness at the nanoscale.[146-148] Colloidal 2D NPLs can be synthesized using different methodologies, including soft templates, self-organization and oriented attachment.[149] Recently, the cation exchange approach has also been used to synthesize high-quality NPLs by replacing the cations within the nanocrystal lattice with a different metal ion.[133,150] In general, the pre-synthesized NPLs with well-defined size and structure can be used as a template for the synthesis of compositionally bare, alloyed and core/shell nanostructures.[151] For example, PbS/CdS core/shell nanosheets have been synthesized.[133,150] The presence of the CdS shell can increase the QY from 6% in bare PbS nanosheets to 11% in PbS/CdS nanosheets, thanks to surface passivation.[150]

NPLs exhibit a series of outstanding optoelectronic properties for various applications in energy technologies, such as solar cells or solar-driven hydrogen production, because of their suitable electronic band structure for fast exciton dissociation, efficient charge transfer of photogenerated electron/hole pairs, and high photochemical stability.[152,153] NIR NPLs based on lead or tin

chalcogenides enable a thickness-tunable wide absorption spectrum, ranging from UV to NIR, thereby matching the solar spectrum with significant overlap.[133-135,150] However, due to the larger size of 2D NPLs with respect to QDs, and the lack of reliable synthesis methodologies for producing ultra-small-sized NPLs (less than 10 nm in lateral size), bandgaps obtained up to now (< 0.9 eV) are not favorable for use in PEC H_2 generation.

In this chapter, we developed a cation-exchange route to synthesize ultra-small ternary NPLs optically active in the NIR. The NPLs (PbSe or alloyed $PbSe_{1-x}S_x$) with lateral dimensions below 10 nm exhibit continuously tunable PL emission ranging from 1180 to 1380 nm thanks to the variation of the S/Se ratio, with QYs up to ~60%. Theoretical simulations of the bandgap as a function of thickness, geometry and size show that ultra-small NPLs exhibit strong 3D quantum confinement, compared to 1D confinement in larger sized NPLs with similar thickness. In addition, the NPLs serves as photosensitizers for PEC hydrogen generation. After surface treatment with Cd, we obtained a saturated photocurrent density of ~5 mA/cm^2, nearly three times higher than the value obtained from PbS/CdS QDs under identical preparation and measurement conditions.[154]

5.1.1 Synthesis of $CdSe_{1-x}S_x$ nanoplatelets

Ultrathin $CdSe_{1-x}S_x$ NPLs with different ratios of Se/S is synthesized by following the protocol reported in the literature.[146] (a) $CdSe_{1-x}S_x$ NPLs (Se:S=1:0): 960 mg of $Cd(CH_3CO_2)_2•2H_2O$, 90 mL of ODE, and 2.6 mL of OA were introduced into a reaction flask and pumped under vacuum at 110 ^oC for 90 min. 156 mg of Se powder was measured and injected into the reaction flask as a dispersion in 4 mL of ODE at 110 ^oC. After switching to a nitrogen environment, the temperature was increased to 240 °C. As the temperature rose, at 205 °C, 480 mg of $Cd(CH_3CO_2)_2•2H_2O$ was added to the flask. The reaction was allowed to proceed for 15 min at 240 °C and was then cooled to room temperature to extract the product. During the cooling process, 5 mL of OA and 15 mL of

toluene was injected. Once the product reached room temperature, it was washed by centrifugation at 3000 rpm for 20 min and final precipitate was dispersed in 10 mL of hexane.

(b) $CdSe_{1-x}S_x$ NPLs (Se:S=3:1): 960 mg of $Cd(CH_3CO_2)_2 \bullet 2H_2O$, 90 mL of ODE, and 2.6 mL of OA were introduced into a reaction flask and pumped under vacuum at 110 °C for 90 min. 120 mg of Se and 16 mg of S powder was measured and injected into the reaction flask as a dispersion in 4 mL of ODE at 110 ^oC. After switching to a nitrogen environment, the temperature was increased to 240 °C. As the temperature rose, at 205 ^oC, 240 mg of $Cd(CH_3CO_2)_2 \bullet 2H_2O$ was added to the flask. The reaction was allowed to proceed for 60 min at 240 ^oC and was then cooled to room temperature to extract the product. During the cooling process, 5 mL of OA and 15 mL of toluene were injected. Once the product reached room temperature, it was washed by centrifugation. The product was split in three parts and centrifuged at 3000 rpm for 20 min, and final precipitate was dispersed in 10 mL of hexane.

(c) $CdSe_{1-x}S_x$ NPLs (Se:S=1:1): 960 mg of $Cd(CH_3CO_2)_2 \bullet 2H_2O$, 90 mL of ODE, and 2.6 mL of OA were introduced into a reaction flask and pumped under vacuum at 110 ^oC for 90 min. 117 mg of Se and 48 mg of S powder were measured and injected into the reaction flask as a dispersion in 4 mL of ODE at 110 ^oC. After switching to a nitrogen environment, the temperature was increased to 240 °C. As the temperature rose, at 193 °C, 720 mg of $Cd(CH_3CO_2)_2 \bullet 2H_2O$ was added to the flask. The reaction was allowed to proceed for 10 or 15 min at 240 ^oC and was then cooled to room temperature to extract the product. During the cooling process, 5 mL of OA and 12 mL of 1:1 toluene-hexane mixture was injected. Once the product reached room temperature, it was washed by centrifugation at 3000 rpm for 20 min and final precipitate was dispersed in 10 mL of hexane.

5.1.1.1 Effect of reaction molar ratio

Colloidal $CdSe_{1-x}S_x$ NPLs were formed[146] via nucleation of $CdSe_{1-x}S_x$ nanocrystals, followed by the lateral extension of seeds induced by an acetate leading to NPLs.[149] Typical $CdSe_{1-x}S_x$ NPLs have large lateral dimensions (60×40 nm^2) and thickness of ~2 nm, corresponding to ~5-6 monolayers (MLs) (Figure 5.2), which is consistent with values found in the literature.[146] The X-ray Diffraction (XRD) patterns exhibit features of zinc blende structure from both CdSe and CdS without splitting, confirming the zinc blende phase of the samples (Figure 5.3). Combined XRD and TEM analysis confirms that the lattice parameters of the $CdSe_{1-x}S_x$ NPLs fall between CdS and CdSe. We also found that it decreases with increasing S concentration, due to the smaller atomic radius of S compared to Se. The alloyed composition and Se/S ratio in $CdSe_{1-x}S_x$ NPLs with feeding ratios of Se/S equal to 1:1 and 3:1 are also confirmed and estimated as 1:1 and 2:1 from EDS data in Figure 5.4.[146] The d spacing of $CdSe_{1-x}S_x$ NPLs based on the high resolution TEM (HR-TEM) image is 0.345 nm; it corresponds to the {111} planes, indicating the lateral growth direction of $CdSe_{1-x}S_x$ NPLs.

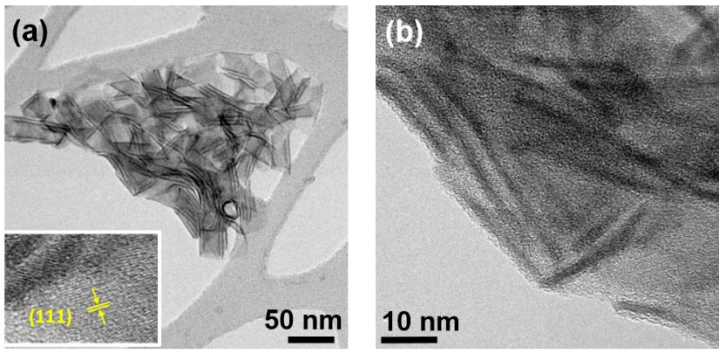

Figure 5.2 TEM Bright-field Images (BFI) of $CdSe_{1-x}S_x$ NPLs (Se:S = 3:1).

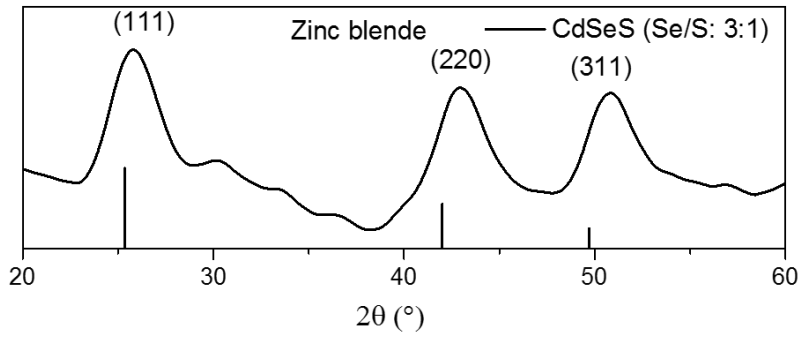

Figure 5.3 XRD spectrum of $CdSe_{1-x}S_x$ NPLs (Se:S = 3:1).

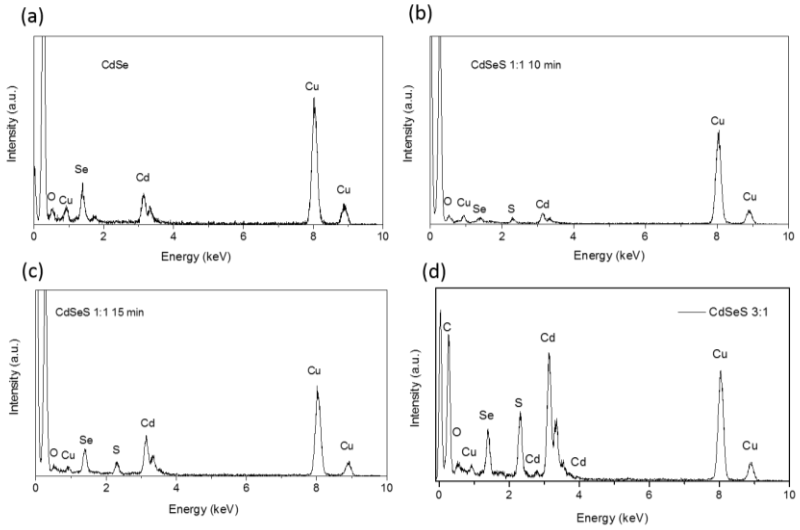

Figure 5.4 EDS spectra of $CdSe_{1-x}S_x$ NPLs with different ratios of Se/S and reaction time.

5.1.2 Synthesis of $PbSe_{1-x}S_x$ nanoplatelets

$PbSe_{1-x}S_x$ NPLs is synthesized via a cation exchange process using different $CdSe_{1-x}S_x$ NPLs template and Pb precursors (including $PbCl_2$, $PbBr_2$, PbI_2 and $Pb(oleate)_2$). With different Pb precursors, the reaction temperature is varied in the 80-120 °C range for 30 min. Typically, in a 50 mL round-bottom flask, the lead precursor ($PbCl_2$, $PbBr_2$, PbI_2) (1 mmol), and OLA (5 mL) were degassed at 110 °C for 30 min. The reaction flask was restored with N_2 and the temperature was further raised to 160 °C while stirring for one hour. The temperature was further lowered to

80 °C. Two milliliters of the $CdSe_{1-x}S_x$ NPLs suspension is added in the above reaction flask and kept at 80 °C for 30 min. OA was added to the mixture when the temperature of the mixture decreased to 40 °C. After 30 min, the reaction was cooled to room temperature using cold water. Ethanol was added, then the suspension was centrifuged and the supernatant was removed. The NPLs were then dispersed in toluene or hexane for further characterization. For the cation exchange reaction by using $Pb(oleate)_2$, the mixture of PbO (1 mmol), OA (2 mmol) was heated to 240 °C for 15 min. Subsequently, the mixture was decreased to 120 °C and degassed for 30 min. The reaction flask was re-stored with N_2 and the $CdSe_{1-x}S_x$ NPLs (2 mL) in hexane was added to mixture. Then the reaction is kept at 120 °C for 30 min. The following injection of OA, cooling and purification processes are the same as demonstrated above.

5.1.2.1 Effect of lead precursors

The cation exchange on $CdSe_{1-x}S_x$ NPLs using various lead precursors induces the formation of the ultra-small $PbSe_{1-x}S_x$ NPLs (Figure 5.5). They are uniformly dispersed and show lateral dimensions (~4-6 nm) much smaller than the starting $CdSe_{1-x}S_x$ NPLs (Figure 5.2a). The formation mechanism of ultra-small NPLs can be described as follows: the alloyed $CdSe_{1-x}S_x$ NPLs exhibit polycrystalline structure, which may be due to the randomly oriented assembly of nanoscale seeds (Figure 5.6). The grain boundaries and dislocations in $CdSe_{1-x}S_x$ NPLs are likely to act as active sites for cation exchange due to their higher surface energy, resulting in the break-up of the original NPLs, as illustrated in the Scheme in Figure 5.1. XRD and selected area electron diffraction (SAED) indicate the typical rock salt phase and alloyed composition in $PbSe_{1-x}S_x$ NPLs (Figure 5.7). The calculated d spacing is ~0.31 nm, suggesting that the $PbSe_{1-x}S_x$ NPLs grow along {200} low surface energy planes, which is also observed in 2D chalcogenide nanomaterials.[155]

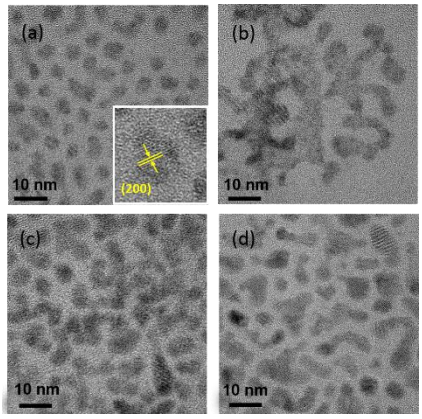

Figure 5.5 TEM Bright-field Images (BFI) of $PbSe_{1-x}S_x$ NPLs using different Pb precursors (Se:S=3:1), $PbBr_2$ (a) and $PbCl_2$ (b); PbI_2 (c) and $Pb(oleate)_2$ (d).

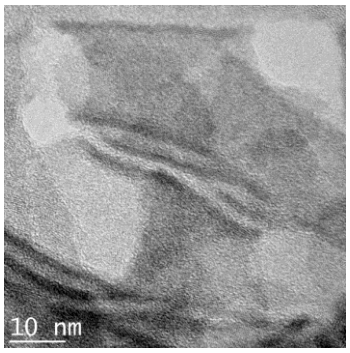

Figure 5.6 HR-TEM image of $CdSe_{1-x}S_x$ NPLs, Se:S=3:1.

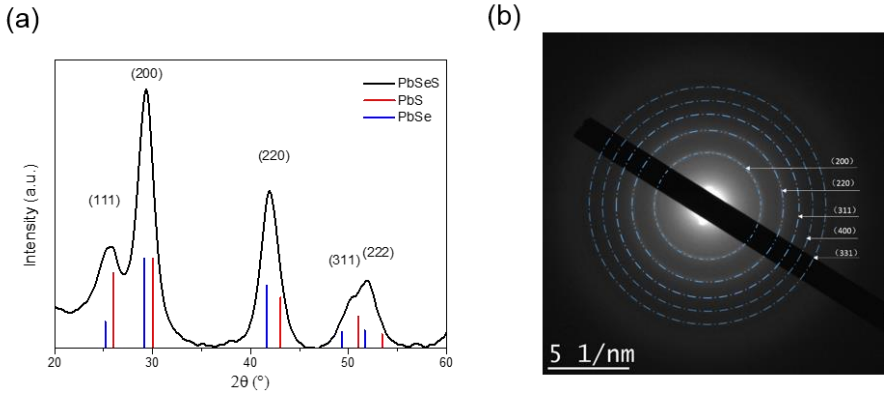

Figure 5.7 XRD and SAED patterns of rock salt structure $PbSe_{1-x}S_x$ NPLs (JCPDS No. 05-0592 for PbS, JCPDS No. 06-0354 for PbSe). Se:S=3:1. Lead precursor: $PbBr_2$.

X-ray Energy Dispersive Spectroscopy (EDS) and X-ray Photoelectron Spectroscopy (XPS) spectra of $CdSe_{1-x}S_x$ NPLs and $PbSe_{1-x}S_x$ NPLs using $PbBr_2$ precursor show the complete achievement of cation exchange process between Cd and Pb ions (Figures 5.4d and 5.8). Subsequent to the cation exchange reaction using $PbBr_2$ precursors, we obtained corresponding $PbSe_{1-x}S_x$ NPLs with different composition, showing similar morphologies (Figures 5.5a and 5.9). The thickness of the NPLs is ~2 nm as measured from the cross section TEM image of PbSe NPLs (Figure 5.9b), consistent with the dimension of template CdSe NPLs. As shown in Figure 5.9a, after cation exchange, a clear hollow structure was observed for PbSe NPLs, possibly due to etching by lead precursors during the cation exchange.[156]

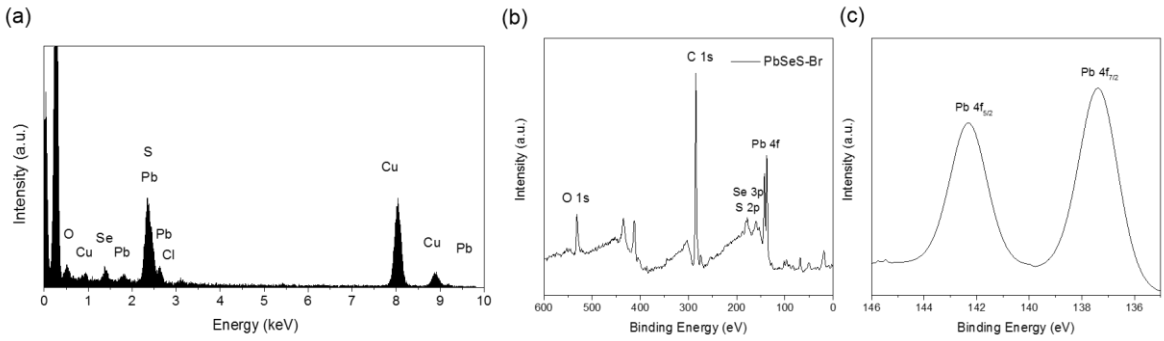

Figure 5.8 EDS (a) and XPS (b, c) spectra of $PbSe_{1-x}S_x$ NPLs (Se:S=3:1, $PbBr_2$ precursor).

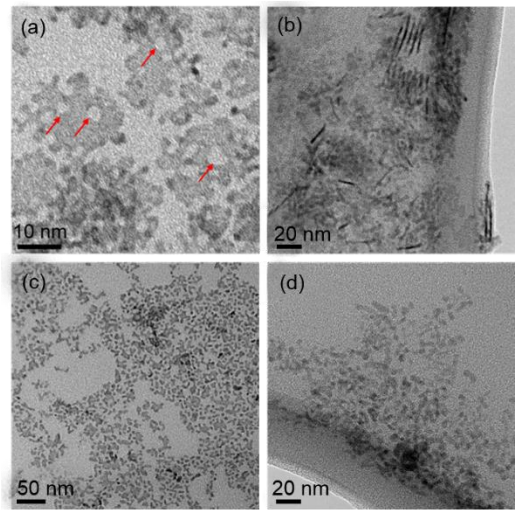

Figure 5.9 TEM images of obtained $PbSe_{1-x}S_x$ NPLs using different $CdSe_{1-x}S_x$ NPLs templates. Se:S=1:0 (a,b); Se:S=1:1, reaction time: 10 min (c) and 15 min (d).

5.1.3 Optical properties and theoretical simulation

The first-excitonic absorption and emission peaks of pure CdSe NPLs and alloyed $CdSe_{1-x}S_x$ NPLs before cation exchange are very well defined (Figure 5.10a) corresponding to 5 MLs and ~5-6 MLs in thickness, respectively, consistently with results found in the literature.[146] Prolonged reaction time results in a red-shift of both the absorption and emission peaks of $CdSe_{1-x}S_x$ NPLs due to the slight increase in thickness. The emission peaks cover the green to blue transition regime (518-463 nm) (Figure 5.10a, top). After cation exchange, the absorption band and PL emission peaks of $PbSe_{1-x}S_x$ NPLs shift from the visible to the NIR region (Figure 5.10a, bottom). In these NPLs the band edge emission peak can be tuned from 1182 to over 1382 nm by carefully varying the reaction conditions (lead precursors, reaction time and temperature, thickness and chemical composition of the parent $CdSe_{1-x}S_x$ NPLs). This is the so-called biologically transparent spectral window (1000-1350 nm), which is critical for *in vivo* optical imaging, and which has never been attained before for NIR NPLs. This particular feature is observed in Pb ternary NPLs thanks to their very small lateral dimensions, which enables strong quantum confinement in 3D (see Scheme

in Figure 5.1), leading to both very sharp PL emission and tunable emission wavelength, overcoming the limitations that affected larger sized PbS and PbS/CdS NPLs until now (in which the PL peak width is typically larger than 200 nm).[150]

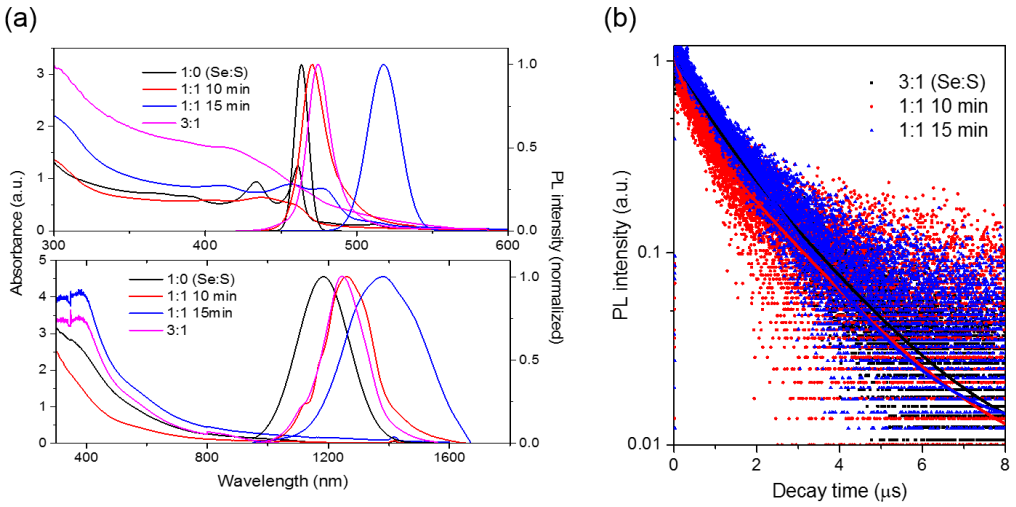

Figure 5.10 (a) Absorption and PL spectra of parent $CdSe_{1-x}S_x$ NPLs (top) and $PbSe_{1-x}S_x$ NPLs after cation exchange (bottom). (b) Typical PL decay curves and fitting curves (solid lines) for $PbSe_{1-x}S_x$ NPLs with various reaction conditions measured at the emission peak in toluene, shown on a semi-logarithmic scale. The excitation wavelength was set at 450 nm.

The ultra-small $PbSe_{1-x}S_x$ NPLs show record QY values compared to larger sized PbS NPLs (Table 5.1). The optimized sample, based on $PbBr_2$ precursor, results in a QY as high as 60% for $PbSe_{1-x}S_x$ NPLs, which is six-fold higher than the best reported QY for NIR NPLs (11% in Ref.[150]). Another key feature of our ultra-small NPLs is the increased fluorescence lifetime: an average lifetime of 1.5 μs was observed in $PbSe_{1-x}S_x$ NPLs (Figure 5.10b), much longer than that reported for large sized PbS NPLs (normally in the range 0.04-0.19 μs). This property suggests the longer radiative decay rate coming from the well passivated surface by Br, which can suppress the non-radiative decay, consistently with the higher QY.

Table 5.1 Optical properties of as-prepared $PbSe_{1-x}S_x$ NPLs. The used Pb precursors are $PbBr_2$ for sample 1-4, $PbCl_2$ for sample 5, PbI_2 for sample 6 and $Pb(oleate)_2$ for sample 7. Reaction time for $CdSe_{1-x}S_x$ NPLs template is 10 min[a)] and 15 min[b)]. Samples 8 and 9 refer to PbS and PbS/CdS NPLs reported in ref. [150].

Samples	Se/S	PL peak position (nm)	FWHM (nm)	QY (%)	PL lifetime (ns)
1	1:0	1180	200	5	590±60
2a)	1:1	1270	185	19	1800±40
3b)	1:1	1380	240	19	1600±60
4	3:1	1250	160	60	1620±50
5	3:1	1250	165	5	----
6	3:1	1250	160	31	1190±30
7	3:1	1250	165	0.1	----
8	----	1450	> 200	6	40
9	----	1330	> 200	11	190

To further understand the nature of high QY in small-sized NPLs, we estimated the radiative decay rate (k_{rad}) and the non-radiative decay rate (k_{nr}) in NPLs according to the equation 3.2: As both the QY and τ_{meas}, can be directly measured and $\tau_{rad} = 1/k_{rad}$, we can calculate the radiative decay (k_{rad}) and non-radiative decay (k_{nr}). For example, for the large sized PbS NPLs, k_{nr} is ~5 μs^{-1} (QY of 6%, lifetime of 0.19 μs).[150] The k_{nr} decreases to ~0.4 μs^{-1} (QY of 60%, lifetime of 1.5 μs). As the non-radiative decay rate is mainly induced by the surface chemical state (surface defects and traps),[111]

the large decrease of k_{nr} in small-sized NPLs directly proves that there are less surface defects/traps on small-sized NPLs due to better passivation with surface ligands.[133]

To further understand the optical properties of the ultra-small sized NPLs, we calculated the bandgap of various types of QDs and NPLs with different geometries (Figures 5.11). We calculated the eigenvalues of the Schrödinger equation for uncoupled electrons and holes, within an effective mass model for pure PbS and PbSe.[105] This model is based on the use of effective masses for electrons and holes and literature data on the bulk HOMO and LUMO absolute energies.[157-160] Figure 5.11 shows the variation of the bandgap as a function of the thickness and size of PbS(Se) NPLs. For comparison, simulations for spherical QDs are also included. For similar shell thicknesses of the NPLs, the bandgap increases with decreasing size. Our simulations of the energy bandgaps for large sized pure PbS(Se) NPLs or QDs are in good agreement with values found in the literature.[99,161-164] The measured energy bandgap for small $PbSe_{1-x}S_x$ NPLs is in very good agreement with calculations, confirming the 3D quantum confinement in ultra-small NPLs, which enables to tune their electronic states and PL emission.

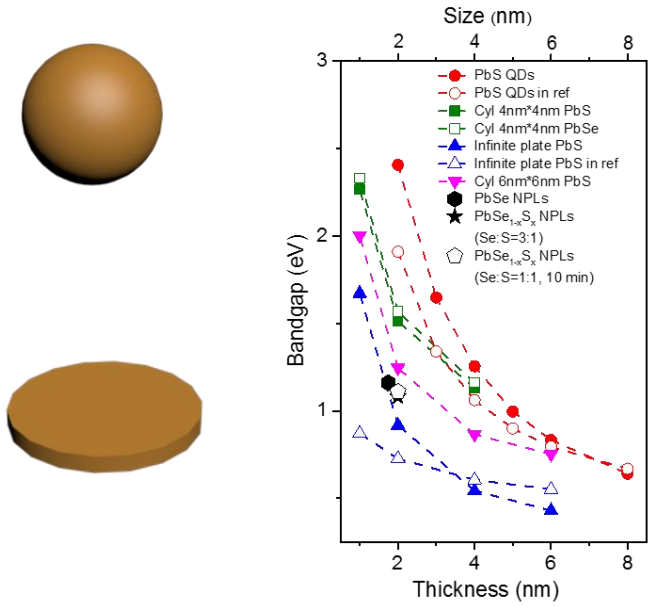

Figure 5.11 Schematic presentation of $PbSe_{1-x}S_x$ QDs and cylindrical (cyl) NPLs (on the left), experimental and simulated bandgap of PbS(Se) NPLs or QDs as a function of PbS size in diameter or thickness of NPLs (on the right). The dashed lines are guides to the eye. Experimental results for binary and ternary NPLs are also reported.

To obtain experimental evidence of the spectral position of the bandgap and understand the exciton dynamics, NPLs were studied by ultrafast transient transmission spectroscopy. Differential transmission measurements were carried out on samples dispersed in toluene. The laser source was a chirped pulse amplified Ti:Sapphire emitting 100-fs pulses at 800 nm and 1 kHz repetition rate. Pump pulses at 800 nm were modulated by a mechanical chopper at 500 Hz and were focused in a spot of (220 x 336) μm^2. Near infrared probe pulses were provided by white light supercontinuum generation focusing a part of the fundamental beam in a 4-mm thick YAG plate. Chirp-free differential transmission spectra $\Delta T/T = (T_{on} - T_{off})/T_{off}$, T_{on} and T_{off} being the transmission of the probe through the perturbed and unperturbed sample, were collected at different pump-probe delays by a fast optical multichannel analyser operating at the full repetition rate of the laser. The average number of excitons $\langle N_o \rangle$ was calculated by the formula $\langle N_o \rangle = \sigma_{abc} J_o$ [165] being σ_{abc} the absorption cross section at 800 nm and J_o the pump fluence in photons per cm^2.

We pumped the sample at 800 nm, well above the energy bandgap of all the nanostructures and probed in the near infrared in a broad spectral range (from 870 to 1450 nm), recording the transient transmission $\Delta T/T$ for various time delays with a time resolution of 100 fs. The $\Delta T/T$ spectra at short time delays (Figure 5.12, top) show a clear derivative feature that recovers in 2 ps; we ascribe this feature to the Stark effect resulting from a transient shift of the excited state absorption induced by two-exciton interaction; the shift ranges from 80 to 240 nm, depending on the sample, and it is towards the red, denoting the attractive two-exciton behaviour.[166,167] Figure 5.12a (bottom) shows the normalized $\Delta T/T$ spectra at 500 ps time delay. All spectra have a positive band due to photobleaching (PB) with peaks between 1050 and 1300 nm (Table 5.2) corresponding to the spectral position of the energy bandgap, in agreement with the theoretical values displayed in Figure 2c. These values, together with PL data (Figures 5.10a and 5.11), evidence a large Stokes shift of 110 nm typical of lead chalcogenides.[168-170] $\Delta T/T$ spectra do not show any negative band due to photo-induced absorption, denoting the absence of shallow traps, in agreement with the high PL QY.

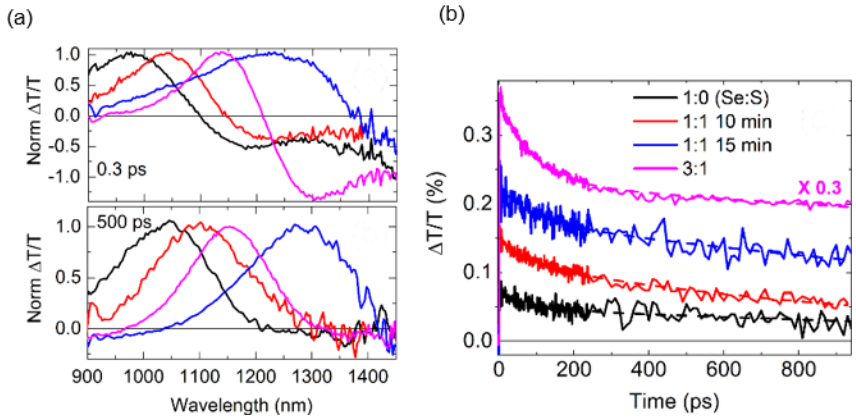

Figure 5.12 $\Delta T/T$ data for PbSe (black lines), $PbSe_{1-x}S_x$ 1:1 10 min (red lines), $PbSe_{1-x}S_x$ 1:1 15 min (blue lines) and $PbSe_{1-x}S_x$ 3:1 (magenta lines) NPLs for $\langle N_0 \rangle = 0.2$. (a, top) Normalized $\Delta T/T$ spectra for 0.3 ps pump-probe time delay; (a, bottom) Normalized $\Delta T/T$ spectra for 500 ps pump-probe time delay; (b) $\Delta T/T$ dynamics (solid lines) probed at the maximum of the PB with the respective biexponential fitting curve (dashed lines).

Table 5.2 $\Delta T/T$ properties of $PbSe_{1-x}S_x$ NPLs.

Samples	Ratio of Se/S	PB peak position (nm)	Stokes shift (nm)	PB FWHM (nm)
1	1:0	1050	130	196
2[a)]	1:1	1110	140	197
3[b)]	1:1	1300	80	207
4	3:1	1150	100	158

Reaction time for template of $PbSe_{1-x}S_x$ NPLs is 10 min[a)], 15 min[b)].

Figure 5.12b displays the $\Delta T/T$ dynamics associated with the PB of each sample. All dynamics have resolution-limited rise time, corresponding to a fast exciton thermalization from high lying energy states to the band-edge, followed by a biexponential decay. The shortest decay time is of the order of 70-80 ps; this value is typical of non-radiative Auger recombination processes,[171,172] which can appear for such small $\langle N_0 \rangle$ because of the large size distribution of NPLs. For higher $\langle N_0 \rangle$, from 1 to 4 (Figure 5.13), all $\Delta T/T$ dynamics show an initial faster decay, in agreement with Auger effect, as optical gain and stimulated emission have not been obtained. Interestingly, all the samples have a long lasting signal with a decay time in the ns range regardless of the exciton population. This denotes that multiexciton processes do not alter PL performance. Thus, all the data confirm that NPLs can be used in applications, in which a strong PL signal is required.

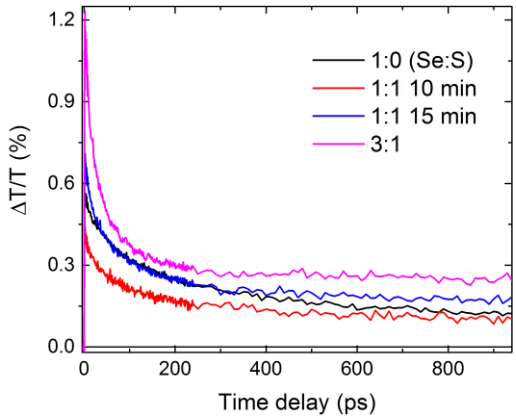

Figure 5.13 ΔT/T dynamics of at the peak of PB at $\langle N_0 \rangle$ =2 for different $PbSe_{1-x}S_x$ NPLs.

5.2 Fabrication and measurement of $PbSe_{1-x}S_x$ nanoplatelets based photoanode for solar-driven hydrogen generation

The design and synthesis of highly active and stable photocatalysts for PEC H_2 generation is vitally important to implement solar-to-hydrogen energy conversion processes. The preparation of ultrathin NPLs is important because these materials have unique properties, leading to superior photon to electron conversion efficiency compared to a 0D structure for solar hydrogen generation. As a proof-of-concept, I used as-synthesized NIR NPLs as photosensitizers for solar-driven PEC H_2 generation.

5.2.1 $PbSe_{1-x}S_x$ nanoplatelets based photoanode

Appropriate energy levels of 2D semiconductors will be favorable for efficient charge injection and thus leads to high hydrogen generation rate in PEC system. The accurate band alignment of the PEC system may be estimated according to Ultraviolet Photoelectron Spectroscopy (UPS) measurements and absorption spectra of NIR NPLs and TiO_2 film (Figure 5.14): the electrons are in the appropriate electronic band position to be injected into the TiO_2 film and then transferred to

the front electrode, finally flowing to the Pt counter electrode to participate in the reduction reaction of water for hydrogen generation (Figure 5.14).

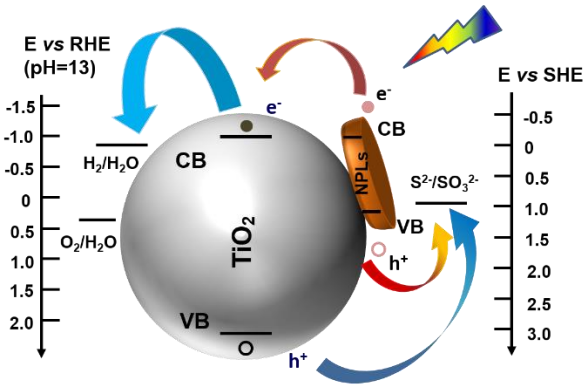

Figure 5.14 Accurate band alignment of PEC system. The band energy level of TiO_2 and NPL were estimated based on the UPS measurement.

5.2.1.1 Surface treatment of $PbSe_{1-x}S_x$ nanoplatelets

To enhance the photo/chemical stability of NPLs based photoanodes, the as-synthesized NPLs were treated by $Cd(OA)_2$, which can typically enhance the stability of materials due to the improved surface passivation compared to organic surface ligands. It is likely that Pb cations of NPLs is partially exchanged with Cd cations, to form a thin layer of CdS.[150] From Figure 5.15 and TEM images shown in Figure 5.16, the absorption of Cd-NPLs samples induces a slightly blue-shift in the NIR region, with no change in the morphology of NPLs sample before and after Cd exchange. Cd is detected in Cd-NPLs from XPS and EDS analysis (Figure 5.17), confirming its presence.

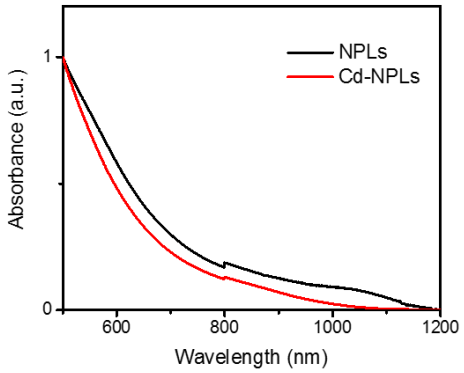

Figure 5.15 Absorption spectra of NIR NPLs and NPLs after Cd post-treatment (Cd-NPLs), Se:S = 3:1, reaction time for $CdSe_{1-x}S_x$ template is 15 min.

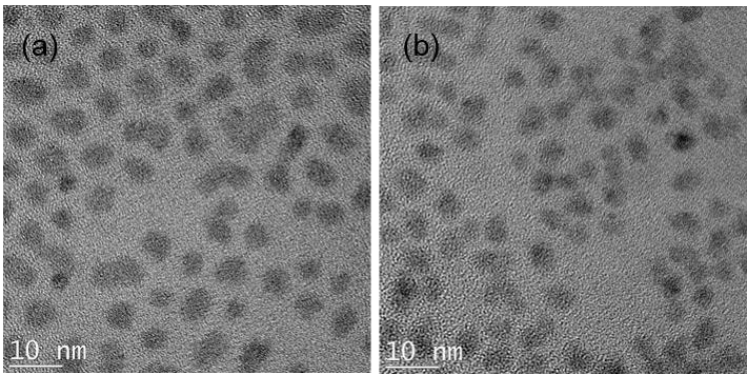

Figure 5.16 TEM images of Cd capped $PbSe_{1-x}S_x$ NPLs (a) and Cd-$PbSe_{1-x}S_x$ NPLs (b) obtained after further cation exchange. $CdSe_{1-x}S_x$ NPLs templates preparation parameters: Se:S=3:1, reaction time: 15min.

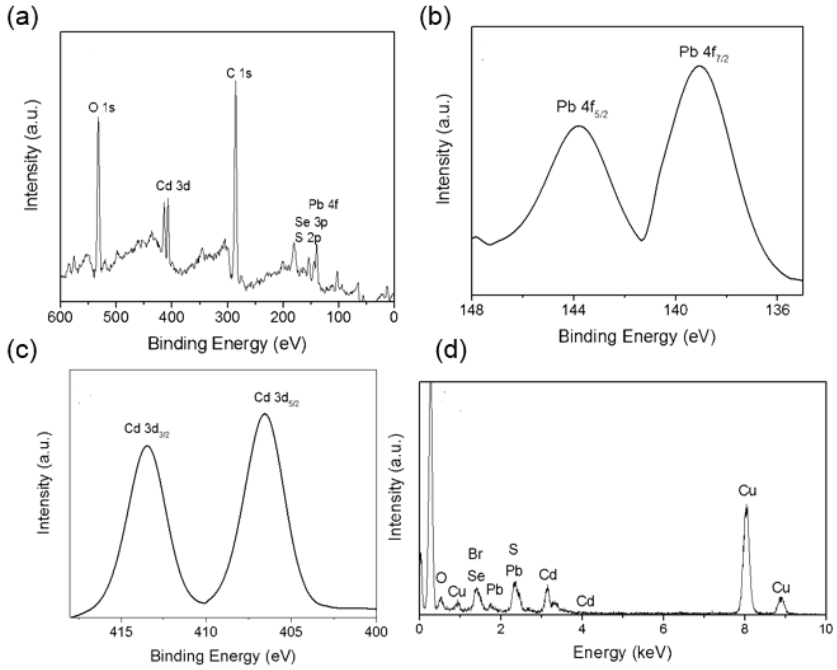

Figure 5.17 XPS (a), high resolution XPS (b, c) and EDS (d) spectra of Cd-NPLs.

5.2.1.2 Preparation of $PbSe_{1-x}S_x$ nanoplatelets based photoanode

The mesoporous TiO_2 thin film was prepared by Doctor-blade technique.[154] Specifically, A thin and compact TiO_2 layer was spin coated on FTO-coated glass at 6000 rpm for 30 s by using the commercial solution Ti-Nanoxide BL/SC (Solaronix) or using TiO_x flat film precursor solution. Then, the films were annealed in air at 500 °C for 30 min after drying and cooled down to room temperature. A 20 nm particle size paste named as 18NR-T (paste A, from Dyesol) and a blend of active anatase particles (≈20 nm) and larger anatase particles (up to 450 nm) paste (18 NR-AO, paste B, from Dyesol) were tape casted, forming a mesoporous film. Following a reannealing in air at 500 °C for 30 min after drying and cooled down to room temperature, 1T+1S structure TiO_2 film is obtained. For 1S+1S structure, the procedure is similar as mentioned above, but larger anatase particles (up to 450 nm) paste (18 NR-AO,paste B, from Dyesol) were tape casted for twice after preparation of TiO_2 blocking layer.

Furthermore, the NPLs were deposited into the thin film by electrophoretic deposition (EPD). In details, a pair of TiO_2 FTO slides were vertically immersed in the NIR NPLs suspension and facing each other with a distance of 1 cm. A voltage of 200 V was applied for 30, 45 or 60 min. The samples were then rinsed three times with toluene and dried with N_2 at room temperature.

5.2.1.3 Post-treatment of $PbSe_{1-x}S_x$ nanoplatelets based photoanode

NPLs based TiO_2 film is dipped in 20 mL cetyltrimethylammonium bromide (CTAB)/methanol solution (10 mg/mL) for 1 min. Then the photoanode is rinsed with methanol for 1 min. Subsequently, for the post-annealing treatment, the photoanode was kept at 150 °C for 15 min under vacuum (Dryfast 2014B-01) condition. Finally, 2 ML ZnS was subsequently deposited using SILAR to prevent and reduce photocorrosion. The structure of the anode is characterized by scanning electron microscope-energy dispersive X-ray spectroscopy (SEM-EDS) mapping in Figure 5.18.

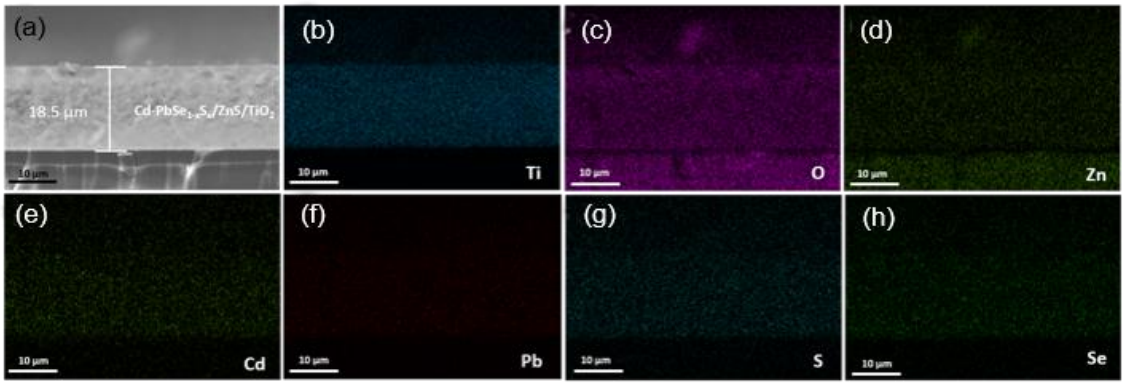

Figure 5.18 (a) Cross-sectional Scanning Electron Microscope (SEM) image of Cd-NPLs-sensitized photoanode. (b-h) EDS mapping analysis of all the related elements in TiO_2/ Cd-$PbSe_{1-x}S_x$/ZnS photoelectrode including Ti (b), O (c), Zn (d), Cd (e), Pb (f), S (g) and Se (h).

5.2.2 Performance of $PbSe_{1-x}S_x$ nanoplatelets based photoanode for solar-driven hydrogen generation

PEC performance of the photoelectrodes was evaluated in a three-electrode configuration, consisting of a NPLs-TiO_2 photoanode working electrode, a Pt counter electrode (CE), and a KCl saturated Ag/AgCl reference electrode. An insulating epoxy resin was used to cover the sample surface except the active area to avoid any direct contact between the electrolyte and the conducting back-contact and/or the connecting wire. Then the sample was fully immersed in the electrolyte with pH = 13, containing 0.25 M Na_2S and 0.35 M Na_2SO_3. All potentials were measured with respect to Ag/AgCl during PEC test and they were converted to the reversible hydrogen electrode (RHE) scale with the following expression $V_{RHE} = V_{Ag/AgCl} + 0.197 + pH\times(0.059)$. The photoresponse was measured using an Oriel LCS-100 solar simulator (AM1.5 G, 94011A, S/N: 244, MFD:09/15). The sample was placed 15 cm far from the window of the light source and the light intensity measured by thermopile was ~100 mW cm^{-2}. The working area of the photoanode was ~0.16 cm^2. All the current versus potential measurements were carried out at a 20 mV/s sweep rate. Current density as a function of time was measured at 0.2 V vs. RHE under continues AM 1.5 G illumination. The IPCE was derived from current-voltage measurements using different band-pass optical filters.[154]

The PEC performance of NPLs is demonstrated in Figure 5.19. The saturated photocurrent density is obtained as ~0.8 mA/cm^2 for pure NPLs treated with Cd cations at 40 °C. Due to surface oxidation during anode preparation, we observe the apparent oxidation peak at ~-0.05 V vs RHE in the J-V curve. This oxidation may be prevented by preparing the anode in a glove box. By optimizing the photoanode through different TiO_2 film structures and electrophoretic deposition time, the saturated photocurrent density of the Cd-NPLs based photoanode in PEC system is

enhanced to 3.8 mA/cm^2. Further ligand exchange with CTAB and post-annealing treatment at 150 °C for 15 min under vacuum condition induces an increase in the photocurrent density to ~5.0 mA/cm^2 at 1.0 V vs RHE, almost 3 times higher than NIR core/shell PbS/CdS QDs (absorption spectrum shown in Figure 5.20) based photoanode (Table 5.3). This photocurrent density is comparable to the values reported from PEC systems using colloidal PbS/CdS QDs (3-11 mA/cm^2),[154,173] hematite (3.05 mA/cm^2)[174] and metal oxides e.g. Cu_2O nanowires (10 mA/cm^2).[175]

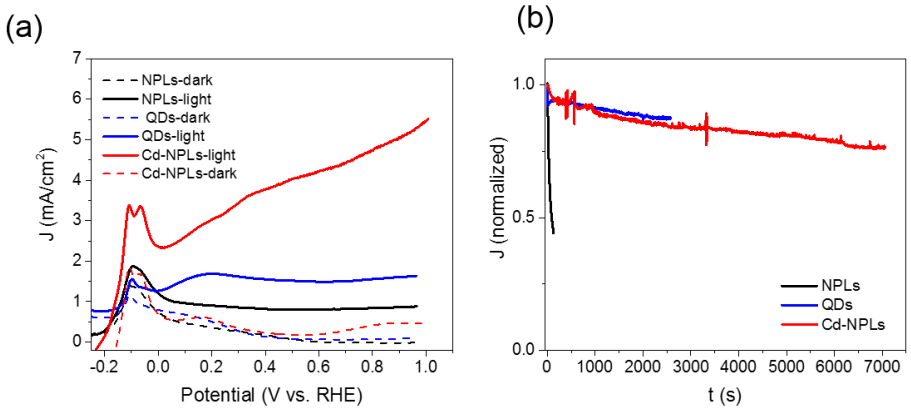

Figure 5.19 (a) Current density-potential dependence of TiO_2/NPLs/ZnS, TiO_2/PbS/CdS QDs/ZnS and TiO_2/Cd-NPLs/ZnS (with ligand exchange and post-annealing treatment) film photoanode in dark and under AM 1.5G illumination (100 mW/cm^2). (b) Measured current density ratio vs. illumination time at 0.8 V vs. RHE under AM 1.5G illumination (100 mW/cm^2) for the photoanodes mentioned in b.

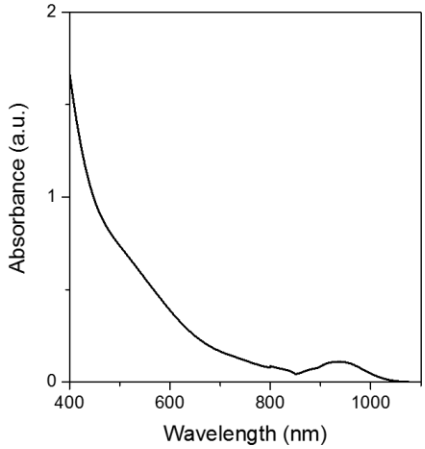

Figure 5.20 Absorption spectrum of PbS/CdS core/shell QDs.

Table 5.3 Optimization of PEC photoanodes. 1T and 1S mentioned represent 1 transparent layer and 1 scattering layer of TiO_2 film, respectively.

Samples	EPD deposition time (min)	TiO_2 film structure	SILAR	J (mA/cm^2)
1	30	1T+1S	2 cycles ZnS	3.8
2	30	1S+1S	2 cycles ZnS	3.4
3	45	1T+1S	2 cycles ZnS	1.8
4	60	1T+1S	2 cycles ZnS	2.4

Furthermore, IPCE was derived by current–voltage measurements (Figure 5.21). The results are consistent with the broad NIR absorption of the NPLs (Figure 5.14), with contribution to IPCE originating from the UV-Vis and NIR region, up to 950 nm. The current density in NPLs based PEC device drops very quickly, ~60% drop of original value after 140 seconds illumination (Figure 5.19b). In a big contrast, the photostability of Cd-NPL (100 °C)-based photoanode is largely improved compared to NPLs without Cd-treatment, comparable to that of PbS/CdS QD-based photoanode (Figure 5.19b). This stability is among the best reported in PbS or PbSe semiconductor-based PEC device. The improved stability of PEC device based on Cd-treated NPLs compared to bare NPLs is due to the efficient surface passivation by CdS shell, which can protect the core materials during cell preparation and operation.

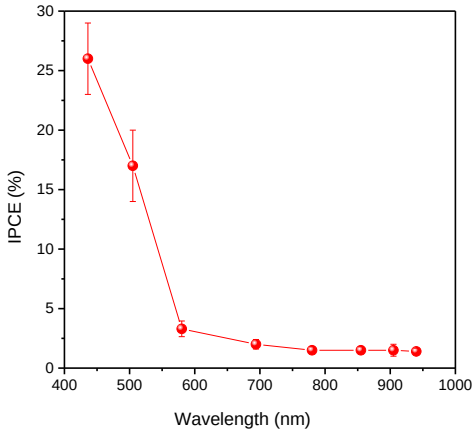

Figure 5.21 IPCE at 1.0 V versus RHE for the sample of TiO_2/ NPLs treated with ZnS.

5.3 Summary

In summary, an easy approach to synthesize ultra-small NIR NPLs via template-assisted cation exchange was demonstrated. The ultra-small sized NIR NPLs with surface compact ligands passivated exhibits 3D quantized electronic behavior, QY as high as ~60% and tunable energy gap with tunable emission wavelength range, showing great potential for application in optical devices, such as LEDs, thermal sensors, luminescent solar concentrators, solar cells and hydrogen production. The Cd-NPL-based photoanode exhibits excellent photostability under illumination and almost 3 times higher saturated photocurrent density of ~5.0 mA/cm^2 at 1.0 V vs RHE than that of core/shell PbS/CdS QD-based photoanode, a record for NPLs based photoelectrode in solar-powered PEC device. This approach can be used to synthesize other small sized semiconductor NPLs such as HgS(Se), BiS(Se), CuSnS(Se), CuZnS(Se), CuInS(Se). Our results suggest that the 2D small sized NPLs are good candidates for energy applications, such as water splitting and solar cells, through efficient band gap engineering, effective surface passivation and outstanding photostability.

Chapter 6 Conclusions and perspectives

6.1 Conclusions

Semiconductor NCs have been widely investigated in recent decades due to their unique optical, electrical properties and various applications in solar technologies, such as solar cell, LSCs and solar-driven water splitting. Among these semiconductor NCs, colloidal semiconducting QDs, are regarded as promising candidates for LSCs applications, with size/composition- tunable optical properties (including high PLQY, broad absorption, high photo/chemical stability, *etc*). However, it is still challenging to synthesize colloidal QDs with large Stokes shift, high PLQY and broad absorption spectrum, which are the main criteria for large-area high efficient LSCs fabrications. Part of objectives in this thesis were the design and synthesis of efficient emitter for LSCs application.

In chapter 2, we demonstrated the application of mixed-halide $CsPb(Br_xI_{1-x})_3$ perovskite QDs as highly emissive fluorophores in high performance large-area LSCs. Specifically, we synthesized $CsPb(Br_xI_{1-x})_3$ perovskite QDs via a hot-injection approach and incorporated them into PLMA-EGDA polymer matrix, resulting in a semitransparent composite with the absorption spectrum ranging from 300 to 650 nm. The prototype LSC based on the perovskite $CsPb(Br_xI_{1-x})_3$ QDs exhibited an external optical efficiency of 2% with a G factor of 45. According to the theoretical calculation, the optical external efficiency of LSCs can be further improved by using perovskites QDs with higher QY and larger Stokes shift. Moreover, the LSCs exhibit long-term air stability without any noticeable variation in PL intensity and lifetime under 4 W UV light illumination for over four hours.

In chapter 3, we fabricated large-area, low reabsorption loss, high efficient LSCs using NIR PbS/CdS QDs. The core/shell PbS/CdS QDs with tunable core size and shell thickness were synthesized via the combination of hot-injection method and cation exchange process. The larger Stokes shift of PbS/CdS QDs with high QY of 40-50% was obtained due to the strong core-to shell leakage of electrons, when the core size is less than 3 nm and the shell is thicker than 0.5 nm. The LSCs based on this type of QDs exhibit excellent optical performance including: (i) broad absorption covering the UV-vis-NIR range (1.1-4 eV); (ii) unchanged PL peak position (1.38 eV) and lifetime after incorporation into the polymer matrix; (iii) small PL loss over large areas, and (iv) high optical efficiency with respect to bare PbS QDs. The semi-transparent LSC shows an optical efficiency of 6.1% (G = 10), which is a record optical efficiency for planar NIR PbS QD based LSCs.

In chapter 4, we demonstrated low-cost, large-area and high-efficiency LSCs based on metal-free, colloidal C-dots dispersed in a PLMA polymer matrix or PVP on glass substrate. The as-synthesized C-dots via solvothermal method were surface-modified with OLA, showing a reduced absorption/PL spectral overlap, a PLQY of ~ 30% and an excellent photo-/chemical stability without any emission loss during the entire process of their encapsulation into a polymer matrix. The large-area C-dot based LSCs exhibit an external optical efficiency of 1.2% (G = 10) and a quantum efficiency of 4% (G = 38), comparable to those of semi-transparent highly efficient inorganic QD based LSCs mentioned above. Furthermore, the tandem semi-transparent thin film LSCs (100 cm^2) exhibit an external optical efficiency of 1.1%. The as-fabricated LSCs are highly stable in air and do not exhibit any noticeable variation in PL under UV light illumination (1.3 W/cm^2) for over twelve hours. Based on the theoretical simulation, the external optical efficiency of LSCs can be further enhanced by improving the absorption range, enhancing the PLQY and

increasing the quality factor by modifying the surface of C-dots. The cost of C-dot based LSCs would be cheaper compared to LSCs made of inorganic QDs, considering the easier synthesis using abundant and low-cost carbon elements and their simple disposal after use.

In addition, ultra-thin semiconducting NPLs with high carrier mobility, narrow emission spectrum and high PLQY draw much attention in their application of solar technologies. It is demanding to synthesize NIR NPLs with high PLQY and colloidal photo/chemical stability. In chapter 5, we synthesized ultrasmall NIR $PbSe_{1-x}S_x$ NPLs by cation exchange on template ultrathin $CdSe_{1-x}S_x$ NPLs. The grain boundaries and dislocations in polycrystalline $CdSe_{1-x}S_x$ NPLs are likely to act as active sites for cation exchange due to their higher surface energy, resulting in the break-up of the original NPLs. The $PbSe_{1-x}S_x$ NPLs NPLs with lateral dimensions below 10 nm exhibit continuously tunable PL emission ranging from 1180 to 1380 nm due to the variation of the S/Se ratio. The ultrasmall sized NIR NPLs with surface compact ligands passivated exhibits 3D quantized electronic behavior, QY as high as ~60%. The Cd treated NIR NPLs was used as absorber and sensitizer for solar driven hydrogen generation. A saturated photocurrent density of ~5.0 mA cm^{-2} at 1.0 V versus RHE was obtained under solar illumination, corresponding to hydrogen generation rate of ~44 mL/cm^2 per day.

6.2 Perspectives

Despite a tremendous effort invested over the last several years in exploring the synthesis, properties and applications of core/shell QDs in LSCs, a number of questions and challenges still remain unanswered. The overall optical efficiency of large-area LSCs is still low, which is still far below the value for real commercial application (> 10%). It is still very challenging to scale up the size of LSCs, meanwhile keep their optical performance. In addition, it is very difficult to scale-up the chemical reaction towards synthesizing QDs with large quantities, while still obtaining high

quality core/shell QDs. Future work should focus on: (1) developing a general synthetic approach which could meet the requirements of reproducible simple synthesis with large scale for core/shell QDs. For example, all current synthetic approaches rely on a relatively high reaction temperature (typically 100-320 °C) using toxic organic solvent and ligands. Thus, identifying new precursors for the low temperature synthesis of core/shell QDs is another emerging direction; (2) using non-toxic semiconducting materials or solvents to synthesize high quality core/shell QDs. Commonly used inorganic QDs for LSCs contain toxic elements, such as Cd, Pb etc. Even if CuInSe(S) QDs are less toxic, the synthesis procedure involves the use of toxic organic solvents and expensive precursors. It is a very promising approach to produce the colloidal QDs in water using less-toxic elements;[176] (3) improving the optical efficiency of LSCs by designing and synthesizing core/shell QDs with high QY, wide absorption spectrum, large Stokes shift and excellent photo-, colloidal- and thermal- stability through a careful selection of core/shell materials, core size, shell thickness and chemical composition. For example, NIR "giant" CISeS/CIS QDs exhibit a typical quasi type II structure, with a large Stokes shift and wide absorption spectrum up to NIR region owing to the large volume of CIS shell (band gap, 1.5 eV, equal to 826 nm). Other method which can be used to improve the performance of LSCs based on core/shell QDs is to couple the QDs with certain metal nanocrystals (Ag, Au), which has been found to increase their emission intensity and the absorption by increasing the QY and excitation rate due to plasmonic effects;[177-179] (4) improving the stability of QDs by coating the QDs with a silica shell which not only avoid the possible quenching during incorporating core/shell QDs in the LSC device, but also isolate the QDs surface from surrounding environments, such as water, light and other molecules; (5) developing new type of non-toxic high efficient QDs, e.g. C-dots and silicon QDs. Even Si QDs or C-dots used for LSCs, the absorption range is still narrow and the QY is still low. Future direction for these QDs

may focus on the optimization of structure of Si or C-dots or further coating such QDs with a further protective layer to tailor their PLQYs and Stokes shift. To commercially realize the large-area LSCs, other challenges should be considered including the efficiency, lifetime and durability of LSCs, and the cost of their installation and fabrication. The expected requirements at least include the 10% of external optical efficiency, five-year outdoor use with efficiency decrease less than 20% with the cost less than 0.1$/watt.

Moreover, the approach demonstrated in chapter 5 can be used to synthesize other small sized semiconductor NPLs, such as HgS(Se), BiS(Se), CuSnS(Se), CuZnS(Se), and CuInS(Se). The 2D small-sized NIR NPLs are suggested as good candidates for energy applications, such as water splitting and solar cells, through efficient bandgap engineering, effective surface passivation, and outstanding photostability.

Bibliography:

(1) Mirchi, A.; Hadian, S.; Madani, K.; Rouhani, O. M.; Rouhani, A. M. *Energies* **2012**, *5*, 2626.

(2) Khan, N.; Saleem, Z.; Wahid, A. *Renew. Sust. Energ. Rev.* **2008**, *12*, 1959.

(3) Carlessi, F.; Junior, M. O. H. A.; Neto, J.; Spacek, A.; Coelho, V.; Schaeffer, L.; Bordon, H.; Perrone, O.; Bretas, A.; Bibao, *International Conference on Renewable Energies and Power Quality* **2013**.

(4) Petroleum, B.; London: *British Petroleum*: **2016**.

(5) Kannan, N.; Vakeesan, D. *Renew. Sust. Energ. Rev.* **2016**, *62*, 1092.

(6) Bhattarai, K.; Stalick, W. M.; McKay, S.; Geme, G.; Bhattarai, N. *J. Environ. Sci. Health., Part A* **2011**, *46*, 1424.

(7) Kumar, Y.; Ringenberg, J.; Depuru, S. S.; Devabhaktuni, V. K.; Lee, J. W.; Nikolaidis, E.; Andersen, B.; Afjeh, A. *Renew. Sust. Energ. Rev.* **2016**, *53*, 209.

(8) Kaygusuz, K. *Energ. Source.* **2002**, *24*, 803.

(9) Energy consumption by form, Department of Energy and Natural Resources and Statistics Canada. https://mern.gouv.qc.ca/energie/statistiques/statistiques-consommation-forme.jsp (accessed **2016**).

(10) Himmel, M. E.; Ding, S. Y.; Johnson, D. K.; Adney, W. S.; Nimlos, M. R.; Brady, J. W.; Foust, T. D. *Science* **2007**, *315*, 804.

(11) Devabhaktuni, V.; Alam, M.; Depuru, S. S. S. R.; Green, R. C.; Nims, D.; Near, C. *Renew. Sust. Energ. Rev.* **2013**, *19*, 555.

(12) Carlson, D. E.; Wronski, C. R. *Appl. Phys. Lett.* **1976**, *28*, 671.

(13) Green, M. A.; Emery, K.; Hishikawa, Y.; Warta, W.; Dunlop, E. D. *Prog. Photovoltaics* **2015**, *23*, 1.

(14) Cui, Y.; Lieber, C. M. *Science* **2001**, *291*, 851.

(15) Kamat, P. V. *J. Phys. Chem. C* **2007**, *111*, 2834.

(16) Scharber, M. C.; Mühlbacher, D.; Koppe, M.; Denk, P.; Waldauf, C.; Heeger, A. J.; Brabec, C. J. *Adv. Mater.* **2006**, *18*, 789.

(17) Grätzel, M. *J. Photoch. Photobio. C* **2003**, *4*, 145.

(18) Günes, S.; Neugebauer, H.; Sariciftci, N. S. *Chem. Rev.* **2007**, *107*, 1324.

(19) Liu, M.; Johnston, M. B.; Snaith, H. J. *Nature* **2013**, *501*, 395.

(20) Mathew, S.; Yella, A.; Gao, P.; Humphry-Baker, R.; Curchod, B.F.; Ashari-Astani, N.; Tavernelli, I.; Rothlisberger, U.; Nazeeruddin, M.K.; Grätzel, M. *Nat. Chem.* **2014**, *6*, 242.

(21) Mishra, A.; Fischer, M. K.; Bäuerle, P. *Angew. Chem. Int. Ed.* **2009**, *48*, 2474.

(22) Meinardi, F.; Ehrenberg, S.; Dhamo, L.; Carulli, F.; Mauri, M.; Bruni, F.; Simonutti, R.; Kortshagen, U.; Brovelli, S. *Nat. Photonics* **2017**, *11*, 177.

(23) Debije, M. G.; Verbunt, P. P. *Adv. Energy Mater.* **2012**, *2*, 12.

(24) Chemisana, D. *Renew. Sust. Energ. Rev.* **2011**, *15*, 603.

(25) Wiegman, J.; Van der Kolk, E. *Sol. Energy Mater. Sol. Cells* **2012**, *103*, 41.

(26) Currie, M. J.; Mapel, J. K.; Heidel, T. D.; Goffri, S.; Baldo, M. A. *Science* **2008**, *321*, 226.

(27) van Sark, W. G.; Barnham, K. W.; Slooff, L. H.; Chatten, A. J.; Büchtemann, A.; Meyer, A.; McCormack, S. J.; Koole, R.; Farrell, D. J.; Bose, R. *Opt. Express* **2008**, *16*, 21773.

(28) Bailey, S. T.; Lokey, G. E.; Hanes, M. S.; Shearer, J. D.; McLafferty, J. B.; Beaumont, G. T.; Baseler, T. T.; Layhue, J. M.; Broussard, D. R.; Zhang, Y.-Z. *Sol. Energy Mater. Sol. Cells* **2007**, *91*, 67.

(29) Drake, J.; Lesiecki, M.; Sansregret, J.; Thomas, W. *Appl. Opt.* **1982**, *21*, 2945.

(30) Baumberg, I.; Berezin, O.; Drabkin, A.; Gorelik, B.; Kogan, L.; Voskobojnik, M.; Zaidman, M. *Polym. Degrad. Stab.* **2001**, *73*, 403.

(31) Batchelder, J.; Zewail, A.; Cole, T. *Appl. Opt.* **1981**, *20*, 3733.

(32) Purcell-Milton, F.; Gun'ko, Y. K. *J. Mater. Chem.* **2012**, *22*, 16687.

(33) Bradshaw, L. R.; Knowles, K. E.; McDowall, S.; Gamelin, D. R. *Nano Lett.* **2015**, *15*, 1315.

(34) Chan, C. K.; Peng, H.; Liu, G.; McIlwrath, K.; Zhang, X. F.; Huggins, R. A.; Cui, Y. *Nat. Nanotechnol.* **2008**, *3*, 31.

(35) Zalba, B.; Marín, J. M.; Cabeza, L. F.; Mehling, H. *Appl. Therm. Eng.* **2003**, *23*, 251.

(36) Walter, M. G.; Warren, E. L.; McKone, J. R.; Boettcher, S. W.; Mi, Q.; Santori, E. A.; Lewis, N. S. *Chem. Rev.* **2010**, *110*, 6446.
(37) Mino, L.; Agostini, G.; Borfecchia, E.; Gianolio, D.; Piovano, A.; Gallo, E.; Lamberti, C. *J. Phys. D: Appl. Phys.* **2013**, *46*, 423001.
(38) Smith, A. M.; Nie, S. *Acc. Chem. Res.* **2010**, *43*, 190.
(39) Rossetti, R.; Ellison, J.; Gibson, J.; Brus, L. E. *J. Chem. Phys.* **1984**, *80*, 4464.
(40) Medintz, I. L.; Uyeda, H. T.; Goldman, E. R.; Mattoussi, H. *Nat. Mater.* **2005**, *4*, 435.
(41) Michalet, X.; Pinaud, F.; Bentolila, L.; Tsay, J.; Doose, S.; Li, J.; Sundaresan, G.; Wu, A.; Gambhir, S.; Weiss, S. *Science* **2005**, *307*, 538.
(42) Reiss, P.; Protiere, M.; Li, L. *Small* **2009**, *5*, 154.
(43) Bera, D.; Qian, L.; Tseng, T.-K.; Holloway, P. H. *Materials* **2010**, *3*, 2260.
(44) Coe, S.; Woo, W.-K.; Bawendi, M.; Bulović, V. *Nature* **2002**, *420*, 800.
(45) Lee, Y. L.; Lo, Y. S. *Adv. Funct. Mater.* **2009**, *19*, 604.
(46) Meinardi, F.; Colombo, A.; Velizhanin, K. A.; Simonutti, R.; Lorenzon, M.; Beverina, L.; Viswanatha, R.; Klimov, V. I.; Brovelli, S. *Nat. Photonics* **2014**, *8*, 392.
(47) Chen, H. M.; Chen, C. K.; Chang, Y. C.; Tsai, C. W.; Liu, R. S.; Hu, S. F.; Chang, W. S.; Chen, K. H. *Angew. Chem. Int. Ed.* **2010**, *122*, 6102.
(48) Meinardi, F.; McDaniel, H.; Carulli, F.; Colombo, A.; Velizhanin, K. A.; Makarov, N. S.; Simonutti, R.; Klimov, V. I.; Brovelli, S. *Nat. Nanotechnol.* **2015**, *10*, 878.
(49) Li, C.; Chen, W.; Wu, D.; Quan, D.; Zhou, Z.; Hao, J.; Qin, J.; Li, Y.; He, Z.; Wang, K. *Sci. Rep.* **2015**, *5*, 17777.
(50) Li, H.; Wu, K.; Lim, J.; Song, H.-J.; Klimov, V. I. *Nat. Energy* **2016**, *1*, 16157.
(51) Zhao, H.; Benetti, D.; Jin, L.; Zhou, Y.; Rosei, F.; Vomiero, A. *Small* **2016**, *12*, 5354.
(52) Hofkens, J.; Roeffaers, M. B. J. *Nature* **2016**, *530*, 36.
(53) Gratzel, M. *Nature* **2001**, *414*, 338.
(54) Yan, Y.; Xia, B.; Ge, X.; Liu, Z.; Wang, J.-Y.; Wang, X. *ACS Appl. Mater. Inter.* **2013**, *5*, 12794.
(55) Wang, Y.; Xie, C.; Liu, D.; Huang, X.; Huo, J.; Wang, S. *ACS Appl. Mater. Inter.* **2016**, *8*, 18652.
(56) Zheng, J. Y.; Song, G.; Hong, J.; Van, T. K.; Pawar, A. U.; Kim, D. Y.; Kim, C. W.; Haider, Z.; Kang, Y. S. *Cryst. Growth. Des.* **2014**, *14*, 6057.
(57) Ji, M.; Cai, J.; Ma, Y.; Qi, L. *ACS Appl. Mater. Inter.* **2015**, *8*, 3651.
(58) Lei, F.; Sun, Y.; Liu, K.; Gao, S.; Liang, L.; Pan, B.; Xie, Y. *J. Am. Chem. Soc.* **2014**, *136*, 6826.
(59) Liu, C.; Yang, Y.; Li, W.; Li, J.; Li, Y.; Chen, Q. *Sci. Rep.* **2016**, *6*, 23451.
(60) Xu, Y.; Zhao, W.; Xu, R.; Shi, Y.; Zhang, B. *Chem. Commun.* **2013**, *49*, 9803.
(61) Zhao, H.; Zhou, Y.; Benetti, D.; Ma, D.; Rosei, F. *Nano Energy* **2017**, *37*, 214.
(62) Zhou, Y.; Benetti, D.; Fan, Z.; Zhao, H.; Ma, D.; Govorov, A. O.; Vomiero, A.; Rosei, F. *Adv. Energy Mater.* **2016**, *6*, 1501913.
(63) Zhou, Y.; Benetti, D.; Tong, X.; Jin, L.; Wang, Z. M.; Ma, D.; Zhao, H.; Rosei, F. *Nano Energy* **2018**, *44*, 378.
(64) Zhou, Y.; Celikin, M.; Camellini, A.; Sirigu, G.; Tong, X.; Jin, L.; Basu, K.; Tong, X.; Barba, D.; Ma, D.; Sun, S.; Vidal, F.; Zavelani-Rossi, M.; Wang, Z. M.; Zhao, H.; Vomiero, A.; Rosei, F. *Adv. Energy Mater.*, 7, 1602728.
(65) Yassitepe, E.; Yang, Z.; Voznyy, O.; Kim, Y.; Walters, G.; Castañeda, J. A.; Kanjanaboos, P.; Yuan, M.; Gong, X.; Fan, F. *Adv. Funct. Mater.* **2016**, *26*, 8757.
(66) Swarnkar, A.; Chulliyil, R.; Ravi, V. K.; Irfanullah, M.; Chowdhury, A.; Nag, A. *Angew. Chem. Int. Ed.* **2015**, *127*, 15644.
(67) Wang, H. C.; Lin, S. Y.; Tang, A. C.; Singh, B. P.; Tong, H. C.; Chen, C. Y.; Lee, Y. C.; Tsai, T. L.; Liu, R. S. *Angew. Chem. Int. Ed.* **2016**, *55*, 7924.
(68) Protesescu, L.; Yakunin, S.; Bodnarchuk, M. I.; Krieg, F.; Caputo, R.; Hendon, C. H.; Yang, R. X.; Walsh, A.; Kovalenko, M. V. *Nano Lett.* **2015**, *15*, 3692.
(69) Chen, X.; Peng, L.; Huang, K.; Shi, Z.; Xie, R.; Yang, W. *Nano Res.* **2016**, *9*, 1994.
(70) Pathak, S.; Sakai, N.; Wisnivesky Rocca Rivarola, F.; Stranks, S. D.; Liu, J.; Eperon, G. E.; Ducati, C.; Wojciechowski, K.; Griffiths, J. T.; Haghighirad, A. A. *Chem. Mater.* **2015**, *27*, 8066.
(71) Makarov, N. S.; Guo, S.; Isaienko, O.; Liu, W.; Robel, I.; Klimov, V. I. *Nano Lett.* **2016**, *16*,

2349.
(72) Huang, H.; Susha, A. S.; Kershaw, S. V.; Hung, T. F.; Rogach, A. L. *Adv. Sci.* **2015**, *2*, 1500194.
(73) Klimov, V. I. *Annu. Rev. Phys. Chem.* **2007**, *58*, 635.
(74) Efros, A. L.; Rosen, M.; Kuno, M.; Nirmal, M.; Norris, D. J.; Bawendi, M. *Phys. Rev. B* **1996**, *54*, 4843.
(75) Klimov, V. I.; Baker, T. A.; Lim, J.; Velizhanin, K. A.; McDaniel, H. *ACS Photonics* **2016**, *3*, 1138.
(76) El Mouedden, Y.; Ding, B.; Song, Q.; Li, G.; Alameh, K. *IEEE J. Sel. Top. Quant.* **2016**, *22*, 82.
(77) Coropceanu, I.; Bawendi, M. G. *Nano Lett.* **2014**, *14*, 4097.
(78) Maculan, G.; Sheikh, A. D.; Abdelhady, A. L.; Saidaminov, M. I.; Haque, M. A.; Banavoth, M.; Alarousu, E.; Mohammed, O. F.; Wu, T.; Bakr, O. M. *J. Phys. Chem. Lett.* **2015**, *6*, 3781.
(79) Yoon, S. J.; Draguta, S.; Manser, J. S.; Sharia, O.; Schneider, W. F.; Kuno, M.; Kamat, P. V. *ACS Energy Lett.* **2016**, *1*, 290.
(80) Park, S. H.; Roy, A.; Beaupré, S.; Cho, S.; Coates, N.; Moon, J. S.; Moses, D.; Leclerc, M.; Lee, K.; Heeger, A. J. *Nat. Photonics* **2009**, *3*, 297.
(81) Tummeltshammer, C.; Taylor, A.; Kenyon, A.; Papakonstantinou, I. *Sol. Energy Mater. Sol. Cells* **2016**, *144*, 40.
(82) Nikolaidou, K.; Sarang, S.; Hoffman, C.; Mendewala, B.; Ishihara, H.; Lu, J. Q.; Ilan, B.; Tung, V.; Ghosh, S. *Adv. Opt. Mater.* **2016**, *4*, 2126.
(83) Mirershadi, S.; Ahmadi-Kandjani, S. *Dyes Pigments* **2015**, *120*, 15.
(84) Roncali, J.; Garnier, F. *Appl. Opt.* **1984**, *23*, 2809.
(85) Batchelder, J.; Zewai, A.; Cole, T. *Appl. Opt.* **1979**, *18*, 3090.
(86) Leijtens, T.; Eperon, G. E.; Noel, N. K.; Habisreutinger, S. N.; Petrozza, A.; Snaith, H. J. *Adv. Energy Mater.* **2015**, *5*, 1500963.
(87) Leng, M.; Chen, Z.; Yang, Y.; Li, Z.; Zeng, K.; Li, K.; Niu, G.; He, Y.; Zhou, Q.; Tang, J. *Angew. Chem. Int. Ed.* **2016**, *55*, 15012.
(88) Jellicoe, T. C.; Richter, J. M.; Glass, H. F.; Tabachnyk, M.; Brady, R.; Dutton, S. E.; Rao, A.; Friend, R. H.; Credgington, D.; Greenham, N. C.; Böhm, M. L. *J. Am. Chem. Soc.* **2016**, *138*, 2941.
(89) Inman, R.; Shcherbatyuk, G.; Medvedko, D.; Gopinathan, A.; Ghosh, S. *Opt. Express* **2011**, *19*, 24308.
(90) Krumer, Z.; Pera, S. J.; van Dijk-Moes, R. J.; Zhao, Y.; de Brouwer, A. F.; Groeneveld, E.; van Sark, W. G.; Schropp, R. E.; de Mello Donegá, C. *Sol. Energy Mater. Sol. Cells* **2013**, *111*, 57.
(91) Zhao, Y.; Lunt, R. R. *Adv. Energy Mater.* **2013**, *3*, 1143.
(92) Giebink, N. C.; Wiederrecht, G. P.; Wasielewski, M. R. *Nat. Photonics* **2011**, *5*, 694.
(93) Brovelli, S.; Schaller, R. D.; Crooker, S.; García-Santamaría, F.; Chen, Y.; Viswanatha, R.; Hollingsworth, J. A.; Htoon, H.; Klimov, V. I. *Nat. Commun.* **2011**, *2*, 280.
(94) Zhao, Y.; Meek, G. A.; Levine, B. G.; Lunt, R. R. *Adv. Opt. Mater.* **2014**, *2*, 606.
(95) Shcherbatyuk, G.; Inman, R.; Wang, C.; Winston, R.; Ghosh, S. *Appl. Phys. Lett.* **2010**, *96*, 191901.
(96) Aeberhard, U.; Vaxenburg, R.; Lifshitz, E.; Tomić, S. *Phys. Chem. Chem. Phys.* **2012**, *14*, 16223.
(97) Koberling, F.; Mews, A.; Basché, T. *Adv. Mater.* **2001**, *13*, 672.
(98) Pietryga, J. M.; Werder, D. J.; Williams, D. J.; Casson, J. L.; Schaller, R. D.; Klimov, V. I.; Hollingsworth, J. A. *J. Am. Chem. Soc.* **2008**, *130*, 4879.
(99) Zhao, H.; Chaker, M.; Wu, N.; Ma, D. *J. Mater. Chem.* **2011**, *21*, 8898.
(100) Zhang, T.; Zhao, H.; Riabinina, D.; Chaker, M.; Ma, D. *J. Phys. Chem. C* **2010**, *114*, 10153.
(101) Zhao, H.; Chaker, M.; Ma, D. *J. Mater. Chem.* **2011**, *21*, 17483.
(102) Haus, J. W.; Zhou, H.; Honma, I.; Komiyama, H. *Phys. Rev. B* **1993**, *47*, 1359.
(103) Zhao, H.; Fan, Z.; Liang, H.; Selopal, G.; Gonfa, B.; Jin, L.; Soudi, A.; Cui, D.; Enrichi, F.; Natile, M. *Nanoscale* **2014**, *6*, 7004.
(104) Zhao, H.; Liang, H.; Vidal, F. o.; Rosei, F.; Vomiero, A.; Ma, D. *J. Phys. Chem. C* **2014**, *118*, 20585.
(105) De Geyter, B.; Justo, J.; Moreels, I.; Lambert, K.; Smet, P. F.; Van Thourhout, D.; Houtepen, A.

J.; Grodzinska, D.; de Mello Donega, C.; Meijerink, A.; Vanmaekelbergh, D.; Hens, Z. *ACS Nano* **2011**, *5*, 58.

(106) Wang, L.; Wang, H.-Y.; Gao, B.-R.; Pan, L.-Y.; Jiang, Y.; Chen, Q.-D.; Han, W.; Sun, H.-B. *IEEE J. Quantum Elect.* **2011**, *47*, 1177.

(107) Hyun, B.-R.; Bartnik, A.; Lee, J.-K.; Imoto, H.; Sun, L.; Choi, J. J.; Chujo, Y.; Hanrath, T.; Ober, C. K.; Wise, F. *Nano Lett.* **2009**, *10*, 318.

(108) Ushakova, E. V.; Litvin, A. P.; Parfenov, P. S.; Fedorov, A. V.; Artemyev, M.; Prudnikau, A. V.; Rukhlenko, I. D.; Baranov, A. V. *ACS Nano* **2012**, *6*, 8913.

(109) Olson, R.; Loring, R. F.; Fayer, M. *Appl. Opt.* **1981**, *20*, 2934.

(110) Bronstein, N. D.; Li, L.; Xu, L.; Yao, Y.; Ferry, V. E.; Alivisatos, A. P.; Nuzzo, R. G. *ACS Nano* **2013**, *8*, 44.

(111) Wu, F.; Zhang, J.; Kho, R.; Mehra, R. *Chem. Phys. Lett.* **2000**, *330*, 237.

(112) Erickson, C. S.; Bradshaw, L. R.; McDowall, S.; Gilbertson, J. D.; Gamelin, D. R.; Patrick, D. L. *ACS Nano* **2014**, *8*, 3461.

(113) Nepal, D.; Drummy, L. F.; Biswas, S.; Park, K.; Vaia, R. A. *ACS Nano* **2013**, *7*, 9064.

(114) Hardman, R. *Environ. Health Perspect.* **2006**, *114*, 165.

(115) Bourlinos, A. B.; Stassinopoulos, A.; Anglos, D.; Zboril, R.; Karakassides, M.; Giannelis, E. P. *Small* **2008**, *4*, 455.

(116) Bourlinos, A. B.; Stassinopoulos, A.; Anglos, D.; Zboril, R.; Georgakilas, V.; Giannelis, E. P. *Chem. Mater.* **2008**, *20*, 4539.

(117) Xu, X.; Ray, R.; Gu, Y.; Ploehn, H. J.; Gearheart, L.; Raker, K.; Scrivens, W. A. *J. Am. Chem. Soc.* **2004**, *126*, 12736.

(118) Sun, Y.-P.; Zhou, B.; Lin, Y.; Wang, W.; Fernando, K. S.; Pathak, P.; Meziani, M. J.; Harruff, B. A.; Wang, X.; Wang, H. *J. Am. Chem. Soc.* **2006**, *128*, 7756.

(119) Baker, S. N.; Baker, G. A. *Angew. Chem. Int. Ed.* **2010**, *49*, 6726.

(120) Wang, J.; Zhang, P.; Huang, C.; Liu, G.; Leung, K. C.-F.; Wáng, Y. X. n. J. *Langmuir* **2015**, *31*, 8063.

(121) Zhang, Y.-Q.; Ma, D.-K.; Zhuang, Y.; Zhang, X.; Chen, W.; Hong, L.-L.; Yan, Q.-X.; Yu, K.; Huang, S.-M. *J. Mater. Chem.* **2012**, *22*, 16714.

(122) Zhu, S.; Zhang, J.; Qiao, C.; Tang, S.; Li, Y.; Yuan, W.; Li, B.; Tian, L.; Liu, F.; Hu, R. *Chem. Commun.* **2011**, *47*, 6858.

(123) Li, Y.; Hu, Y.; Zhao, Y.; Shi, G.; Deng, L.; Hou, Y.; Qu, L. *Adv. Mater.* **2011**, *23*, 776.

(124) Ray, S.; Saha, A.; Jana, N. R.; Sarkar, R. *J. Phys. Chem. C* **2009**, *113*, 18546.

(125) Cao, L.; Wang, X.; Meziani, M. J.; Lu, F.; Wang, H.; Luo, P. G.; Lin, Y.; Harruff, B. A.; Veca, L. M.; Murray, D. *J. Am. Chem. Soc.* **2007**, *129*, 11318.

(126) Qu, S.; Zhou, D.; Li, D.; Ji, W.; Jing, P.; Han, D.; Liu, L.; Zeng, H.; Shen, D. *Adv. Mater.* **2016**, *28*, 3516.

(127) Kwon, W.; Lee, G.; Do, S.; Joo, T.; Rhee, S. W. *Small* **2014**, *10*, 506.

(128) Ding, H.; Yu, S.-B.; Wei, J.-S.; Xiong, H.-M. *ACS Nano* **2016**, *10*, 484.

(129) Wang, F.; Pang, S.; Wang, L.; Li, Q.; Kreiter, M.; Liu, C.-y. *Chem. Mater.* **2010**, *22*, 4528.

(130) Li, Y.; Miao, P.; Zhou, W.; Gong, X.; Zhao, X. *J. Mater. Chem. A* **2017**, *5*, 21452.

(131) Zhu, S.; Meng, Q.; Wang, L.; Zhang, J.; Song, Y.; Jin, H.; Zhang, K.; Sun, H.; Wang, H.; Yang, B. *Angew. Chem. Int. Ed.* **2013**, *125*, 4045.

(132) Selopal, G. S.; Zhao, H.; Tong, X.; Benetti, D.; Navarro-Pardo, F.; Zhou, Y.; Barba, D.; Vidal, F.; Wang, Z. M.; Rosei, F. *Adv. Funct. Mater.* **2017**, *27*, 1701468.

(133) Bouet, C.; Laufer, D.; Mahler, B.; Nadal, B.; Heuclin, H.; Pedetti, S.; Patriarche, G.; Dubertret, B. *Chem. Mater.* **2014**, *26*, 3002.

(134) Schliehe, C.; Juarez, B. H.; Pelletier, M.; Jander, S.; Greshnykh, D.; Nagel, M.; Meyer, A.; Foerster, S.; Kornowski, A.; Klinke, C. *Science* **2010**, *329*, 550.

(135) Li, L.; Chen, Z.; Hu, Y.; Wang, X.; Zhang, T.; Chen, W.; Wang, Q. *J. Am. Chem. Soc.* **2013**, *135*, 1213.

(136) Maiti, P. S.; Houben, L.; Bar-Sadan, M. *J. Phys. Chem. C* **2015**, *119*, 10734.

(137) Pedetti, S.; Ithurria, S.; Heuclin, H.; Patriarche, G.; Dubertret, B. *J. Am. Chem. Soc.* **2014**, *136*, 16430.

(138) Li, Z.; Peng, X. *J. Am. Chem. Soc.* **2011**, *133*, 6578.
(139) Olutas, M.; Guzelturk, B.; Kelestemur, Y.; Yeltik, A.; Delikanli, S.; Demir, H. V. *ACS Nano* **2015**, *9*, 5041.
(140) Ellingson, R. J.; Beard, M. C.; Johnson, J. C.; Yu, P.; Micic, O. I.; Nozik, A. J.; Shabaev, A.; Efros, A. L. *Nano Lett.* **2005**, *5*, 865.
(141) Aerts, M.; Bielewicz, T.; Klinke, C.; Grozema, F. C.; Houtepen, A. J.; Schins, J. M.; Siebbeles, L. D. *Nat. Commun.* **2014**, *5*, 3789.
(142) Chen, B.; Chang, S.; Li, D.; Chen, L.; Wang, Y.; Chen, T.; Zou, B.; Zhong, H.; Rogach, A. L. *Chem. Mater.* **2015**, *27*, 5949.
(143) Sichert, J. A.; Tong, Y.; Mutz, N.; Vollmer, M.; Fischer, S.; Milowska, K. Z.; García Cortadella, R.; Nickel, B.; Cardenas-Daw, C.; Stolarczyk, J. K. *Nano Lett.* **2015**, *15*, 6521.
(144) Wang, L.; Xia, L.; Wu, Y.; Tian, Y. *ACS Sustain. Chem. Eng.* **2016**, *4*, 2606.
(145) Sang, Y.; Zhao, Z.; Zhao, M.; Hao, P.; Leng, Y.; Liu, H. *Adv. Mater.* **2015**, *27*, 363.
(146) Fan, F.; Kanjanaboos, P.; Saravanapavanantham, M.; Beauregard, E.; Ingram, G.; Yassitepe, E.; Adachi, M. M.; Voznyy, O.; Johnston, A. K.; Walters, G. *Nano Lett.* **2015**, *15*, 4611.
(147) Ithurria, S.; Dubertret, B. *J. Am. Chem. Soc.* **2008**, *130*, 16504.
(148) Ithurria, S.; Tessier, M.; Mahler, B.; Lobo, R.; Dubertret, B.; Efros, A. L. *Nat. Mater.* **2011**, *10*, 936.
(149) Wang, F.; Wang, Y.; Liu, Y.-H.; Morrison, P. J.; Loomis, R. A.; Buhro, W. E. *Acc. Chem. Res.* **2014**, *48*, 13.
(150) Zhang, H.; Savitzky, B. H.; Yang, J.; Newman, J. T.; Perez, K. A.; Hyun, B.-R.; Kourkoutis, L. F.; Hanrath, T.; Wise, F. W. *Chem. Mater.* **2015**, *28*, 127.
(151) De Trizio, L.; Manna, L. *Chem. Rev.* **2016**, *116*, 10852.
(152) Chen, D.; Gao, L.; Yasumori, A.; Kuroda, K.; Sugahara, Y. *Small* **2008**, *4*, 1813.
(153) Qiu, Y.; Chen, W.; Yang, S. *J. Mater. Chem.* **2010**, *20*, 1001.
(154) Jin, L.; AlOtaibi, B.; Benetti, D.; Li, S.; Zhao, H.; Mi, Z.; Vomiero, A.; Rosei, F. *Adv. Sci.* **2016**, *3*, 1500345.
(155) Tong, H.; Zhu, Y. J.; Yang, L. X.; Li, L.; Zhang, L. *Angew. Chem. Int. Ed.* **2006**, *118*, 7903.
(156) Oh, N.; Shim, M. *J. Am. Chem. Soc.* **2016**, *138*, 10444.
(157) Wei, S.-H.; Zunger, A. *Phys. Rev. B* **1997**, *55*, 13605.
(158) Nanda, K.; Kruis, F.; Fissan, H.; Behera, S. *J. Appl. Phys.* **2004**, *95*, 5035.
(159) Martinez, G.; Schlüter, M.; Cohen, M. L. *Phys. Rev. B* **1975**, *11*, 651.
(160) Hyun, B.-R.; Zhong, Y.-W.; Bartnik, A. C.; Sun, L.; Abruña, H. D.; Wise, F. W.; Goodreau, J. D.; Matthews, J. R.; Leslie, T. M.; Borrelli, N. F. *ACS Nano* **2008**, *2*, 2206.
(161) Segets, D.; Lucas, J. M.; Klupp Taylor, R. N.; Scheele, M.; Zheng, H.; Alivisatos, A. P.; Peukert, W. *ACS Nano* **2012**, *6*, 9021.
(162) Moreels, I.; Lambert, K.; Smeets, D.; De Muynck, D.; Nollet, T.; Martins, J. C.; Vanhaecke, F.; Vantomme, A.; Delerue, C.; Allan, G. *ACS Nano* **2009**, *3*, 3023.
(163) Li, H.; Zhitomirsky, D.; Grossman, J. C. *Chem. Mater.* **2016**, *28*, 1888.
(164) Bhandari, G. B.; Subedi, K.; He, Y.; Jiang, Z.; Leopold, M.; Reilly, N.; Lu, H. P.; Zayak, A. T.; Sun, L. *Chem. Mater.* **2014**, *26*, 5433.
(165) Klimov, V. I. *J. Phys. Chem. B* **2000**, *104*, 6112.
(166) Klimov, V.; Hunsche, S.; Kurz, H. *Phys. Rev. B* **1994**, *50*, 8110.
(167) Gdor, I.; Sachs, H.; Roitblat, A.; Strasfeld, D. B.; Bawendi, M. G.; Ruhman, S. *ACS Nano* **2012**, *6*, 3269.
(168) Gaponenko, M. S.; Tolstik, N. A.; Lutich, A. A.; Onushchenko, A. A.; Yumashev, K. V. *Physica E* **2013**, *53*, 63.
(169) Warner, J. H.; Thomsen, E.; Watt, A. R.; Heckenberg, N. R.; Rubinsztein-Dunlop, H. *Nanotechnology* **2004**, *16*, 175.
(170) Fernée, M. J.; Thomsen, E.; Jensen, P.; Rubinsztein-Dunlop, H. *Nanotechnology* **2006**, *17*, 956.
(171) Stewart, J. T.; Padilha, L. A.; Qazilbash, M. M.; Pietryga, J. M.; Midgett, A. G.; Luther, J. M.; Beard, M. C.; Nozik, A. J.; Klimov, V. I. *Nano Lett.* **2012**, *12*, 622.
(172) Klimov, V. I.; Mikhailovsky, A. A.; McBranch, D.; Leatherdale, C. A.; Bawendi, M. G. *Science*

2000, *287*, 1011.

(173) Zhao, H.; Jin, L.; Zhou, Y.; Bandar, A.; Fan, Z.; Govorov, A. O.; Mi, Z.; Sun, S.; Rosei, F.; Vomiero, A. *Nanotechnology* **2016**, *27*, 495405.

(174) Qiu, Y.; Leung, S.-F.; Zhang, Q.; Hua, B.; Lin, Q.; Wei, Z.; Tsui, K.-H.; Zhang, Y.; Yang, S.; Fan, Z. *Nano Lett.* **2014**, *14*, 2123.

(175) Luo, J.; Steier, L.; Son, M.-K.; Schreier, M.; Mayer, M. T.; Grätzel, M. *Nano Lett.* **2016**, *16*, 1848.

(176) Jing, L. H.; Kershaw, S. V.; Li, Y. L.; Huang, X.; Li, Y. Y.; Rogach, A. L.; Gao, M. Y. *Chem. Rev.* **2016**, *116*, 10623.

(177) Liang, H. Y.; Zhao, H. G.; Rossouw, D.; Wang, W. Z.; Xu, H. X.; Botton, G. A.; Ma, D. L. *Chem. Mater.* **2012**, *24*, 2339.

(178) Liang, H. Y.; Rossouw, D.; Zhao, H. G.; Cushing, S. K.; Shi, H. L.; Korinek, A.; Xu, H. X.; Rosei, F.; Wang, W. Z.; Wu, N. Q.; Botton, G. A.; Ma, D. L. *J. Am. Chem. Soc.* **2013**, *135*, 9616.

(179) Liang, H. Y.; Zhao, H. G.; Li, Z. P.; Harnagea, C.; Ma, D. L. *Nanoscale* **2016**, *8*, 4882.

Résumé:

L’introduction

La génération de l'énergie directe ou indirecte à partir de ressources durables, comme le rayonnement solaire, offre un moyen pratique pour suffire à la demande croissante en énergie propre et renouvelable avec les impacts environnementaux minimisés à cause des émissions excessives de carbone.[1,2] L’étude des cellules solaires avec le rendement de conversion de puissance (en anglais: PCE) plus élevé et le faible coût a fourni des efforts de recherche en nouveaux matériaux avec l’accommodation spectrale optimale au rayonnement solaire.[13-16] Les cellules solaires à base de silicium monocristallin ont été utilisées dans les dernières décennies grâce à leur large spectre d'absorption de la lumière (300-1100 nm) correspondant bien au spectre du soleil et leurs propriétés électroniques.[12] Les cellules solaires en silicium cristallin et en simple-jonction présentent un PCE d’environ de 20% avec une très bonne stabilité et seulement une réduction en PCE de 10% pendant les prochains 30 ans dans l’utilisation de plein air.[15] Toutefois, le prix du module photovoltaïque (PV) en silicium (entièrement installé) est relativement élevé (jusqu'à 1,0 $/watt). Les cellules solaires excitoniques (en anglais : ESCs) avec le faible coût et pouvant être traitées par solution étaient émergentes pendant ces dernières années. Par exemple, des dispositifs PVs en polymère, en colorant,[13-16] en points quantiques (ou boîtes quantiques, en anglais: QDs), et en pérovskite.[17-20]

Au présent, le PCE dans tous les ESCs, à l'exception des PVs des pérovskites, est plutôt bas comparé à celui des cellules solaires commerciales au silicium. Bien que les cellules solaires à pérovskite aient récemment atteint un PCE élevé en plus de 20%, leur stabilité se ressemble très faible. Une chute rapide du PCE pendant l'utilisation était trouvée en raison de l'instabilité inhérente en structure cristalline et la sensibilité à l’humidité.

Un moyen complémentaire prometteur sur les systèmes PVs conventionnels vise des concentrateurs solaires luminescents (en anglais : LSCs) qui ont été récemment étudiés.[22-25] Un LSC typiquement comprend un guide d'ondes optique revêtu ou incorporé avec les fluorophores émissifs.[26,28] Avec l'absorption de la lumière solaire, les fluorophores réémettent des photons et ces photons sont guidés par une réflexion interne totale vers les dispositifs PVs sur leurs bords.[48-50] A cause de la surface de la dalle sous lumière est exposée beaucoup plus large que la surface de ses bords, les LSCs peuvent efficacement améliorer l'intensité des photons sur les bords où les cellules PVs sont installées, donnant un renforcement de leurs photocourants.[22,23] LSCs peuvent également s'adapter aux besoins des architectes pour des cellules PVs intégrées au bâtiment et semi-transparentes (en anglais: BIPVs), tels qu'une variété des couleurs, des formes, des transparences, de légèreté et de flexibilité, ce qui fait une option intéressante pour des bâtiments transformés ou transformer des objets communs en générateurs d'électricité transparents ou semi-transparents.[22,48,51,62]

À ce jour, les plusieurs types de fluorophores ont été utilisés comme les convertisseurs de lumière pour les LSCs, y compris les fluorophores à conversion descendante et à conversion ascendante.[22,46] Sous illumination, les fluorophores à conversion descendante, par exemple, les polymères, les colorants et les QDs, réémettent des photons à l'énergie plus faible (ex. à une longueur d'onde plus grande).[22,89] Par contre, des matériaux à conversion ascendante absorbent deux ou plus des photons, et ensuite rémittents seulement un type de photons à l'énergie plus élevée (ex. à une longueur d'onde plus courts).[40,47,48] Typiquement, les colorants et polymères présentent une couverture limitée du spectre solaire et souffrent de pertes optiques significatives associées à la réabsorption de la photoluminescence (PL) guidée. De plus, leur faible stabilité est toujours un grand défi à cause de la dégradation structurelle photo-induite des colorants/polymères,

par rapport au PCE stable pendant l'utilisation au long-terme des dispositifs. Les matériaux à conversion ascendante peuvent convertir la lumière proche infrarouge (en anglais: NIR) en lumière visible (Vis) et ultraviolette (UV), ce qui offre l'opportunité de récolter la partie de NIR du spectre solaire, mais leur rendement quantique PL (en anglais: QY, Φ_{PL}) est généralement faible (moins de 10%) et leurs spectres d'absorption sont assez étroits avec les faibles coefficients d'absorption (plusieurs ordres inférieurs par rapport aux colorants et aux QDs).[112] Ces inconvénients réduisent grandement le rendement de la récolte de la lumière des LSCs basés sur des semi-conducteurs à conversion ascendante, et ainsi limitant les utilisations commerciales.

Les QDs semi-conducteurs colloïdaux peuvent surmonter ces limitations.[40] Les QDs sont des nanocristaux (NCs) fluorescents en dimensions nanométriques (nm), normalement inférieures à 20 nm de diamètre.[40] Typiquement, ils sont composés d'un noyau inorganique, avec les quelques centaines à plusieurs milliers d'atomes, entourée par une couche organique externe des molécules surfactants, ex. oleylamine (OLA).[73,99-101] Les QDs sont très bons candidats pour les LSCs car ils ont des plusieurs avantages présentés ci-dessous: i) Une synthèse simple par la voie chimique humide; ii) Un QY très élevé (jusqu'à 100%); iii) Un large spectre d'absorption (300−2000 nm); iv) Une grande absorption aux sections transversales; v) Des spectres d'absorption/émission modifiés par la taille; et vi) La meilleure stabilité chimique/photo- comparée aux colorants/polymères organiques.[73, 99-101] Dans les LSCs, comment éviter la perte d'énergie en raison de la réabsorption est une clé pour réaliser leur haute efficacité. Idéalement, si un QY de QDs atteint la valeur de 100%, il n'y aurait presque aucune perte d'énergie par réabsorption et la perte d'énergie dépendrait principalement de l'angle critique θ_C car les photons réémis peuvent encore s'échapper du LSC. Dans la pratique, le QY de QDs colloïdaux est généralement inférieur à 100% et il existe également un chevauchement spectral entre leur absorption et leur émission.

Les pertes d'énergie à la réabsorption de QDs se produisent de façon répétitive, car ces photons peuvent être absorbés et réémis plusieurs fois par d'autres QDs avec des bandes interdites (E_g) similaires avant d'atteindre un bord.[23] Dans les implémentations pratiques des LSCs, les longueurs de chemin optique peuvent d'avoir un mètre ou plus, et même un très petit chevauchement entre les spectres d'absorption et d'émission peut causer des fortes pertes d'énergie.[33] Ainsi, la synthèse de QDs avec un QY élevé et un grand décalage de Stokes (définie par la différence entre les positions de la bande maximale d'absorption et d'émission) deviennent l'un des facteurs les plus critiques dans la fabrication de LSCs au grand rendement avec la grande surface.[33] Les QDs peuvent être conçus pour fournir un grand décalage de Stokes, ce qui est important sur la réalisation de LSCs à la grande échelle avec des pertes de réabsorption supprimées. Donc, les QDs représentent des candidats prometteurs pour les LSCs avec le coût faible, le rendement élevé et la stabilité au long-terme.[32,33]

En plus d'utiliser des nanocristaux semi-conducteurs pour les LSCs, ils peuvent également utiliser comme les absorbeurs et les sensibilisateurs pour dispositif photoélectrochimique (PEC) pour la production d'H_2 à l'énergie solaire.[36] Les sources d'énergie chimique propre, c'est-à-dire hydrogène peuvent d'être stockée et transportée pour des usages appropriés. Typiquement, dans un système électrochimique, les nanocristaux semiconducteurs agissent comme sensibilisateur et catalyseur, où la charge se sépare et se transfère en photoanode et photocathode pour des réactions de génération d'oxygène et d'hydrogène, respectivement.[36] Les oxydes métalliques comme ZnO et TiO_2 sont extensive étudiés comme photoélectrode pour génération d'hydrogène. Cependant, les matériaux optimisés avec la bande interdite appropriée (ex. transitions *d-d* interdites) pour la production d'hydrogène par l'énergie solaire ont un très faible coefficient d'absorption optique.

D'autre part, les mobilités des porteurs dans les oxydes métalliques sont assez faibles, ce

qui cause des longueurs de diffusion du porteur courtes. Maintenant, le rendement à conversion du solaire en hydrogène (en anglais: STH) dans les cellules PECs est encore faible, ce qui nécessite d'être encore amélioré. Pour obtenir une stabilité à long-terme (la performance PEC en fonction du temps) des photoélectrodes et réduire leur coût, il est également très difficile de les réaliser dans la pratique. Les nanoplaques (NPLs) ultraminces avec un spectre d'absorption large, des mobilités de porteurs élevées, sont favorables à l'application d'une génération solaire-à-hydrogène avec le rendement élevé.

Les objectifs

Comme l'introduction des LSCs ci-dessus, il est assez difficile de fabriquer des LSCs basés sur des QDs avec une grande surface, efficaces, stables et environnementaux. Plus précisément, le design et la synthèse d'un émetteur efficace sont importants pour l'application des LSCs. Un émetteur efficace nécessite les caractéristiques suivantes: (1) un QY relativement élevé; (2) un large spectre d'absorption correspondant au rayonnement solaire; (3) un chevauchement faible ou nul entre les spectres d'absorption et d'émission; (4) des matériaux sans métaux lourds; (5) la stabilité au long-terme dans la matrice polymère sous éclairage et condition ambiante; (6) une méthode de synthèse simple et verte.

Pour résoudre les soucis ci-dessus, je compte de synthétiser des émetteurs PL efficaces (semi-conducteurs) pour les LSCs, et de fabriquer des LSCs avec une grande surface à base de QDs préparés.

1. De synthétiser un émetteur QY (ex. QDs pérovskites) avec un décalage de Stokes adapté, et les caractériser.

2. De synthétiser les QDs de PbS/CdS à NIR avec un grand décalage de Stokes pour la fabrication des LSCs, et les caractériser.

3. D'utiliser des QDs de carbone verts (C-points) pour la fabrication de LSCs par une méthode simple, et les caractériser.

Pendant ce temps, la synthèse de NPLs ultraminces avec un large spectre d'absorption est également exigeante pour l'application de génération d'hydrogène, améliorant le rendement et la stabilité du solaire-à-hydrogène.

On compte de synthétiser des NPLs ultraminces avec un large spectre d'absorption pour la production d'hydrogène par l'énergie solaire. Les objectifs sur ces projets sont par les suivants:

1. Synthèse de NPLs ultra-minces à NIR et l'utilisation pour la fabrication de photoanodes sur la génération d'hydrogène à l'énergie solaire.

Ce mémoire de la thèse comprend des six parties et bien organisé par la suite. Le chapitre 1 présente le sujet de cette thèse et décrit la motivation de ce travail. Le chapitre 2 présente la synthèse et la caractérisation de QDs CsPb $(Br_xI_{1-x})_3$ aux pérovskites à halogénures mixtes avec le QY élevé et le décalage de Stokes adaptés par rapport de concentration des précurseurs Br/I variables, et étudient les performances optiques (le rendement optique, le rendement quantique et la stabilité) des LSCs. Le chapitre 3 montre la synthèse et la caractérisation de QDs de PbS / CdS en noyau/coquille avec un décalage de Stokes en ajustant la taille du noyau et l'épaisseur de la coque, et discutent la performance d'optique {le rendement optique externe (η_{opt}), le rendement quantique ($\eta_{quantum}$) et la stabilité} des LSCs basées sur les QDs PbS/CdS en noyau/coquille.[62] Le chapitre 4 manifeste la synthèse de la fabrication de C-points non-toxique et à faible coût par une méthode simple en utilisant une charge à base de carbone relativement abondante en terre. De plus,

on étudie les propriétés optiques des C-points modifiés en surface et les performances optiques des LSCs à base de C-points à grande surface.[63] Le chapitre 5 présente la synthèse des NPLs de $PbSe_{1-x}S_x$ ultraminces à NIR par l'échange de cations en utilisant des NPLs de $CdSe_{1-x}S_x$, et ensuite on démontre le mécanisme de formation possible et les propriétés optiques des NPLs de $PbSe_{1-x}S_x$. Enfin, on étudie la performance de la photoanode basée sur NPLs de $PbSe_{1-x}S_x$ dans la génération d'hydrogène par l'énergie solaire.[64] Le chapitre 6 résume brièvement les contributions importantes dans ce travail et les futurs défis dans ce domaine de recherche.

Chapitre 2 La synthèse et la caractérisation de concentrateurs solaires luminescents à base des points quantiques à pérovskite

Les QDs pérovskites organiques-inorganiques et inorganiques hybrides colloïdales ont été synthétisées et utilisées comme blocs de construction dans une variété de dispositifs.[65-72] Parmi les différents types de QDs pérovskites, les QDs $CsPbX_3$ inorganiques (X = Cl, Br, I) ont été extensive étudiés pour les optoélectroniques en raison de leur taille/spectres d'absorption et d'émission dépendant de la composition, le large spectre d'absorption, la haute luminosité avec un QY jusqu'à 90% ou l'unité, le faible largeur de raie d'émission, la synthèse facile en phase de solution et la bonne photostabilité.[65,66,68,69] Les QDs pérovskites inorganiques peuvent représenter un nouveau candidat prometteur pour les LSCs efficaces (la Figure R.1).

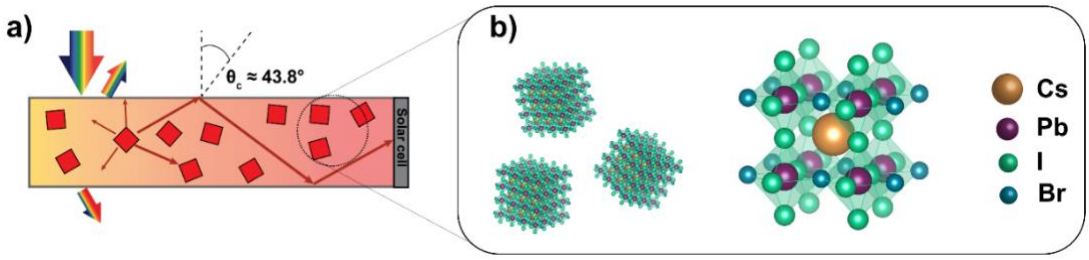

Figure R.1 (a) Le schéma d'une configuration typique d'un LSC. (b) La structure cubique de QDs pérovskites à halogénures mixtes de $CsPb(Br_xI_{1-x})_3$.

Dans la Figure R.2a, les QDs $CsPb(Br_{0.4}I_{0.6})_3$ à halogénure mixte présentent une forme cubique typique avec une taille uniforme de ~13 nm, qui est attribuée à la phase cubique. Les spectres d'absorption et d'émission de QDs pérovskites à halogénures mixtes avec des compositions différentes sont montrés dans la Figure R.2b. Le spectre d'absorption de QDs pérovskites peut être adapté sur la région UV-Visible. Avec la diminution de la concentration de Br/(Br + I), le premier pic d'absorption excitonique s'est déplacé vers le rouge, cohérent avec la tendance similaire des positions de pic de PL. Par rapport aux QDs pérovskites à halogénure pure ($CsPbBr_3$ ou $CsPbI_3$) ayant une largeur maximale à mi-hauteur (en anglais : FWHM) de ~17-20 nm, la FWHM dans les QDs pérovskites à halogénures mixtes est plus large en raison de leur plus grande distribution de taille. Le QY de QDs pérovskites variait de 20% à 90%. De plus, les QDs $CsPb(Br_xI_{1-x})_3$ pérovskites à halogénures mixtes (x = 0,1; 0,2; 0,3; 0,4) montre un décalage de Stokes en deux fois plus grand par rapport aux QDs pérovskites à halogénure pure (Figure R.2c), qui peuvent atténuer la perte d'énergie dans les LSCs en grande surface. Dans les QDs colloïdaux, un décalage de Stokes résulte typiquement d'une combinaison des effets de la division de la structure des bords de bande, de l'émission assistée par des phonons et de la polydispersité de taille.[73, 74]

D'ici, le plus grand décalage de Stokes sur les QDs à halogénures mixtes peut provenir de leur plus grande distribution de taille par rapport aux QDs pérovskites unique. Les QDs pérovskites

synthétisées ont été utilisées pour fabriquer des LSCs semi-transparents avec une grande surface ($0,2 \times 6 \times 6$ cm^3), comme le montrent les Figures R.2d-f. Sous illuminations solaires ou UV, la lumière rouge ou verte concentrée peut être clairement observée à partir des bords des LSCs basés sur des QDs pérovskites avec les différentes compositions. La dynamique des dégradations PL de QDs en solution et de la matrice polymère est presque la même (Figure R.2h), indiquant que les QYs de QDs sont constants et que des pièges ou des défauts de surface supplémentaires ne sont pas introduits durant le processus de fabrication. Les spectres d'absorption et de PL des LSCs à base de QDs pérovskites à différents trajets optiques pour les LSCs à halogénure mixte $CsPb(Br_{0.2}I_{0.8})_3$ et $CsPbBr_3$ QD sont présentés sur la Figure R.2g. Avec l'augmentation du chemin optique, les spectres PL des deux types de QDs présentent un décalage vers le rouge allant jusqu'à 8 nm avec un rétrécissement du FWHM PL, ce qui confirme que la perte d'énergie est causée par la réabsorption de la lumière. Comme le montre la Figure R.2i, la zone PL intégrée de $CsPb(Br_{0.2}I_{0.8})_3$ reste 0,5 dans 6 cm LSCs, ce qui est supérieur à 0,3 dans 6 cm LSCs basé sur $CsPbBr_3$ en raison de l'énergie de sortie de photons et de réabsorption perte.

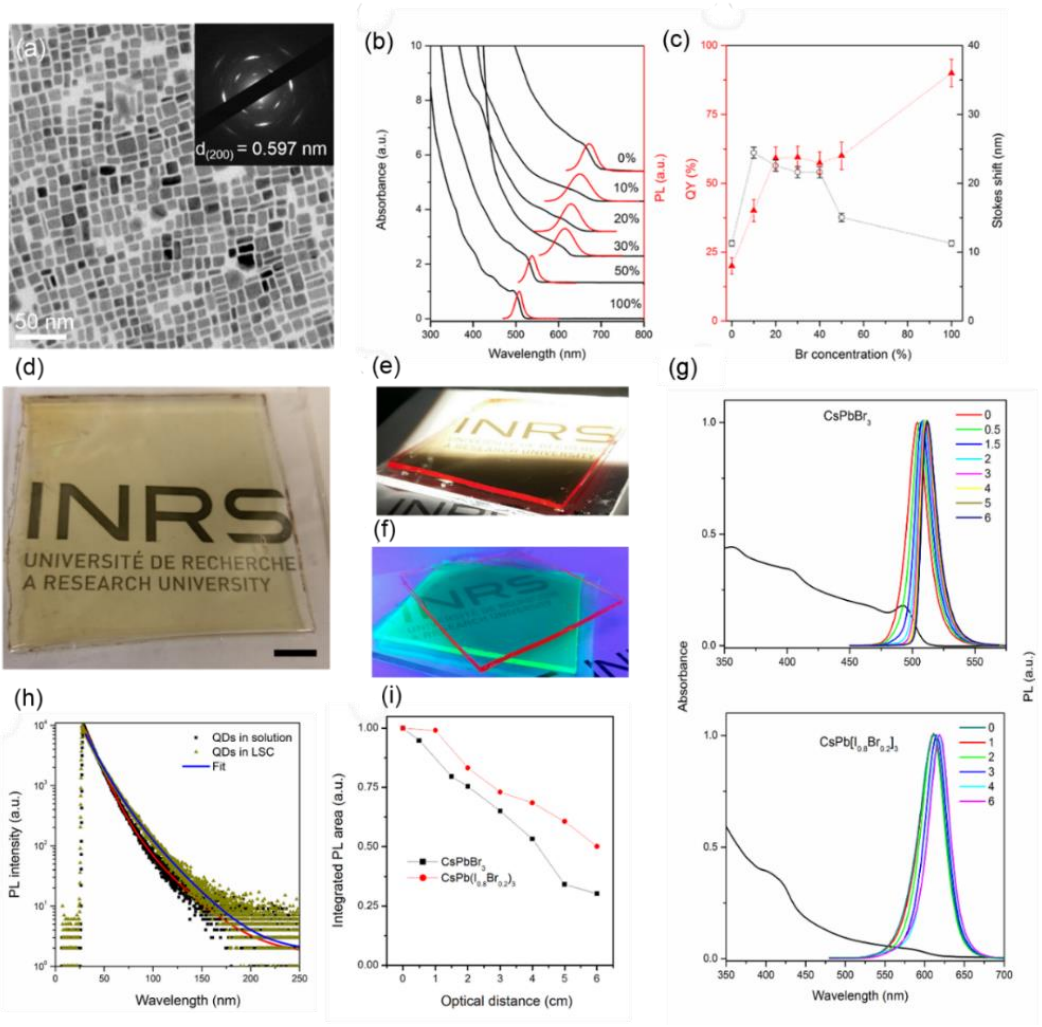

Figure R.2 (a) Une image de MEB avec une grande surface et correspondant un modèle SAED de QDs $CsPb(Br_{0.4}I_{0.6})_3$ (l'encart). (b) L'absorption et les spectres PL de QDs $CsPb(Br_xI_{1-x})_3$ avec compositions chimiques (x = 0-1) variées. (c) Le QY et le décalage de Stokes variés avec différentes concentrations de Br. Photographiques de la LSC comprenant QDs $CsPb(Br_{0.2}I_{0.8})_3$ sous la température ambiante (d), illumination d'un soleil (100 mW/cm^2) (e), et l'illumination UV (f). La barre d'échelle est de 1 cm (d). Dimensions LSC, 6 × 6 × 0,2 cm^3. (g) L'absorption et les spectres PL mesurés à différents chemins optiques pour les LSCs à base de QDs $CsPb(Br_{0.2}I_{0.8})_3$. (h) Les courbes de dégradation PL pour les QDs $CsPb(Br_{0.2}I_{0.8})_3$ dans le toluène et la matrice polymère (excitation à 440 nm). (i) La zone PL intégrée à différents chemins optiques pour les LSCs basés sur QDs $CsPbBr_3$ et $CsPb(Br_{0.2}I_{0.8})_3$.

Une méthode courante pour estimer le η_{opt} consiste à coupler une cellule PV (généralement une cellule solaire en silicium avec des paramètres PV bien connus) au bord du LSC. Dans ce cas, η_{opt} peut être calculé comme la suite:[51]

$$\eta_{\mathrm{opt}} = \frac{I_{\mathrm{LSC}} \cdot A_{\mathrm{PV}}}{I_{\mathrm{SC}} \cdot A_{\mathrm{LSC}}} = \frac{I_{\mathrm{LSC}}}{I_{\mathrm{SC}} \cdot G}$$

Lorsque I_{LSC} est le courant de court-circuit généré par la cellule couplée au LSC, I_{SC} est le courant de court-circuit de la même cellule PV sous l'éclairage direct, A_{PV} est la zone du bord du LSC (ou la zone active sur la cellule PV, si la zone est plus petite) et A_{LSC} est la zone du sommet du LSC. Les LSC semi-transparents à grande surface basés sur QDs $CsPb(Br_{0.2}I_{0.8})_3$ présentent un η_{opt} de 2% avec un facteur G de 45 (9 × 1,5 cm^2) et une stabilité à long-terme de l'air.

La publication relative à ce travail montre ci-dessous :

[61] H. Zhao[#], Y. Zhou[#], D. Benetti, D. Ma, and F. Rosei. Perovskite quantum dots integrated in large-area luminescent solar concentrators. *Nano Energy*, 37:214-223, 2017. (#: contribution égale)

Chapitre 3 La synthèse et la caractérisation des concentrateurs solaires luminescents à base de points quantiques PbS/CdS

Les QDs pérovskites à halogénures mixtes avec un QY élevé pour l'utilisation des LSCs ont été présentés dans le chapitre 2. Cependant, le décalage de Stokes de QDs pérovskites à halogénures mixtes est encore relativement faible, ce qui produit une forte réabsorption lorsque la dimension de LSC devient plus grande. De plus, l'absorption de QDs pérovskites à halogénures mixtes mentionnées est dans la gamme d'UV-Vis, ce qui n'est pas suffisant pour l'utilisation de

l'irradiation solaire. Pour prolonger l'absorption et améliorer le décalage de Stokes de l'émetteur PL pour l'utilisation des LSCs, on a synthétisé les QDs PbS/CdS en noyau/coquille avec un décalage de Stokes modifié en faisant varier la taille du noyau et l'épaisseur de la coquille.

Spécifiquement, les QDs PbS/CdS en noyau/coquille avec une taille accordable et une épaisseur de coque ont été synthétisés par une méthode d'échange de cations.[99,101] Le rayon du noyau de PbS (R) varie de 1,3 à 3,3 nm, avec une épaisseur de 0,1 ~ 0,7 nm. Les spectres d'absorption et de PL représentatifs des échantillons en solution contenant différentes tailles de QDs PbS et PbS/CdS sont montrés dans la Figure R.3a. Les deux premiers pics d'absorption et d'émission excitoniques ont été clairement observés pour ces échantillons. Pour les QDs avec R de 2,3 nm, avec une épaisseur de coquille croissante (H) de 0 à 0,7 nm, les décalages de Stokes présentent une variation limitée, par rapport aux QDs PbS nuls. Au contraire, dans les QDs en noyau/coquille avec R de 1,5 nm, le décalage de Stokes augmente significativement avec la croissance de l'épaisseur de la coquille (Figure R.3a). Les décalages de Stokes dépendants de la taille du noyau et de l'épaisseur de la coquille dans les QDs PbS ou PbS/CdS sont illustrés plus en détail dans la Figure R.3b. Le décalage de Stokes dans les QDs nuls augmente modérément avec la diminution de la taille (décalage bleu du pic PL), jusqu'à un maximum de 150 meV. Dans les QDs en noyau/coquille, pour R inférieur à 2 nm (L'énergie de pic PL > 1,0 eV) et H de 0,5 ~ 0,7 nm, les décalages de Stokes sont significativement plus grands (jusqu'à 200−250 meV) que ceux de QDs PbS et de QDs en noyau/coquille avec la coquille mince (H: 0,1 ~ 0,2 nm). [31, 78]

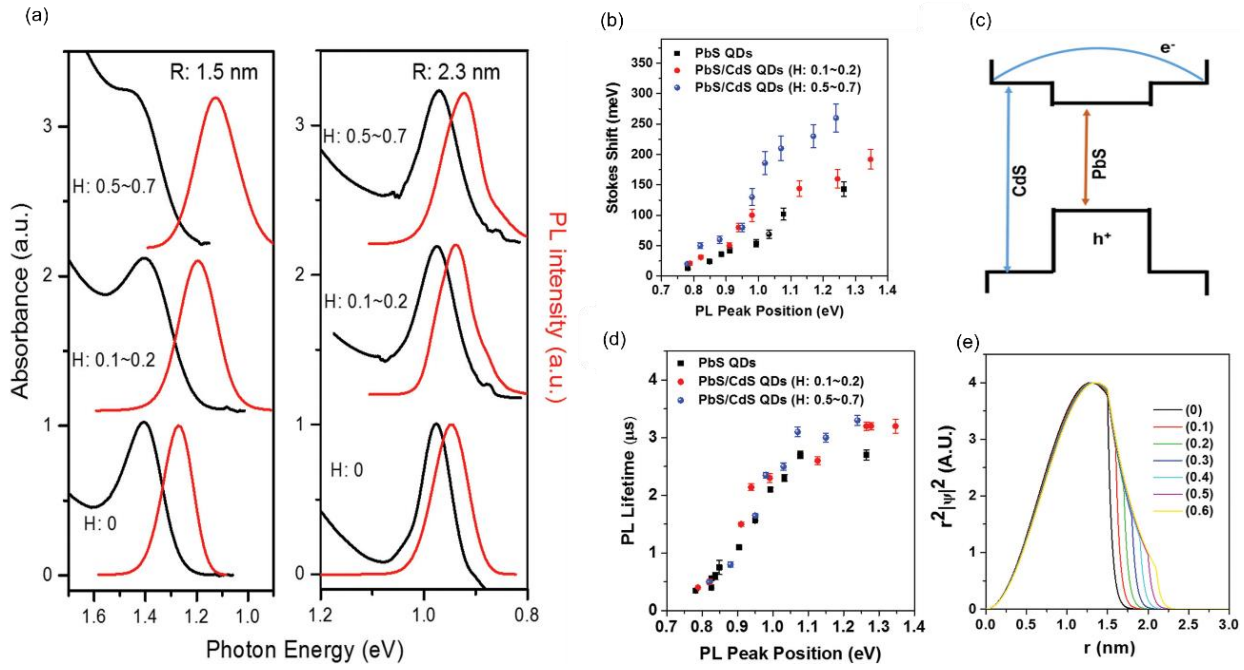

Figure R.3 (a) L'absorption normalisée et les spectres PL de QDs ayant un rayon de noyau de 1,5 et 2,3 nm avec une épaisseur de couche accordable CdS. (b) Le décalage de Stokes de QDs avec épaisseurs de coquille variée en fonction de la position de pic PL (liée à la taille de noyau de diamètre de 3 à 6 nm). (c) La structure de la bande électronique approximative d'un QD en noyau/coquille de PbS/CdS. (d) La durée de vie de PL de QDs avec différentes épaisseurs de coquille en fonction de la position du pic PL (liée à la taille du noyau de diamètre de 3 à 6 nm). (e) Des fonctions de distribution radiale pour l'électron 1S d'un QD de PbS ayant une taille de noyau de 3,0 nm de diamètre et une épaisseur de couche variée de 0-0,6 nm.

Pour comprendre les différences observées dans les décalages de Stokes, on a calculé les fonctions d'onde électronique d'un QD (R: 3 nm; H: 0~0,6 nm) en fonction de son alignement de la bande en masse (Figures R.3c, e). Dans cette calculation, la masse effective des électrons dans le PbS et le CdS en masse et la structure de la bande de CdS en masse ont été utilisées. La Figure R.3e montre les fonctions de distribution radiale des électrons 1S dans le QD en fonction de la distance radiale du centre de QD. Les électrons ont une forte probabilité de pénétrer profondément dans la couche de CdS et même d'entrer dans la couche extérieure de la surface de QD, bien que l'amplitude de leur fonction d'onde décroisse dans toute l'épaisseur de la coquille, en particulier

pour les coquilles plus épaisses. Ces résultats décrivent les décalages de Stokes dépendant de la taille et de l'épaisseur de la coquille dans les QDs en noyau/coquille, ce qui sont causés par la fuite d'électrons efficace. Généralement, cet effet de la fuite peut causer un décalage vers le rouge de la position du pic PL et une durée de vie plus longue par rapport aux QDs nuls (Figure R.3d). Les durées de vie PL de QDs PbS nuls augmentent avec la croissance de la position de pic PL, qui est corrélée avec R de QD de 0,4 μs (~0,8 eV) à 2,7 μs (~1,05 eV) et reste presque constante après ~1,05 eV. Les durées de vie des QDs en noyau/coquille avec une position de pic PL supérieure à ~0,95 eV sont plus longues que celles des QDs PbS purs. La longue durée de vie est généralement attribuée à la diminution du confinement quantique induisant par la fuite d'électrons.

De plus, les QDs en noyau/coquille synthétisés avec une épaisseur de coquille de 0,5 ~ 0,7 nm montrent toujours un QY élevé de 40-50%, ce qui fait de bons candidats pour les LSCs au rendement élevé. Pour comparer expérimentalement le rendement des LSCs, on a fabriqué en outre les LSCs (5 × 1,5 × 0,2 cm^3) en incorporant les QDs nuls et de noyau/coquille dans une matrice de polymère de poly(méthacrylate de lauryle) (PLMA). Les QDs PbS avec la grande taille et les QDs en noyau/coquille avec la petite taille sont étiquetés comme PbS_L et C@S_S, respectivement. Les formes des spectres PL pour l'échantillon C@S_S restent inchangées le long du trajet optique jusqu'à 5,0 cm, suggérant la suppression de la réabsorption au grand décalage de Stokes (Figure R.4b). Et plus, le signal PL intégré ne présente une faible atténuation (10%) à un trajet optique de 4,5 cm en raison de la diffusion, indiquant la haute performance optique du LSC basé sur QDs C@S_S. Finalement, un LSC semi-transparent à base de QDs C@S_S a été fabriqué dans une taille aussi grande que 10 × 1,5 × 0,2 cm^3 (Figure R.4e).

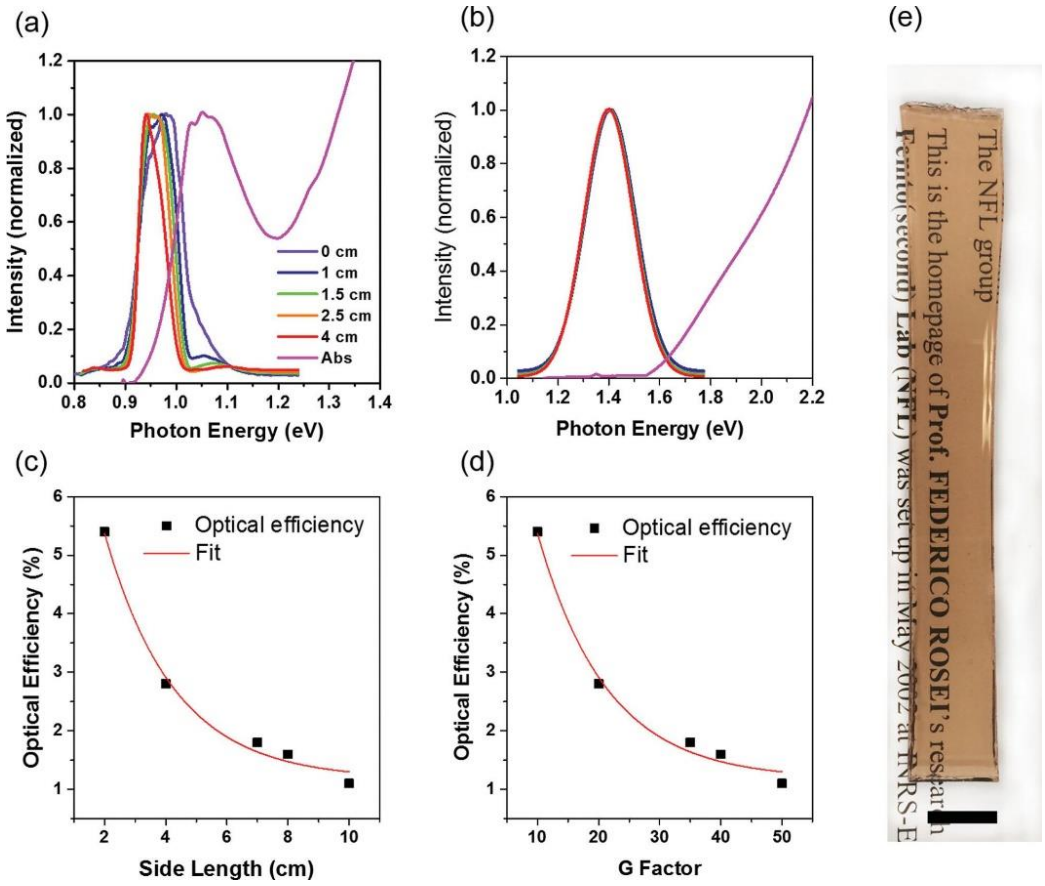

Figure R.4 L'absorption normalisée et les spectres PL mesurés avec différents trajets optiques pour les échantillons a) des QDs PbS_L et b) des QDs C@S_S. Le rendement optique externe du LSC à base de QDs C@S_S couplé à la diode Si en fonction de la longueur du côté c) ou du facteur d) G. e) La photographie d'un LSC à base de polymère de QDs (dimension: 10 × 1,5 × 0,2 cm^3) comprenant QDs C@S_S à la lumière ambiante. La barre d'échelle est de 1 cm.

Le η_{opt} présente une décroissance exponentielle avec l'augmentation de la longueur latérale ou G du LSC (Figures R.4c, d). Le η_{opt} de LSC semi-transparent de QDs C@S_S atteint jusqu'à 6,1% avec G de 10, ce qui est plus de 15 fois plus élevé que celui de LSC planaire à base de QDs PbS (G = 4,2) avec une concentration similaire de QDs (~20 μM) pour une structure plane.

La publication liée à ce travail montre ci-dessous:

[62] Y. Zhou, D. Benetti, Z. Fan, H. Zhao, D. Ma, A. Govorov, A. Vomiero, and F. Rosei. Near Infrared, Highly Efficient Luminescent Solar Concentrators. *Adv. Energy Mater.* 6:1501913, 2016.

Chapitre 4 La synthèse et la caractérisation du concentrateur solaire luminescent à base de points de carbone

Comme discuté dans les chapitres précédents, outre la question de la réabsorption, les défis principaux qui ont entravé jusqu'ici le développement technologique des LSCs sont les suivants: (1) Les QDs inorganiques couramment utilisés contient des éléments toxiques, ex. Cd, Pb. Même si CuInSe(S) et QDs silicium sont moins toxiques, la procédure de synthèse implique l'utilisation de solvants organiques toxiques.[22,48,114] (2) Les QDs dopés ou de type-II présentent une perte d'énergie de réabsorption réduite qui est favorable pour les LSCs avec la grande surface. Cependant, le QY de PL de QDs n'est généralement pas très élevé (< 20%) et souffre d'une faible photostabilité.[112] (3) Des QDs inorganiques colloïdales sont sensibles à l'exposition oxygène/humidité/lumière pendant la synthèse, la purification et la après-utilisation. Comparé aux colorants/polymères organiques et aux QDs inorganiques, ex. Si, PbS/CdS et CdSe/CdS, les pointes de carbone (les points-C) présentent une bonne stabilité de l'air, ce qui permet de les stocker dans des conditions ambiantes. En outre, l'émission non radiative peut être inhibée par la passivation de surface et la fonctionnalisation des pointes-C, ce qui produit une grande séparation d'entre les spectres d'émission et d'absorption. Ceci, à son tour, pourrait réduire la perte d'énergie causée par la réabsorption dans les LSCs avec la grande surface.[128,129] Récemment, la fabrication de LSCs à base de points-C avec une petite surface latérale (4 cm^2) a été rapportée.[130]

Les points-C de Vis-actifs (QY ≈ 30%) ont été synthétisés par la méthode solvothermale. Après le traitement de surface, les points-C hydrophiles peuvent être transférés dans un monomère hydrophobe pour la fabrication de LSC planaire. Dans la présence d'un catalyseur approprié et d'un

agent de réticulation (Figure R.5a), la longue chaîne carbonée OLA a été fonctionnalisée sur la surface des points-C originaux. En raison de la présence de ce groupe fonctionnel hydrophobe, les points-C modifiés par OLA avec un QY comparable (~20-30%) peuvent être dispersés uniformément dans un solvant hexane non polaire. De plus, le QY des points-C d'origine peut être amélioré à 40% par le recouvrement de surface avec des ions Na^+, ce qui est bénéfique pour la fabrication de LSCs en couches minces. Dans la Figure R.5b, les spectres d'absorption et d'émission de points-C avec différents traitements de surface sont montrés. On peut observer que l'absorption dans la gamme de longueurs d'onde plus longues de 550-700 nm est réduite après le traitement de surface, ce qui indique que les défauts de surface sont bien passivés, ce qui induise un chevauchement spectral plus faible entre les pics d'absorption et d'émission (presque pas de changements après la modification de la surface). Les dégradations de PL sur la Figure R.5c révèlent une dynamique similaire entre les points-C préparés et traités en surface, en accord avec les valeurs rapportées. Les points-C modifiés par l'OLA ont été appliqués pour préparer les LSCs planaires avec la grande surface (Figure R.7, à gauche). La lumière orange jaune concentrée est visible lorsque le LSC est partiellement éclairé sous la lumière du soleil.

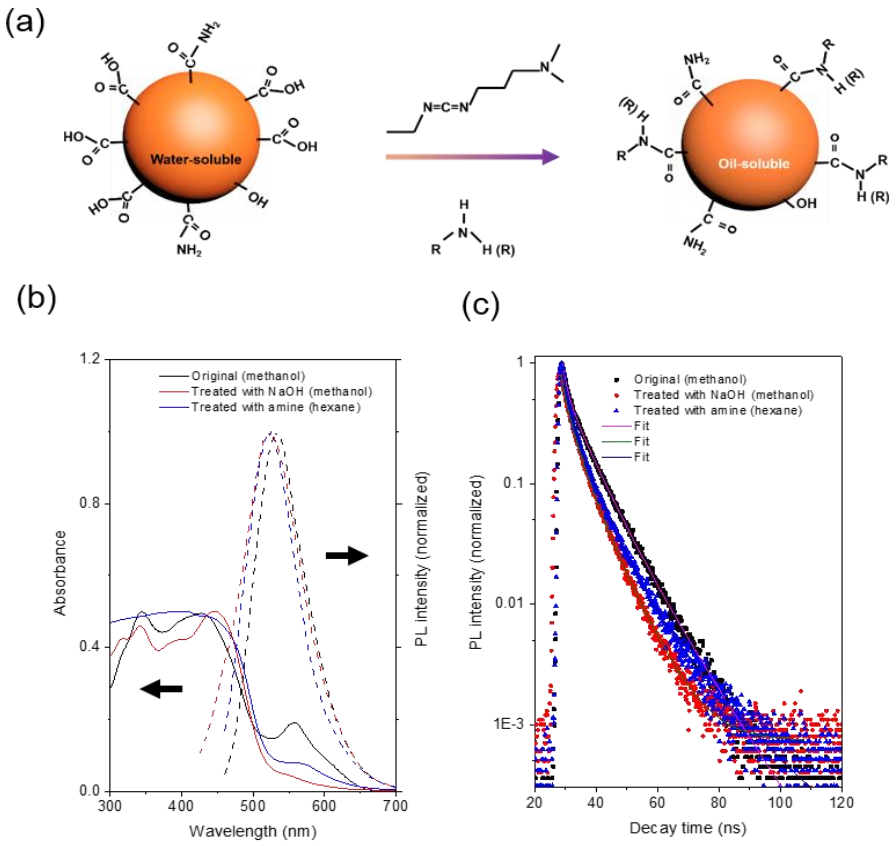

Figure R.5 (a) L'illustration schématique de la modification de surface de points-C avant et après le transfert de phase. (b, c) L'absorption, les spectres d'émission (b) et les dégradations de PL (c) des points-C par différents traitements.

Pour étudier plus profondément la faisabilité des points-C pour la fabrication de LSC, on a fabriqué des LSCs en couches minces en tandem par incorporer des points-C hydrophiles dans le PVP et les enrober-tourner sur le substrat en verre (schéma dans la Figure R.6a). Par rapport aux LSCs à base de polymère de QDs/PLMA mentionnés ci-dessus qui ont une épaisseur de 2 mm, l'épaisseur d'une couche de points-C/PVP sur un substrat en verre est seulement de 50-100 µm. Les photons émis voyagent à l'intérieur du verre, ce qui diminue la probabilité de rencontrer des points-C, ce qui conduit une perte d'énergie réduite en raison de la réabsorption. Deux types de points-C ont été utilisés pour fabriquer les LSCs. La première couche de LSCs a été fabriquée en utilisant des

points-C UV (noté comme #1)[131] (~60% de QY) sans aucun l'après-traitement de surface. Les points-C modifiés par NaOH visibles (noté comme #2) avec ~40% d'un QY et les points-C originaux sans aucun traitement de surface (~30% de QY) ont été utilisés pour fabriquer la deuxième couche de LSCs en couches minces (Figures R.6a, b). Comme le montre dans la Figure R.6b, les points-C UV présentent une très grande séparation des spectres d'absorption et d'émission et un QY élevé de 60%, ce qui réduit la perte de réabsorption. De plus, la lumière visible émise dans la première couche échappée par le guide d'ondes pourrait être absorbée par la deuxième couche de points-C traités par NaOH, en se concentrant à partir des bords du substrat de verre. En utilisant des points-C modifiés UV et NaOH visibles, nous avons fabriqué des LSCs en couches minces en tandem semi-transparents sous différentes illuminations (Figure R.7b). Les LSCs à base de points-C en couche mince présentent une très bonne transparence dans la lumière visible, ce qui est favorable à l'utilisation de fenêtres solaires.

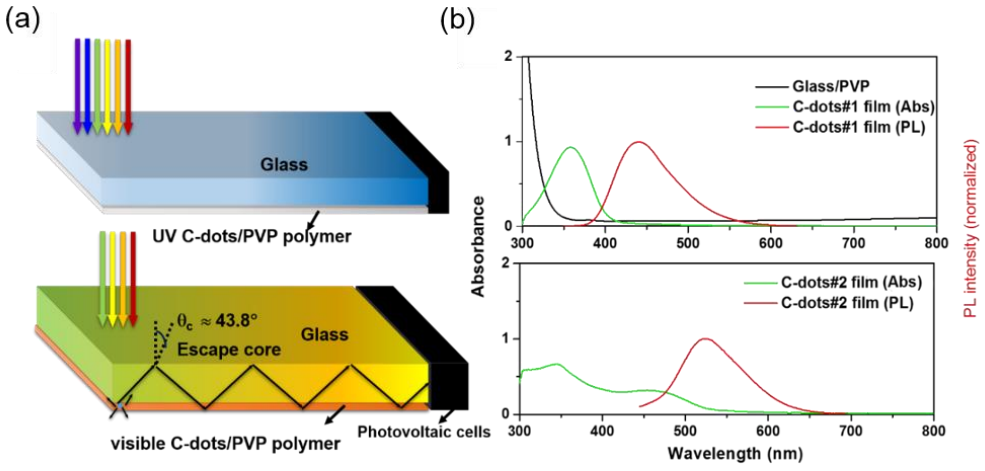

Figure R.6 (a) Schémas de LSCs en couches minces en tandem basées sur des points-C UV (en haut) et des points-C visibles (en bas). (b) Les spectres d'absorption et d'émission des points-C UV (#1, en haut) et des points-C (#2, en bas) traitées au NaOH et du spectre d'absorption de la PVP sur substrat de verre.

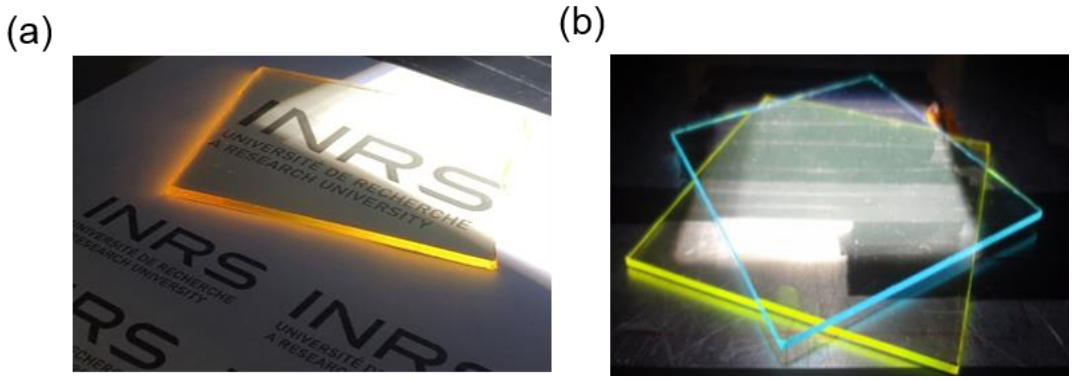

Figure R.7 Photographies de LSCs à base de points-C et polymère avec une grande surface (à gauche) et à couches minces en tandem (à droite) sous illumination d'un soleil. Deux types de points-C sont utilisés.

Les LSCs en couches mince en tandem atteignent un rendement optique externe d'environ 1,1% sous illumination d'un soleil et présentent une très bonne photostabilité par rapport aux LSCs inorganiques à base de QDs. Ce travail ouvre la voie à l'élaboration de LSCs basés sur des points-C verts, économiques, stables et efficaces. Le rendement optique externe actuellement obtenue dans les LSCs basés sur des points-C est encore plutôt faible. D'autres recherches visant à atteindre des LSCs avec un rendement élevé devraient se concentrer sur le développement de points-C avec une large gamme d'absorption, un QY élevé et un grand décalage de Stokes.

La publication liée à ce travail montre ci-dessous:

[63] Y. Zhou, D. Benetti, X. Tong, L. Jin, Z. M. Wang, D. Ma, H. Zhao, and F. Rosei. Colloidal carbon dot based highly stable luminescent solar concentrators, *Nano Energy*, 44:378-387, 2018.

Chapitre 5 La synthèse et la caractérisation de la photoanode à base de nanoparticules de $PbSe_{1-x}S_x$ pour la production d'hydrogène par l'énergie solaire

Comparant avec les QDs colloïdales, les NPLs présentent une série de propriétés optoélectroniques remarquables pour utilisations variées dans les technologies solaires, comme les cellules solaires ou la production d'hydrogène solaire, en raison de leur structure électronique appropriée pour la dissociation rapide des excitons, le transfert efficace des électrons/trous photogénérés et la stabilité photoélectrochimique (PEC) plus élevée.[152,153] Les NPLs à NIR à base de chalcogénures de plomb ou d'étain permettent d'obtenir un large spectre d'absorption accordable en épaisseur, allant d'UV à NIR, ce qui permet de faire correspondre le spectre solaire avec un chevauchement important.[133-135,150] Cependant, en raison de la plus grande taille des NPLs 2D par rapport aux QDs, et l'absence de méthodologies de synthèse fiables pour produire des NPLs de taille très petite (moins de 10 nm), les bandes interdites obtenues jusqu'à présent (< 0,9 eV) ne sont pas favorables à la génération d'H_2 PEC.

On a développé une voie d'échange de cations pour synthétiser des NPLs $PbSe_{1-x}S_x$ ternaires ultra-petites optiquement actives dans la lumière de NIR en utilisant des NPLs $CdSe_{1-x}S_x$ comme modèle (Figure R.8a). Les NPLs $CdSe_{1-x}S_x$ typiques ont de grandes dimensions latérales (60×40 nm^2) et une épaisseur de ~2 nm, correspondant à ~ 5-6 de monocouches (MCs) (Figure R.8b).[146] L'espacement *d* des NPLs $CdSe_{1-x}S_x$ basé sur l'image MET à haute résolution (HR-MET) est de 0,345 nm; il correspond aux plans {111}, indiquant la direction de croissance latérale des NPLs $CdSe_{1-x}S_x$. La composition alliée et le rapport Se/S dans les NPLs $CdSe_{1-x}S_x$ avec des rapports d'alimentation de Se/S égaux à 3:1 sont également confirmés et estimés à 2:1 à partir des données EDX dans la Figure R.8d. Les NPLs $PbSe_{1-x}S_x$ sont synthétisée par un processus d'échange de cations en utilisant différents modèles de NPLs $CdSe_{1-x}S_x$ et des précurseurs de Pb (y compris $PbCl_2$, $PbBr_2$, PbI_2 et Pb(oléate)$_2$). Ils sont uniformément dispersés et montrent des dimensions latérales (environ de 4-6 nm) beaucoup plus petites que les NPLs $CdSe_{1-x}S_x$ (Figure

R.8c). L'espacement *d* calculé est de ~0,31 nm, ce qui suggère que les NPLs $PbSe_{1-x}S_x$ se développent le long de plans d'énergie de surface faible {200}, ce qui est également observé dans les nanomatériaux de chalcogénure 2D.

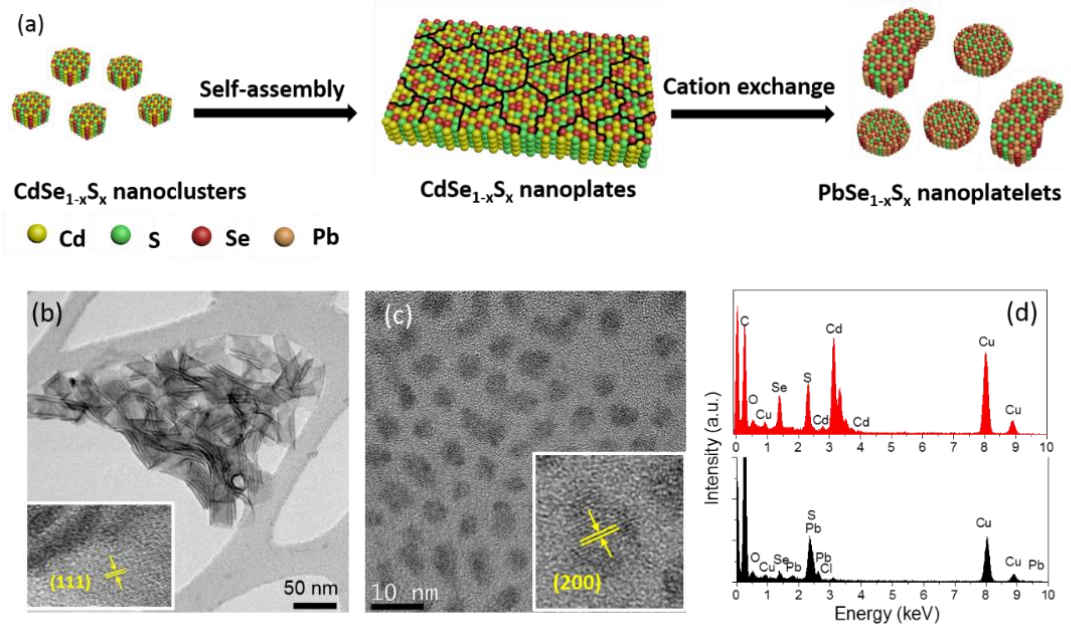

Figure R.8 (a) Schéma de la formation de NPLs à NIR par l'échange de cations en utilisant des NPLs visibles comme gabarit et transition de 1D à 3D du confinement quantique des NPLs vers des NPLs ultra-petites. (b, c) Des images MET de NPLs $CdSe_{1-x}S_x$ (b) et de NPLs $PbSe_{1-x}S_x$ (c). Les encarts sont des images HR-MET. (d) Des spectres EDS des NPLs $CdSe_{1-x}S_x$ (en haut) et des NPLs $PbSe_{1-x}S_x$ (en bas). Se/S = 3:1; précurseurs de plomb: $PbBr_2$.

Les premiers pics d'absorption et d'émission excitoniques des NPLs CdSe pures et des NPLs $CdSe_{1-x}S_x$ alliées avant l'échange cationique sont très bien définis (Figure R.9a) correspondant à 5 de MCs et à 5-6 de MCs d'épaisseur, respectivement, avec des résultats trouvés dans la littérature.[146] Le temps de réaction prolongé conduit un décalage vers le rouge des pics d'absorption et d'émission des NPLs $CdSe_{1-x}S_x$ en raison de la légère augmentation de l'épaisseur. Les pics

d'émission se font le régime de transition du vert au bleu (518-463 nm) (Figure R.9a, en haut). Après l'échange de cations, la bande d'absorption et les pics d'émission PL des NPLs $PbSe_{1-x}S_x$ passent de la région visible à NIR (Figure R.9a, en bas). Dans ces NPLs, le pic d'émission du bord de bande peut être modifié de 1182 à plus de 1382 nm en faisant varier soigneusement les conditions de réaction (les précurseurs, le temps de réaction, la température, l'épaisseur et la composition chimique des NPLs $CdSe_{1-x}S_x$ parentes). On a obtenu cette particularité dans les NPLs Pb ternaires grâce à leurs très petites dimensions latérales, qui permettent un confinement quantique fort en 3D (voir schéma dans la Figure R.8a), conduisant à une émission PL très forte et à une longueur d'onde accordable, dépassant les limites des NPLs PbS et PbS/CdS de plus grande taille (dans lequel la largeur de pic PL est généralement supérieure à 200 nm).[150] Les NPLs $PbSe_{1-x}S_x$ ultra-petites montrent des valeurs de QY records comparées à NPLs PbS de taille plus grande. L'échantillon optimisé basé sur le précurseur de $PbBr_2$, donne un QY aussi élevé que 60% pour les NPLs $PbSe_{1-x}S_x$.

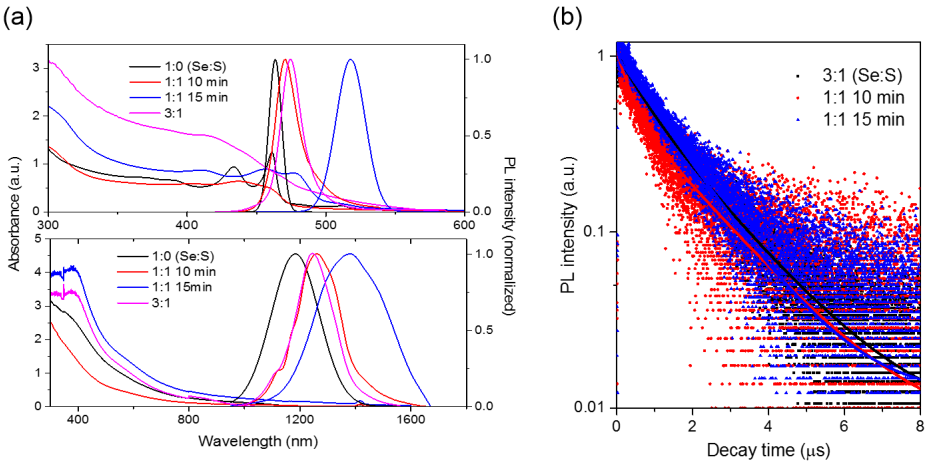

Figure R.9 (a) L'absorption et les spectres PL des NPLs $CdSe_{1-x}S_x$ parentes (en haut) et des NPLs $PbSe_{1-x}S_x$ après échange de cations (en bas). (b) Des courbes typiques de dégradation PL et les courbes d'ajustement (lignes pleines) pour les NPLs $PbSe_{1-x}S_x$ avec différentes conditions de réaction mesurées au pic d'émission dans le toluène, représenté sur une échelle semi-logarithmique. La longueur d'onde d'excitation a été fixée à 450 nm.

Sur le concept prouvé, on a utilisé des NPLs à NIR synthétisés comme photo-sensibilisateurs pour la génération d'H_2 PEC à l'énergie solaire. La performance PEC des photoélectrodes a été évaluée dans une configuration à trois électrodes, consistant en une électrode de travail à photoanode NPLs-TiO_2, une contre-électrode Pt et une électrode de référence Ag/AgCl saturée en KCl. La performance PEC des NPLs est illustrée dans la Figure R.10a. La densité de photocourant saturé est obtenue d'environ 0,8 mA/cm^2 pour les NPLs purs traités avec des cations Cd à 40 °C. En raison de l'oxydation de surface au cours de la préparation de l'anode, nous observons le pic d'oxydation apparent à -0,05 V vs RHE dans la courbe *J-V*. Cette oxydation peut être évitée en préparant l'anode dans une boîte à gants. En optimisant la photoanode à travers différentes structures d'une couche de TiO_2 et le temps de dépôt électrophorétique, la densité de photocourant saturé de la photoanode à base de NPLs-Cd dans le système PEC est augmentée à 3,8 mA/cm^2. Un autre échange de ligand avec du bromure de cétyltriméthylammonium et un traitement de l'après-hybridation à 150 °C pendant 15 min sous vide induisent une augmentation de la densité de photocourant d'environ 5,0 mA/cm^2 à 1,0 V par rapport à RHE. Cette densité de photocourant est comparable aux valeurs rapportées à partir de systèmes PEC utilisant des QDs PbS/CdS colloïdales (3-11 mA/cm^2),[154,173] hématite (3,05 mA/cm^2)[174] et des oxydes métalliques, ex. nanofils Cu_2O (10 mA/cm^2).[175]

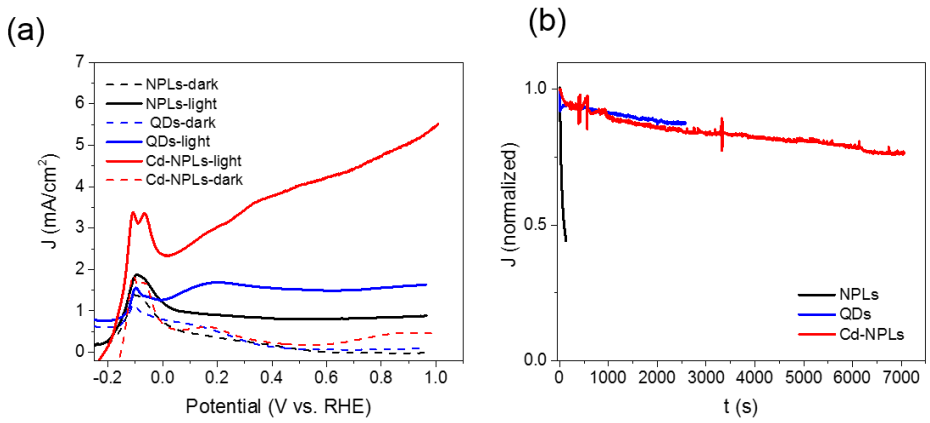

Figure R.10 (a) La dépendance densité-potentiel du courant des photoanodes sur TiO_2/NPLs/ZnS, TiO_2/PbS/CdS QDs/ZnS et TiO_2/Cd-NPL/ZnS (avec échange de ligand et traitement de l'après-recuit) dans le noir et sous illumination AM 1,5G (100 mW/cm^2). (b) La densité de courant mesurée en fonction du temps d'illumination à 0,8 V vs. RHE sous éclairage AM 1,5G (100 mW/cm^2) pour les photoanodes.

Comme le montre dans la Figure R.10b, la densité de courant dans le dispositif PEC basé sur les NPLs chute très rapidement, ~ 60% de baisse de la valeur d'origine après 140 secondes d'illumination. Dans un grand contraste, la photostabilité de la photoanode basée sur les NPLs-Cd (100 °C) est largement améliorée par rapport aux NPL sans traitement au Cd, comparable à celle de QDs basés sur PbS/CdS. La stabilité améliorée du dispositif PEC basé sur les NPLs traitées au Cd comparé aux NPL nus est due à la passivation efficace de la surface par la coquille CdS, qui peut protéger les matériaux du noyau pendant la préparation et le fonctionnement des cellules. On a également estimé le taux de la génération d'H_2 d'environ 44 mL·cm^{-2}·jour^{-1}.